SAINT PETERSBURG STATE UNIVERSITY

Krapivin Dmitry Andreevich

Electronic transitions in diatomic quasimolecules under interaction with pulses of a strong electromagnetic field

Specialization 1.3.3. Theoretical physics

Dissertation is submitted for the degree
of Candidate of Physical and Mathematical Sciences
Translation from Russian

Thesis supervisor:
Telnov Dmitry Alexandrovich
Doctor in Physical and Mathematical Sciences

Saint Petersburg
2023

Contents

Introduction

Relevance of the research topic and elaboration of the topic. The achievements of recent years in the field of laser technology have made it possible to experimentally observe atomic and molecular processes on ultrashort attosecond time scales [1, 2, 3, 4] and in the region of short wavelengths [1, 5, 6]. It is worth noting here free-electron lasers, which make it possible to obtain short-wavelength coherent radiation up to the X-ray range and to study ultrafast molecular dynamics [7]. Due to the presence of additional degrees of freedom in molecules, their response to strong radiation is much more complex than that of atoms, and the study of such processes presents a new challenge for researchers. The term "quasimolecule" in this work denotes a system of two interacting atoms or ions located at interatomic distances from each other characteristic of molecules, but not representing a stable formation. Quasimolecules can appear over a certain time interval when atoms or ions collide with each other. Even the simplest diatomic molecules in strong laser fields attract much attention from researchers, both in the theory and experiment [8]. Revolutionary changes in the experimental techniques made it possible to observe and measure various processes with diatomic molecules in laser fields, including the effects due to contributions from multiple molecular orbitals [9] and orientation of the molecular axis [10, 11], as well as electron diffraction [12, 13], molecular orbital imaging [14, 15] etc. Particularly, can be mentioned the interference phenomena in the spectra of electrons after above-threshold ionization [16, 17, 18, 19] and in the high-order harmonic generation (HHG) spectra [20, 21, 22, 23], where important information about the internal structure of molecules can be encoded. The electron holography in strong fields, which has attracted great interest in recent years [24, 25, 26, 27]. The possibility of creating quasi-stable molecular systems in which interatomic bonding forces are induced by a laser is demonstrated [28], the possibility of a qualitative change in the spectra of emitted high-energy electrons during the

collision of a Ne^{10+} ion with a He atom in a weak external field is shown [29], it was found that infrared fields of moderate intensity can significantly increase the cross-sections for dissociative recombination in the low-energy region due to the Coulomb focusing effect [30], the dynamics of the collision of two atoms in an optical microtrap has been experimentally studied [31], the charge transfer mechanism was analyzed taking into account the radial and rotational interactions in the collision of B^{2+} with Ar and Ne atoms for collision energies $E_{lab} \approx (0.02 - 1080)$ keV [32] etc.

The simplest diatomic molecule, the one-electron ion H_2^+, has been repeatedly used in theoretical studies as a prototype of a diatomic molecule in exploring the ionization and HHG processes, including the effects of molecular axis orientation and two-center interference [33, 34, 35, 36, 37, 38, 39]. A strong dependence of the ionization dynamics on the molecular axis orientation was revealed in [37]. Also, during ionization by a circularly polarized laser pulse, destructive interference manifests itself in the form of splitting of peaks in the energy spectrum of photoelectrons when emitted at a certain angle to the axis of the molecule [34]. In [35] the dependence of multiphoton ionization and high-order harmonic generation from the ground and excited electronic states of H_2^+ on the orientation of the molecular axis with respect to the polarization of laser radiation was investigated. In the works mentioned above, the time-dependent Schrödinger equation for a two-center quantum system in an external field was solved using various numerical methods: the split-operator method with a uniform radial grid in spherical coordinates [34] and the split-operator method in the energy representation combined with pseudospectral discretization in prolate spheroidal coordinates [35], using polynomial expansions in spheroidal coordinates [36], combined finite element method and representation of discrete variables [39], and also using the expansion in terms of the basis of B-splines and spherical harmonics [40]. One of the research objectives of this work is the study of H_2^+ ionization under the action of strong linearly polarized laser radiation with a wavelength in the far ultraviolet region. The dissertation demonstrates an anomalous dependence of the ionization probability on the angle between the molecular axis and the polarization vector of the external field.Usually, the effects of two-center interference are associated with the destructive nature of such interference and appear as minima in the photoionization or harmonic generation spectrum. The dissertation deals with constructive two-center interference, the maximum of

which corresponds to such a geometry, when the molecular axis is not parallel to the polarization of laser radiation, which leads to an unexpected result, when the maximum ionization probability is observed when the molecular axis is perpendicular to the orientation. In the angular distributions of photoelectrons, the effect manifests itself in the form of a local minimum in the direction of polarization of the external field for a parallel orientation of the molecular axis.

An external electromagnetic field makes it possible to control the process of electron capture during collisions. This circumstance attracted attention of researchers as early as in the 1970s [41]. A number of studies in recent years were devoted to studying the influence of the phase of the electromagnetic field on this process. This circumstance is due to the fact that laser sources with stabilized phase [42, 43] are currently available, and experimental methods for measuring the field phase [44, 45] have been described. In [46] studied a field with a wavelength of $\lambda = 780$ nm and an intensity of 3.5×10^{12} W/cm^2. It was shown that for asymmetric colliding systems, such as H–He^{2+}, a change in the phase of the electromagnetic field linearly polarized in the collision plane can significantly increase the probability of charge transfer in the collision energy range of 0.05–10 keV/u. In another work [47] it was also shown that in low-energy collisions the value of the phase of the electromagnetic field has a significant effect on the charge transfer process. In symmetric systems, on the contrary, a linearly polarized external field with a polarization vector in the collision plane has small effect on the charge transfer if the ionization is negligible, as it was reported in [48] for H–H$^+$ collision: the charge transfer probability is almost the same for different initial phases as well as in the absence of the external field. For a strong circularly polarized field (intensity 5×10^{13} W/cm^2), the results of [49] demonstrate a significant effect of the field phase on both the ionization probability and the charge transfer probability. The paper [50] shows a significant increase of the charge transfer cross-section in the H–He^{2+} collision for parallel and perpendicular laser polarization at an intensity of 3.5×10^{12} W/cm^2 and a wavelength of 800 nm. In the work [51], the possibility of optimal control of the charge transfer process by the laser field in slow collisions was studied within a one-dimensional model. One of the goals of this dissertation is to study the influence of the phase and intensity of a field linearly polarized in the collision plane on ionization and the probability of electron capture by an incident particle in a symmetric H–H$^+$ system in low-energy

collisions for various frequencies.

In addition to the phenomenon of two-center interference and the influence of the phase of the electromagnetic field on the process of electron capture, it is of great interest to study heavy one-electron ions and one-electron quasimolecules in external strong fields with very high frequencies and intensities. Theoretical treatment of such systems must be fully relativistic, since the electron moves with very high speed under the influence of both the coulomb field of a highly charged nucleus and strong external electromagnetic field. Several relativistic approaches for description of the laser–ion interaction have been suggested recently. They include numerical solution of the time-dependent Dirac equation (TDDE) in spherical coordinates with expansion of the angular part of the wave function in spherical harmonics [52, 53, 54]. Kinetically balanced B-spline basis sets in both radial and angular coordinates for the time-dependent Dirac equation with an axial symmetry were introduced in [55]. Non-Hermitian approaches have been developed, such as complex coordinate rotation[56] and complex coordinate scaling[57]. These approaches have become effective in studying multiphoton ionization processes. Other theoretical and computational approaches include the relativistic tight coupling method [58, 59], the relativistic generalization of the matrix iteration method [60] and the classical relativistic phase space averaging method [61] generalized to arbitrary central potentials for the nonstationary equation Dirac. The relativistic strong field approximation corrected for the Coulomb interaction was used to consider above-threshold ionization [62, 63].

For the external electromagnetic fields in the infrared, visible, and ultraviolet regions, where the wavelength of the radiation exceeds the atomic size to a great extent, the dipole approximation is commonly used to describe the interaction of the atom, molecule or quasimolecule with the field. In this approximation, the spatial dependence of the external field vector potential is neglected, thus the electric field of the electromagnetic wave is uniform in space, and the magnetic field vanishes.In the relativistic domain, a wide range of the laser field parameters, such as the photon energy and peak intensity, still exists where the dipole approximation is well justified. Previously, it was successfully used in the time-dependent Dirac equation to treat highly charged ions exposed to strong laser fields [52, 55, 58]. However, when the photon energy and peak intensity of the laser pulse increase, the nondipole ef-

fects become more and more important, and the dipole approximation eventually breaks down. Of course, it may happen even for nonrelativistic atomic and molecular systems described by the time-dependent Schrödinger equation [53, 64, 65, 66, 67]. As to the relativistic systems, several attempts have been made to go beyond the dipole approximation and include nondipole correction terms into the interaction with the external field in the time-dependent Dirac equation [52, 57, 54, 68]. It was shown [57] that the spatial dependence in the pulse envelope, rather than the carrier, provides a dominant correction beyond the dipole approximation. One of the goals of this dissertation is to consider the problem of relativistic ionization in a strong field for important prototypes of one-electron systems, such as homonuclear diatomic quasimolecules. Among such systems, only H_2^+ can exist as a stable molecule, quasimolecules with higher nuclear charges can temporarily form during collisions in ion beams or storage rings. Compared to atomic ions, quasimolecules have less symmetry and a large number of degrees of freedom, which greatly complicates their response to external fields. On the other hand, as the total nuclear charge approaches the critical value, highly charged quasimolecules can provide a unique opportunity for studying laser-stimulated quantum electrodynamics processes in super strong fields.

Atomic units ($\hbar = |e| = m_e{=}1$) are used throughout the paper unless specified otherwise.

Main goals of the work consist in the development and application of numerically stable algorithms for solving the Schrödinger equation and the Dirac equation to study the interaction of diatomic molecules and quasimolecules with pulses of strong coherent radiation. To do this, the following **tasks** are solved:

1. Development of an algorithm for solving the fully three-dimensional nonstationary Schrödinger equation and the nonstationary Dirac equation in an elongated spheroidal coordinate system using numerical pseudospectral methods.

2. Study of the influence of two-center interference on the process of ionization of a molecule H_2^+, prepared in the first excited electronic state $1\sigma_u$, by a linearly polarized laser pulse with a carrier wavelength in the far ultraviolet region within the framework of the non-relativistic approach (Schrödinger equation)

3. Within the framework of the relativistic approach (Dirac equation), the ener-

gies of bound states were calculated and an assessment of relativistic effects was made by scaling the system parameters with respect to the nuclear charge Z for various homonuclear quasimolecules.

4. Calculation of capture electron cross-sections in a collision of a proton with a hydrogen atom in the ground state in a field linearly polarized in the collision plane. An analysis of the influence of the frequency and phase of the electromagnetic field on the process of electron capture by an incident particle is carried out.

Scientific novelty. Within the framework of the thesis, a fully three-dimensional algorithm for solving the nonstationary Dirac equation in an external field for diatomic quasimolecules beyond the dipole approximation was developed. A similar algorithm has been developed for the Schrödinger equation. The possibility of choosing the parameters of the laser field in such a way that the maximum ionization, as well as the maximum in the angular distributions of emitted photoelectrons, is observed when the orientation of the quasimolecule axis and the laser field polarization vector is perpendicular to the orientation is demonstrated. An analysis of the influence of the phase of a linearly polarized electromagnetic field in collisions of a proton atom with a hydrogen atom in low-energy collisions for wavelengths in the infrared and far ultraviolet region is presented.

Scientific value and practical significance. The developed algorithms for describing the interaction of molecules and quasimolecules with a linearly polarized external field can find their application in the field of preparation of molecules in a certain quantum mechanical state, in the study of molecular electronic structure and electron motion for various fixed nuclear configurations. The algorithm developed for the relativistic Dirac equation makes it possible to evaluate relativistic effects in quasimolecules, and also creates the necessary theoretical basis for controlling processes the resonance process, when the carrier frequency of the laser field coincides with the difference between two levels in the quasimolecule, as a result of which ionization can be significantly strengthened. The practical application of the results obtained is directly related to the possibility of creating compact sources of intense coherent radiation and attosecond pulses. It is advisable to use the results of the dissertation in research organizations and centers involved in the interaction

of strong laser radiation with matter: Institute of General Physics of the Russian Academy of Sciences, Research Institute of Nuclear Physics of Moscow State University, Russian Research Center Kurchatov Institute, St. Petersburg State University, National Research Nuclear University "MEPhI", Moscow Institute of Physics and Technology, Institute of Applied Physics RAS, Voronezh State University, Institute of Applied Physics named after A.V. Gaponov-Grekhov RAS.

Thesis statements to be defended:

1. The probability of ionization of the H_2^+ molecule in the $1\sigma_u$ state under the influence of a linearly polarized electromagnetic field and the angular distributions of photoelectrics depend on the orientation of the molecule in an anomalous manner due to two-center interference.

2. Relativistic effects lead to an increase in the ionization potential of a quasimolecule and to a shift in the resonant frequency when interacting with an electromagnetic field. The significant inhomogeneity of the vector potential of the electromagnetic field in the region of the electron wave packet is the cause of the occurrence of non-dipole effects, expressed in increased ionization of the quasimolecule under the influence of the electromagnetic field.

3. During the collision of a proton with a hydrogen atom in an external field, the phase of the electromagnetic field, in the case of a slowly oscillating field, has a significant impact on the process of electron capture. The phase of a rapidly oscillating electromagnetic field does not have a significant effect on the dynamics of the system.

Reliability of the results obtained. All results were tested for convergence by increasing the accuracy of the calculation. The calculated values are in good agreement with the theoretical results of other authors, when it is possible to compare them. The results presented in the thesis have been published in reputable journals and discussed at several international conferences

Approbation of the research

1. International student conference "Science and progress", November 12-14, 2018, St. Petersburg, Russia.

2. All-Russian youth scientific forum “OpenSciens 2021”, November 16-18, 2021, Gatchina, Russia.

3. All-Russian Conference on Natural Sciences and Humanities with International Participation - “Science of St. Petersburg State University-2021”, December 28, 2021, online.

4. All-Russian Conference on Natural Sciences and Humanities with International Participation - “Science of St. Petersburg State University-2022”, November 21, 2022, online.

5. International Summer Conference on Theoretical Physics 2023, July 3-7, 2023, Moscow, Russia.

In addition, the results were repeatedly presented at seminars at the Department of Quantum Mechanics, Faculty of Physics, St. Petersburg State University.

Publications of the author on the topic of the dissertation. On the topic of the dissertation work, 3 articles were published in journals recommended by the Higher Attestation Commission of the Russian Federation and/or included in the RSCI, Web of Science and Scopus databases:

1. Multiphoton Ionization of One-Electron Relativistic Diatomic Quasimolecules in Strong Laser Fields / D. A. Telnov, D. A. Krapivin, J. Heslar, S.-I. Chu // The Journal of Physical Chemistry A. – 2018. — Vol. 122, no. 11. — Pp. 8026–8036. [69]

2. *Krapivin D. A., Telnov D. A.* Anomalous dependence of ionization probability and electron angular distributions on orientation of molecular axis in photoionization of H_2^+ : effect of two-center interference // Journal of Physics B: Atomic, Molecular and Optical Physics. – 2021. — Vol. 54, no. 20. — P. 205601. [70]

3. *Krapivin D. A., Telnov D. A.* Influence of the phase of the electromagnetic field on the processes of charge transfer and ionization in laser-assisted collisions of protons with hydrogen atoms // The European Physical Journal D. — 2023. — Vol. 77, no. 99. [71]

Personal contribution of the author All main results were obtained personally by the author or through joint work with other researchers.

Structure of the thesis.

The thesis contains 87 pages, 17 figures and 3 tables. The dissertation consists of an introduction, three chapters, a conclusion, and a list of references, which includes 99 titles.

- In **introduction** the relevance of the dissertation work is substantiated, the goal is formulated and the scientific novelty of the research is argued, the practical significance of the results obtained is indicated, and the scientific provisions submitted for defense are presented.

- In **the first chapter,** the theoretical approach and the numerical methods used in solving the Schrödinger equation in an external field in the velocity gauge for the two-center molecule H_2^+ are presented in detail. The wave functions of the continuous spectrum for the one-electron molecule H_2^+ are constructed. The dependence of the total probability of ionization of the system on the orientation of the molecular axis in a linearly polarized laser field from the initial state $1\sigma_u$ has been studied. Distributions of emitted photoelectrons by energy and emission angles have been constructed for wavelengths in the soft X-ray and XUV ranges in the single-photon mode.

- **The second chapter** of the dissertation is devoted to the study of relativistic effects in one-electron quasimolecules exposed to an external field and effects arising from going beyond the dipole approximation.

- **The third chapter** is devoted to the study of the influence of the phase of a linearly polarized electromagnetic field on the process of charge transfer in $H–H^+$ collisions. Collisions are considered in the low-energy regime (the velocity of the incident proton corresponds to an energy of 0.25 keV) within the framework of the dipole approximation of the electromagnetic field.

- The **conclusion** contains the main results and conclusions obtained within the framework of the dissertation work.

Anomalous dependence of ionization probability and electron angular distributions on orientation of molecular axis in photoionization of H_2^+ : effect of two-center interference

This chapter describes in detail the theoretical approach and the numerical methods used to solve the Schrödinger equation in an external field in the velocity gauge for a two-center molecule H_2^+.

The Schrödinger equation for a two-center molecular system is most conveniently solved in prolate spheroidal coordinate system. Such a system takes into account the symmetry of a two-center molecule, and the parameter of the spheroidal coordinate system makes it possible to set the internuclear distance in a simple way. Initially, the stationary Schrödinger equation is solved to obtain the energies and wave functions of the bound states. The next step describes the evolution of the initial state of the system in an external field over time. The antisymmetric wave function of the $1\sigma_u$ state was chosen as the initial state, for an internuclear distance of 2 a.u. To study the spectrum of photoelectrons, wave functions of the continuous spectrum are constructed with the correct asymptotic behavior at infinity. The calculation of the distributions of the emitted photoelectrons over the angles and energies of the emission makes it possible to analyze the dependence of the total ionization probability and photoelectron spectra on the orientation of the molecular axis. It turns out that in the wavelength range from 6 to 23 nm, an anomalous behavior of the ionization probability is detected, where it increases with an increase in the angle between the polarization vector of the external field and the axis of the molecule, reaching a maximum at a perpendicular orientation of the molecule. This anomalous behavior is explained by the two-center interference of contributions to the wave packet from regions of space near the nuclei of the molecule.

In Chapter 1, the field is assumed to be linearly polarized and is considered in the dipole approximation.

1.1 Schrödinger equation in prolate spheroidal coordinates

The time-dependent Schrödinger equation for a one-electron molecular system or quasimolecular in an external field has the form:

$$i\frac{\partial}{\partial t}\Psi(\mathbf{r},t) = [H_0 + V]\Psi(\mathbf{r},t). \tag{1.1}$$

Here H_0 is the unperturbed Hamiltonian, which includes the kinetic energy operator and the interaction potential $U(\mathbf{r})$ between the electron and the nuclei:

$$H_0 = -\frac{1}{2}\nabla^2 + U(\mathbf{r}), \tag{1.2}$$

The operator V — describes the interaction of the electron with the external electromagnetic field. When choosing the velocity gauge in the dipole approximation, this operator takes the form:

$$V = -i(\mathbf{A}\cdot\nabla) + \frac{1}{2}A^2, \tag{1.3}$$

moreover, the vector potential $\mathbf{A}$ in this case depends on time, but does not depend on spatial coordinates. The force acting on an electron from an external electric field is expressed in terms of a vector potential using the usual relationship:

$$\mathbf{F} = \frac{\partial \mathbf{A}}{\partial t}. \tag{1.4}$$

For a two-center molecular system, the natural choice of the coordinates to solve the Schrödinger equation (1.1) is prolate spheroidal coordinates ξ, η, ϕ, which are related to the Cartesian coordinates as [72]:

$$\begin{aligned} x &= a\sqrt{(\xi^2-1)(1-\eta^2)}\cos\phi, \\ y &= a\sqrt{(\xi^2-1)(1-\eta^2)}\sin\phi, \\ z &= a\xi\eta. \end{aligned} \tag{1.5}$$

The intervals of change of spheroidal coordinates are given by the following relations:

$$1 < \xi < \infty, \quad -1 < \eta < 1, \quad 0 < \phi < 2\pi. \tag{1.6}$$

In order to write the Schrödinger equation in a spheroidal coordinate system, Lame multipliers are needed:

$$H_\xi = a\sqrt{\frac{\xi^2-\eta^2}{\xi^2-1}}. \quad H_\eta = a\sqrt{\frac{\xi^2-\eta^2}{1-\eta^2}}, \quad H_\phi = a\sqrt{(\xi^2-1)(1-\eta^2)}. \tag{1.7}$$

The connection of the orts of the Cartesian coordinate system with the orts of the spheroidal coordinate system is given by the following relations:

$$\vec{e}_z = \frac{f\eta}{H_\xi}\vec{e}_\xi + \vec{e}_\eta\frac{f\xi}{H_\eta}, \tag{1.8}$$

$$\vec{e}_x = \vec{e}_\xi\cos\phi\frac{f\xi}{H_\eta} - \vec{e}_\eta\cos\phi\frac{f\eta}{H_\xi} - \sin\phi\vec{e}_\phi, \tag{1.9}$$

$$\vec{e}_y = \vec{e}_\xi\sin\phi\frac{f\xi}{H_\eta} - \vec{e}_\eta\sin\phi\frac{f\eta}{H_\xi} + \cos\phi\vec{e}_\phi. \tag{1.10}$$

The nabla differential operator has the following expression:

$$\vec{\nabla} = \frac{1}{H_\xi}\frac{\partial}{\partial\xi}\vec{e}_\xi + \frac{1}{H_\eta}\frac{\partial}{\partial\eta}\vec{e}_\eta + \frac{1}{H_\phi}\frac{\partial}{\partial\phi}\vec{e}_\phi \tag{1.11}$$

Written using spheroidal coordinates, the kinetic energy operator and the interaction potential with nuclei have the form:

$$\begin{gathered}-\frac{1}{2}\nabla^2 = -\frac{1}{2a^2}\frac{1}{\xi^2-\eta^2}\left[\frac{\partial}{\partial\xi}(\xi^2-1)\frac{\partial}{\partial\xi}+\right.\\ \left.+\frac{\partial}{\partial\eta}(1-\eta^2)\frac{\partial}{\partial\eta} + \frac{\xi^2-\eta^2}{(\xi^2-1)(1-\eta^2)}\frac{\partial^2}{\partial\phi^2}\right],\end{gathered} \tag{1.12}$$

$$U(\xi,\eta) = -\frac{(Z_1+Z_2)\xi + (Z_2-Z_1)\eta}{a(\xi^2-\eta^2)}, \tag{1.13}$$

Z_1 and Z_2 are nuclear charges, $Z_1 = Z_2 = 1$ for the molecular ion H_2^+. The z axis of the Cartesian coordinate system, in this chapter of the dissertation, is directed along the axis of the molecule. The nuclei of the molecule are placed at the centers of the spheroidal coordinate system, and the distance between them R is given by the parameter a: $R = 2a$. The calculations assume $a = 1$ a.u., which corresponds to the equilibrium internuclear distance $R_e = 2$ a.u. ion H_2^+ in the ground electronic state. Before solving the nonstationary equation (1.1), it is necessary to solve the eigenvalue problem for unperturbed Hamiltonian H_0:

$$[H_0 + U]\Psi_i(\mathbf{r}) = E_i\Psi_i(\mathbf{r}), \tag{1.14}$$

to obtain the wave function of the initial state as an eigenfunction of the first excited electronic state of the molecule ($1\sigma_u$). Since the H_2^+ molecule is unstable and dissociates in this electronic state, its preparation may be the result of resonant excitation from the stable ground state ($1\sigma_g$). The practical feasibility of such a process has been experimentally confirmed [73]. When solving the problem numerically, the size of the spatial region is determined by the parameter R_b. For $a\xi = R_b$, the zero boundary condition is imposed on the wave function. In the calculations of this chapter, $R_b = 80$ a.u, which for the parameters of the external field used (see below) makes it possible to correctly describe all processes that are physically significant for this problem. To numerically solve the eigenvalue problem (1.14), the coordinates ξ and η are discretized using the generalized pseudospectral method. The idea of using such methods is to discretize functions over points, called collocation points. Define mapping $x \to \xi : x \in (-1; 1)$:

$$a\xi_i = a + R_l \frac{(1 + x_i)^2}{1 - x_i + 4\frac{R_l}{R_b}}, \tag{1.15}$$

where R_l is a parameter, by adjusting which one can change the distribution of collocation points, as well as improve the accuracy of calculations. R_b is a boundary parameter, it must be chosen large enough to correctly describe the dynamics of the system in the laser field. The size of the spatial domain, beyond which the wave function is assumed to be equal to 0, for the grid $a\xi$ (pseudo-radial) is equal to $R_b + a$. The map (1.15) is quadratic in the neighborhood of $\xi = 1$, so the density of collocation points near the centers of the prolate spheroidal coordinate system is high. This is important for accurate calculations with the model of a non-point nucleus, since the size of the nucleus is several orders of magnitude smaller than the size of the molecular system. To discretize ξ and functions depending on ξ, the Gauss-Legendre-Radau scheme is used. The collocation points for this scheme look like [74, 75]:

$$x_i : P_{N_x}(x_i) - P_{N_x+1}(x_i) = 0, \tag{1.16}$$

where $P_{N_x+1}(x_i), P_{N_x}(x_i)$ are the Legendre polynomials calculated at the collocation points (N_x is the number of collocation points for the coordinate ξ). Weights for discretization at collocation points have the form:

$$w_i^x = \frac{1}{(N_x + 1)^2} \frac{1 + x_i}{(P_{N_x}(x_i))^2}. \tag{1.17}$$

Formulas for integrating and differentiating an arbitrary function:

$$\int_{-1}^{1} f(x)dx = \sum_{i=1}^{N_x+1} f(x_i)w_i^x, \tag{1.18}$$

$$\frac{df}{dx}(\xi(x_i)) = \frac{1}{\xi_i'}\sum_{i'=1}^{N_x+1} D_{ii'}^x f(x_{i'}), \tag{1.19}$$

where:

$$D_{ii'}^x = \frac{(1+x_{i'})P_{N_x}(x_i)}{(x_i - x_{i'})(1+x_i)P_{N_x}(x_{i'})} \quad (i \neq i'), \tag{1.20}$$

$$D_{ii}^x = -\frac{(1+x_i)P_{N_x}(x_i)}{2(1+x_i)(1+x_i)P_{N_x}(x_i)} \quad (i = i'). \tag{1.21}$$

For the η coordinate, the mapping $\eta \to y : y \in (-1; 1)$

$$\eta_j = \sin\Big(\frac{\pi}{2}y_j\Big). \tag{1.22}$$

For this coordinate, the Gauss-Legendre scheme is applied (N_y is the number of collocation points for the coordinate η):

$$y_j : P_{N_y}(y_j) = 0, \qquad \int_{-1}^{1} g(y)\,dy = \sum_{j=1}^{N_y} g(y_j)w_j^y, \tag{1.23}$$

$$w_j^y = \frac{1}{(1-y_j^2)[P'_{N_y}(y_j)]^2}, \tag{1.24}$$

$$\frac{dg}{dy}(\eta(y_j)) = \frac{1}{\eta_j'}\sum_{j'=1}^{N_y} D_{jj'}^y g(y_{j'}), \tag{1.25}$$

where:

$$D_{jj'}^y = \frac{P'_{N_y}(y_j)}{(y_j - y_{j'})P'_{N_y}(y_{j'})}, \quad (j \neq j'), \tag{1.26}$$

$$D_{jj'}^y = \frac{y_j P'_{N_y}(y_j)}{(1-y_j^2)P'_{N_y}(y_j)}, \quad (j = j'). \tag{1.27}$$

The ϕ coordinate is discretized using the Fourier grid method [76]. This method builds a grid with a uniform step:

$$\phi = s\Delta\phi, \tag{1.28}$$

the unperturbed Hamiltonian (1.2), in spheroidal coordinates, can be written as:

$$H_0 = T(\xi, \eta, \phi) + U(\xi, \eta).$$

Next, the integer n is determined by the following relation:

$$2n = (N_\phi - 1),$$

where N_ϕ is the number of grid points, which is necessarily odd. Then, the discretized (by the angle ϕ) Hamiltonian will be written in the form:

$$H_{ss'} =< \psi_s|H|\psi_{s'} >= \frac{1}{\Delta\phi} \left(\sum_{l=-n}^{n} \frac{e^{il2\pi(s-s')/N_\phi}}{N_\phi} T_l + U(\phi_s)\delta_{ss'}, \right) \tag{1.29}$$

where

$$T_l = l\Delta k, \quad \Delta k = \frac{2\pi}{N_\phi \Delta\phi} = 1. \tag{1.30}$$

Combining negative and positive values of l in a formula (1.29):

$$H_{ss'} = \frac{1}{\Delta\phi} \left(\sum_{l=1}^{n} \frac{2cos(l2\pi(s-s')/N_\phi)}{N_\phi} T_l + U(\phi_s)\delta_{ss'} \right). \tag{1.31}$$

After discretization, the equation (1.1) is a system of linear equations from which, by diagonalization, the energy values and wave functions of the bound states are found.

1.2 Solution of the non-stationary Schrödinger equation in an external field

The external field is assumed to be linearly polarized and directed at the angle β to the z axis, that is, to the internuclear axis of the molecule. For a homonuclear molecule, the range of variation of the angle β from 0° to 90°. Let's fix the x and y axes of the Cartesian coordinate system so that the vector $\mathbf{F}$ always lies in the $x-z$ plane. Then the vector $\mathbf{F}$ is decomposed into components along the x and z axes:

$$\mathbf{F}(t) = F(t)[\sin\beta\, \mathbf{e}_x + \cos\beta\, \mathbf{e}_z], \tag{1.32}$$

and the time dependence $F(t)$ has the following form:

$$F(t) = F_0 \sin^2\left(\frac{\omega t}{2N}\right) \sin\omega t \quad (0 \le \omega t \le 2\pi N), \tag{1.33}$$

where N — is the number of optical cycles in the pulse and ω is the carrier frequency of the electromagnetic wave. In this chapter of the dissertation, the calculations were made for the values $\omega = 3.645$ a.u. (wavelength 12.5 nm) and $N = 8$. To describe the time evolution of the wave function of the equation (1.1), two different methods are used, applicable to both the Schrödinger equation and the Dirac equation. The first is the split-operator method in energy representation [77]. The following scheme is used to describe the evolution of the wave function:

$$\begin{gathered}\Psi(t+\Delta t) = exp(-i\frac{1}{2}\Delta t H_0)\times \\ exp(-i\Delta t V(t+\frac{1}{2}\Delta t)) \times exp(-i\frac{1}{2}\Delta t H_0)\Psi(t)\end{gathered} \tag{1.34}$$

The expression $exp(-i\frac{1}{2}\Delta t H_0)$ is a free propagator. The field propagator is time-dependent and must be calculated at each time step. However, this operation does not take much time. Another method is based on the application of the Crank-Nicolson algorithm [78]

$$\begin{gathered}\left[1 + \frac{i}{2}\Delta t H\left(t+\frac{1}{2}\Delta t\right)\right]\Psi(t+\Delta t) \\ = \left[1 - \frac{i}{2}\Delta t H\left(t+\frac{1}{2}\Delta t\right)\right]\Psi(t)\end{gathered} \tag{1.35}$$

where Δt is the time step. To find the wave function at time $t + \Delta t$, a system of linear equations (1.35) is solved at each step. The smaller the Δt value, the more accurate the approximation (1.35) for calculating the wave function, but the larger the number of steps and the calculation time. Calculating the wave function at each time step in this method involves not only matrix-vector multiplication, but also solving a system of linear equations. As has been verified numerically, the time step can be set to approximately 100 times larger than the split operator method to achieve the same level of accuracy, significantly reducing the overall number of time steps. Numerical tests for the electromagnetic field in the dipole approximation demonstrate that with an increase in the number of collocation points (increasing the value of the expression $N_x \cdot N_y \cdot N_\phi$), the time required to execute the Crank-Nicholson algorithm increases significantly faster than the program execution time based on the use of the split operator method. For the selected number of collocation points (see below), the Crank-Nicholson method turns out to be faster than the split operator method. All calculations presented in this chapter were performed

using the Crank-Nicholson method. The number of steps is set to $N_s = 512$ for each optical cycle, which provides a reasonable compromise between accuracy and computational speed. As a result of the influence of an external field, the wave function propagates to the boundaries of the region within which sampling is carried out. To prevent nonphysical reflection of the wave function from the boundaries of this region, the wave function at each step is multiplied by a mask function, which smoothly decreases to zero towards the boundary of the region:

$$\begin{aligned} f(\xi) &= \cos\left(\pi \frac{a\xi - R_a}{2(R_b - R_a)}\right)^{1/4} \quad (R_a \le a\xi \le R_b), \\ f(\xi) &= 1 \quad (a \le a\xi \le R_a), \end{aligned} \tag{1.36}$$

where R_a is a parameter that determines the value of ξ at which the mask function begins to decrease. The peak field strength was $F_0 = 1.194$ a.u, which corresponds to the field intensity $I_0 = 5 \times 10^{16}$ W/cm^2. In calculations, the near-boundary layer was set by the value $R_a = 65$ a.u. Note that for an arbitrary orientation of the molecular axis relative to the polarization vector of the external field, the projection of the angular momentum on the molecular axis is not preserved, and the problem (1.35) is essentially three-dimensional. In this chapter, the following numerical parameters were used calculations: 180 collocation points for the ξ coordinate, 16 collocation points for the η coordinate and 5 for the ϕ coordinate. The total linear size of the equation system matrix (1.35) is equal to 14400.

The duration of the laser pulse, taking into account the above parameters, is 334 as, which is significantly less than the characteristic time of motion of the nuclei. This justifies the used approximation of stationary nuclei, in which only the dynamics of electron motion is considered, and the nuclei create a static electric field.

1.3 Calculation of distributions

For the selected parameters of the laser pulse, ionization occurs mainly in the single-photon regime. The probability of finding the electron after absorption of a single photon is much greater than the probability of finding the electron after absorption of two or more photons. In this case, the electron energy after single-photon ionization ($E = \omega + E_i$, E_i is the energy of the initial state) is such that

it does not have time to reach the boundaries of the region with radius R_b for the duration of the laser pulse. Then the energy and angular distributions of such photoelectrons can be obtained by projecting the electron wave function at the end of the pulse onto the continuum eigenfunctions of the unperturbed Hamiltonian with the correct behavior at large distances (linear combination of a plane wave and incoming spherical wave).

Since the time-independent Schrödinger equation for a two-center Coulomb system allows separation of variables in prolate spheroidal coordinates, the continuum wave function (with the energy $E > 0$) can be represented using the following expansion:

$$\Psi_f(\mathbf{k},\mathbf{r}) = \sum_{l=0}^{\infty}\sum_{m=-\infty}^{\infty} C_{lm}(\mathbf{k}) R_{lm}(\xi) S_{lm}(\eta)\exp(im\phi), \tag{1.37}$$

where $C_{lm}(\mathbf{k})$ are the expansion coefficients ($\mathbf{k}$ is the momentum of an electron at an infinite distance, $k = \sqrt{2E}$). In the expression (1.37), the summation index m has the meaning of the projection of the electronic angular momentum onto the molecular axis (z axis) while the l index enumerates the Coulomb spheroidal functions [$S_{lm}(\eta)$ и $R_{lm}(\xi)$ — pseudoangular functions and pseudoradial functions], but is not equal to the absolute value of the angular momentum (the latter is not a good quantum number in the absence of spherical symmetry). The Coulomb spheroidal functions themselves satisfy the second-order ordinary differential equations:

$$\begin{aligned}\Big[\frac{\partial}{\partial\eta}(1-\eta^2)\frac{\partial}{\partial\eta} - \frac{m^2}{1-\eta^2} + 2Ea^2(1-\eta^2) \\ + 2a(Z_2 - Z_1)\eta\Big] S_{lm}(\eta) = \lambda_{lm} S_{lm}(\eta),\end{aligned} \tag{1.38}$$

$$\begin{aligned}\Big[\frac{\partial}{\partial\xi}(\xi^2-1)\frac{\partial}{\partial\xi} - \frac{m^2}{\xi^2-1} + 2Ea^2(\xi^2-1) \\ + 2a(Z_2 + Z_1)\xi\Big] R_{lm}(\xi) = -\lambda_{lm} R_{lm}(\xi).\end{aligned} \tag{1.39}$$

Equations (1.38) and (1.39) are coupled by the separation constant λ_{lm}. The equation (1.38) for the pseudoangular function is an eigenvalue problem (taking into account the requirement that the function $S_{lm}(\eta)$ must be finite at the singular points $\eta = \pm 1$ at the ends of the interval of variation of the coordinate η), and λ_{lm} plays the role of an eigenvalue. This problem is solved using the generalized

pseudospectral method, similar to the diagonalization of the unperturbed Hamiltonian H_0. For the given energy E and projection of the angular momentum m, the eigenvalues λ_{lm} are enumerated by the index l ($l = 0.1, 2\dots$).

The pseudoradial Coulomb spheroidal function $R_{lm}(\xi)$ is constructed as a solution of the Cauchy problem for the equation (1.39) with the given parameters m, E and λ_{lm} [79]. In the vicinity of the point $\xi = 1$, the function is represented by its Taylor series. The coefficients of the Taylor series can be found using simple recurrence relations. After that, the finite-difference Numerov method is applied to construct the function on the remaining range of the coordinate ξ. From the asymptotic form $\xi \to \infty$ of the pseudoradial functions δ_{lm}, one can extract the spheroidal scattering phases δ_{lm}:

$$R_{lm}(\xi) \underset{\xi\to\infty}{\approx} \frac{1}{ka\xi} \sin\left[ka\xi + \frac{Z_1 + Z_2}{k}\ln(2ka\xi) - \frac{l\pi}{2} + \delta_{lm}\right]. \tag{1.40}$$

Then the correct asymptotics of the wave functions of the continuous spectrum (1.37) and their normalization to the delta function in the momentum space,

$$\langle \Psi_f(textbf k', \mathbf{r}) | \Psi_f(\mathbf{k}, \mathbf{r})\rangle = \delta^{(3)}(\mathbf{k} - \mathbf{k}'), \tag{1.41}$$

will be ensured if the expansion coefficients of $C_{lm}(\mathbf{k})$ in the formula (1.37) have the following form:

$$C_{lm}(\mathbf{k}) = \frac{2i^l}{(2\pi)^{3/2}} \exp[-i(\delta_{lm} + m\phi_k)] S_{lm}(\cos\theta_k), \tag{1.42}$$

where θ_k and ϕ_k are the angles of the photoelectron momentum vector $\mathbf{k}$ in the spherical coordinate system.

The differential ionization probability, which describes the distribution of photoelectrons over energies and emission angles, is calculated using the following equation:

$$\frac{\partial^2 P}{\partial\Omega\partial E} = k|T_{fi}|^2, \tag{1.43}$$

$$T_{fi} = \langle \Psi_f(\mathbf{k}, \mathbf{r}) | \Psi(\mathbf{r}, \tau)\rangle, \tag{1.44}$$

where the time τ corresponds to the end of the laser pulse: $\tau = 2\pi N/\omega$.

1.4 Main results of the first chapter

The initial state of the molecular ion H_2^+ is the first excited electronic state, $1\sigma_u$. In most of our calculations, the internuclear separation is equal to $R = 2$ a.u., the equilibrium internuclear distance in the ground $1\sigma_g$ state. In the $1\sigma_u$ state, the wave function is antisymmetric under reflection of the coordinates, and there is a nodal plane located in the center of the molecule perpendicular to the molecular axis. With such a geometry of the initial state, it is natural to expect the lowest ionization probability if the molecular axis is oriented perpendicular to the polarization vector of the external field: when the electron is ejected perpendicular to the molecular axis, the contributions to the ionization amplitude from the vicinities of the two nuclei, where the electron density is concentrated, always interfere destructively. Since the electrons are driven by the linearly polarized laser field, they have higher probability to escape along the direction of the external field. If this direction is perpendicular to the molecular axis, then ionization is suppressed because of destructive two-center interference. These simple qualitative considerations are confirmed by the calculations of multiphoton ionization of H_2^+ in the laser field with the wavelength in the near infrared region [35]: the maximum and minimum of the ionization probability correspond to the parallel and perpendicular orientation of the molecular axis, respectively. For the wavelengths 6 to 23 nm in the soft X-ray and XUV regions, however, the calculated ionization probability exhibits an anomalous orientation dependence with the maximum at the perpendicular orientation.

Figure 1.1 displays the dependence of the total ionization probability of H_2^+ on the angle between the direction of the laser electric field and the molecular axis for several carrier wavelengths. Before the external field is switched on, the electron is in the first excited state $1\sigma_u$, and the internuclear distance R is fixed at 2 a.u. Shown are representative examples of the carrier wavelengths, both inside and outside the interval 6 to 23 nm. The peak intensities range from 5×10^{15} W/cm^2 at $\lambda = 34$ nm to 5×10^{18} W/cm^2 at $\lambda = 4$ nm. The intensities are high enough to produce appreciable ionization probabilities, so the data obtained by solving the time-dependent Schrödinger equation are accurate and reliable (very small ionization probabilities cannot be extracted accurately from the numerical solution of time-dependent Schrödinger equation). Based on our convergence tests, the relative

error of the calculated ionization probabilities can be estimated to be below 1% at figure 1.1. As one can see, at $\lambda = 10$ nm and $\lambda = 20$ nm the behavior of the ionization probability as a function of the orientation angle β is directly opposite to what one would expect from the simple, intuitive considerations outlined above: the ionization probability increases with an increase of the angle β and reaches a maximum at $\beta = 90°$, that is when the molecular axis is perpendicular to the polarization vector of the external field. As revealed by the calculations, such an anomalous orientation dependence of the ionization probability is observed for the wavelengths within the range 6 to 23 nm. For the wavelengths $\lambda = 4$ nm and $\lambda = 34$ nm outside this interval, an expected pattern with the minimum at $\beta = 90°$ is restored.

The wavelength range where the anomalous orientation dependence of the ionization probability is observed can be estimated with the help of the time dependent perturbation theory (TDPT). Generally, TDPT can be applied if the external field is relatively weak. The first-order TDPT can be used to calculate the one-photon ionization probability and returns the following semianalytical expression for the dependence on the orientation angle β:

$$P = P_{\parallel} \cos^2 \beta + P_{\perp} \sin^2 \beta, \tag{1.45}$$

$P_{\parallel}$ — probability of electron emission along the molecular axis, $P_{\perp}$ —perpendicular to it. These probabilities are expressed through the bound-free dipole matrix elements:

$$P_{\parallel} = \sum_{l=0}^{\infty} \int_0^{\infty} dE \; G(E) \, |\langle \Psi_{El0} | z | \Psi_i \rangle|^2, \tag{1.46}$$

$$P_{\perp} = \sum_{l=1}^{\infty} \sum_{m=\pm 1} \int_0^{\infty} dE \; G(E) \, |\langle \Psi_{Elm} | x | \Psi_i \rangle|^2. \tag{1.47}$$

The continuum wave functions Ψ_{Elm} here are described by the energy E, quantum number l, and angular momentum projection m onto the molecular axis (see (1.38) and (1.39)). The orthogonality and normalization relation:

$$\langle \Psi_{E'l'm'} | \Psi_{Elm} \rangle = \delta_{ll'} \delta_{mm'} \delta(E - E'). \tag{1.48}$$

The function $G(E)$ is determined by the time dependence of the laser field. For the

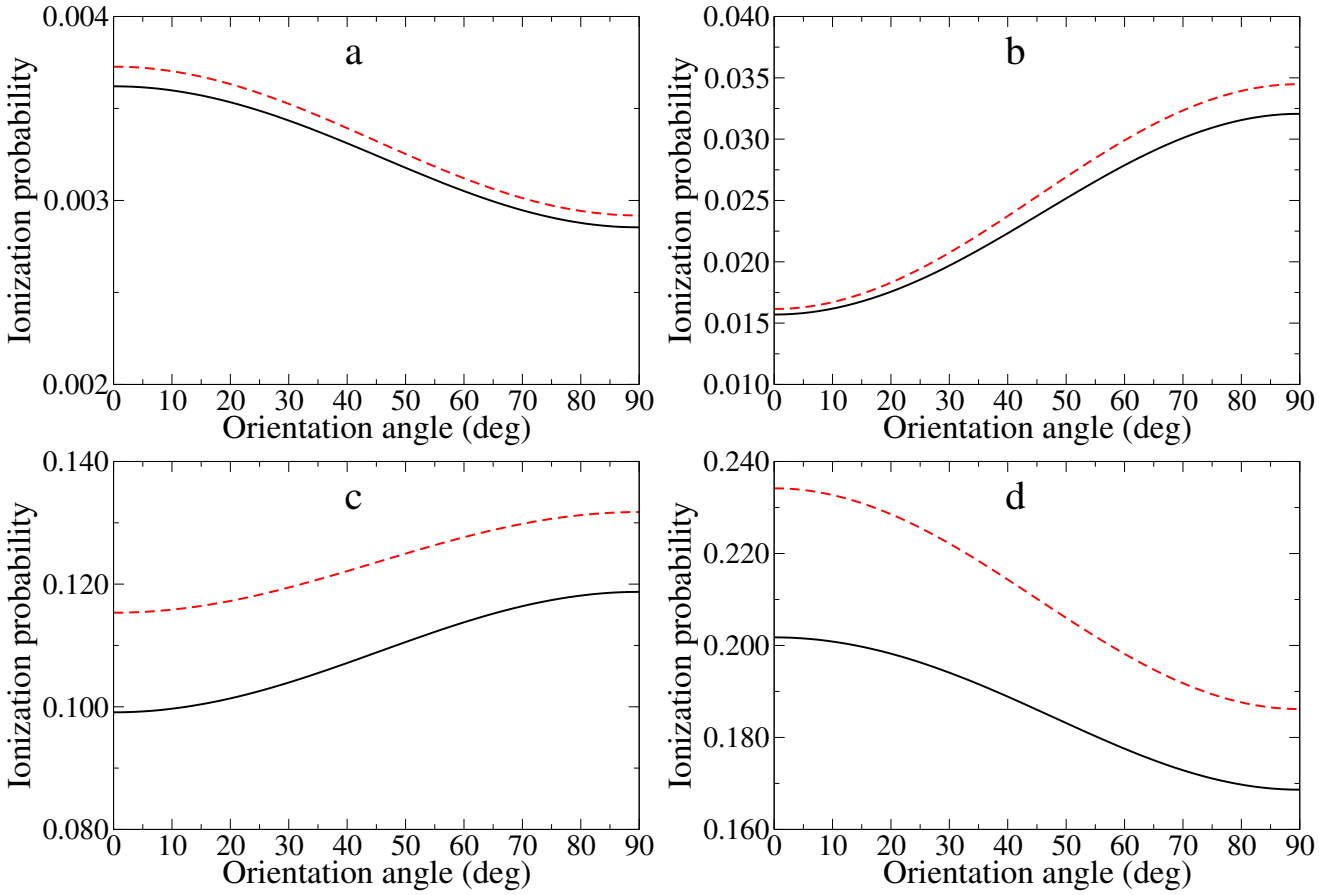

Figure 1.1: The total probability of ionization H_2^+ from the $1\sigma_u$ state depending on the angle β between the field polarization vector and the molecular axis: (a), $\lambda = 4$ nm, $I_0 = 5 \times 10^{18}$ W/cm^2; (b), $\lambda = 10$ nm, $I_0 = 5 \times 10^{17}$ W/cm^2; (c), $\lambda = 20$ nm, $I_0 = 5 \times 10^{16}$ W/cm^2; (d), $\lambda = 34$ nm, $I_0 = 5 \times 10^{15}$ W/cm^2. Internuclear distance $R = 2$ a.u., pulse duration 8 optical cycles. Solid black line: numerical data obtained from the Schrödinger equation, dotted red line: data obtained from first order perturbation theory.

pulse shape (1.33), it is defined as follows:

$$G(E) = \frac{F_0^2}{4}\left[\frac{2\omega}{\omega^2-(E-E_i)^2} - \frac{\omega_-}{\omega_-^2-(E-E_i)^2} - \frac{\omega_+}{\omega_+^2-(E-E_i)^2}\right]^2 \sin^2\left[\frac{\pi N(E-E_i)}{\omega}\right]. \quad (1.49)$$

The following notation is used here:

$$\omega_- = \omega\left(1-\frac{1}{N}\right), \quad \omega_+ = \omega\left(1+\frac{1}{N}\right). \quad (1.50)$$

As seen in figure 1.1, the TDPT ionization probabilities reproduce the correct dependence on the orientation angle β at least qualitatively.

According to (1.45), the ionization probability has a maximum at $\beta = 90^\circ$ if $P_\perp > P_\parallel$. Figure 1.2 (left graph) shows the dependence of the ratio $P_\perp/P_\parallel$ on the wavelength of the laser field. For the $1\sigma_u$ initial state, this ratio is less than unity for the wavelengths between the one-photon ionization threshold at $\lambda = 23$ nm and $\lambda = 68$ nm. In this wavelength interval, the pattern in the orientation dependence of the ionization probability corresponds to the intuitive picture outlined above, with the maximum at $\beta = 0^\circ$ and minimum at $\beta = 90^\circ$. Then between $\lambda = 23$ nm and $\lambda = 6$ nm the ionization probability exhibits an anomalous orientation dependence, with the maximum at $\beta = 90^\circ$ and minimum at $\beta = 0^\circ$. For even shorter wavelengths, one can see alternating intervals $P_\perp < P_\parallel$ and $P_\perp > P_\parallel$ with the ratio $P_\perp/P_|$ gradually approaching unity. On the same left panel of figure 1.2, the data for the initial $1\sigma_g$ state are also shown. One can see that in the latter case the ratio $P_\perp/P_\parallel$ oscillates almost with the opposite phase compared to the case of the $1\sigma_u$ initial state. Considering an effect of two-center interference on ionization, with the contributions to the ionization amplitude coming from the regions of localization of the electron density in the vicinities of the nuclei, the difference between the $1\sigma_g$ and $1\sigma_u$ states is related to the phase difference of the wave function on the nucleus 1 and nucleus 2. While this difference is zero for the $1\sigma_g$ state, it is equal to π for the $1\sigma_u$ state, thus changing the interference pattern.

Besides the phase difference of the initial wave function on the nucleus 1 and nucleus 2, the outcome of the two-center interference essentially depends on the kinetic energy of the emitted electron (which, in turn, is determined by the photon

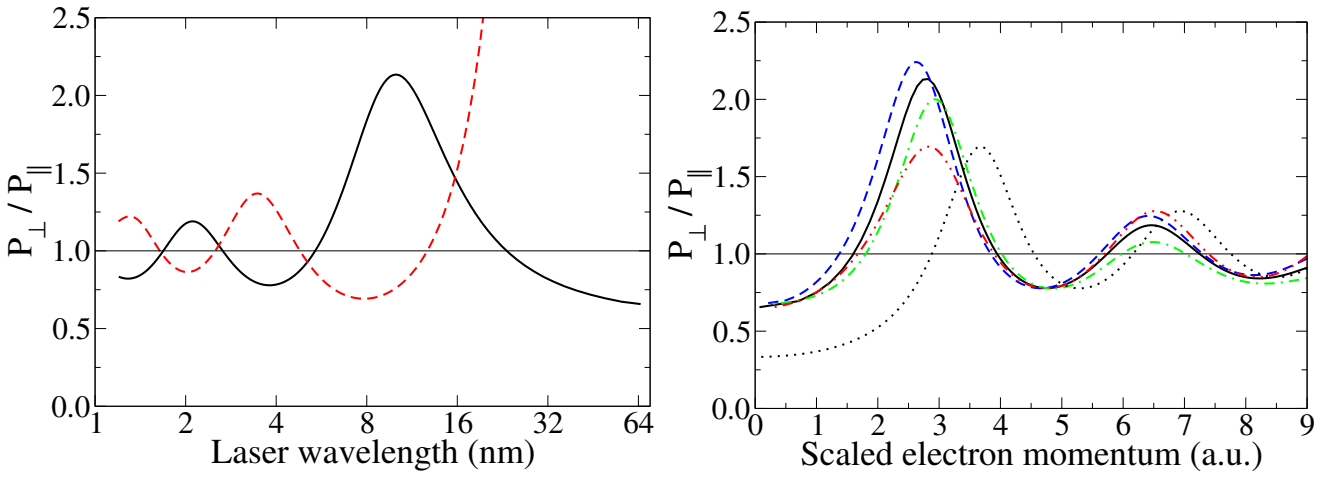

Figure 1.2: Ratio $P_\perp/P_\parallel$ from the first-order perturbation theory versus the carrier wavelength (left panel, note the logarithmic wavelength scale) and scaled photoelectron momentum ka (right panel). The solid black line in both panels corresponds to initial $1\sigma_u$ state with internuclear separation $R = 2$ a.u. Left panel: dashed red line, initial $1\sigma_g$ state with internuclear separation $R = 2$ a.u. Right panel: dashed blue line, initial $1\sigma_u$ state with internuclear separation $R = 2.4$ a.u.; dot-dash green line, initial $1\sigma_u$ state with internuclear separation $R = 1.6$ a.u.; dotted black line, analytical approximation (1.54) for initial $1\sigma_u$ state; dash double dot red line, corrected analytical approximation (1.54), (1.55) for $\varkappa_0^2 = 5.5$.

energy and ionization potential) and the internuclear distance. When these parameters change, the characteristics of the dependence of the ionization probability on the orientation of the molecular axis can change qualitatively. In figure 1.1, the data are presented for the same $1\sigma_u$ initial state and internuclear distance $R = 2$ a.u. but for various photon energies which determine the photoelectron momentum k according to the energy conservation relation (apart from the broadening of the energy distribution due to finite duration of the laser pulse):

$$k = \sqrt{2(E_i + \omega)}. \tag{1.51}$$

For comparison, figure 1.3 shows the ionization probability as a function of the angle β for the fixed electron momentum k. Besides the results for the $1\sigma_u$ state at $R = 2$ a.u. and $R = 1.6$ a.u., data are given for the state $1\sigma_g$ at $R = 2$ a.u. and for a model atomic ion initially in the $2p_0$ state (with the zero projection of the angular momentum onto the z axis). The latter case corresponds to the limit $R \to 0$ of the $1\sigma_u$ state in H_2^+. Assuming that the charge of the nucleus of an atomic ion is $Z = 2.31$ a.u., then the energy of the $2p_0$ state is equal to the energy of the $1\sigma_u$ state in the H_2^+ molecule at $R = 2$ a.u. As one can see in figure 1.3, the orientation

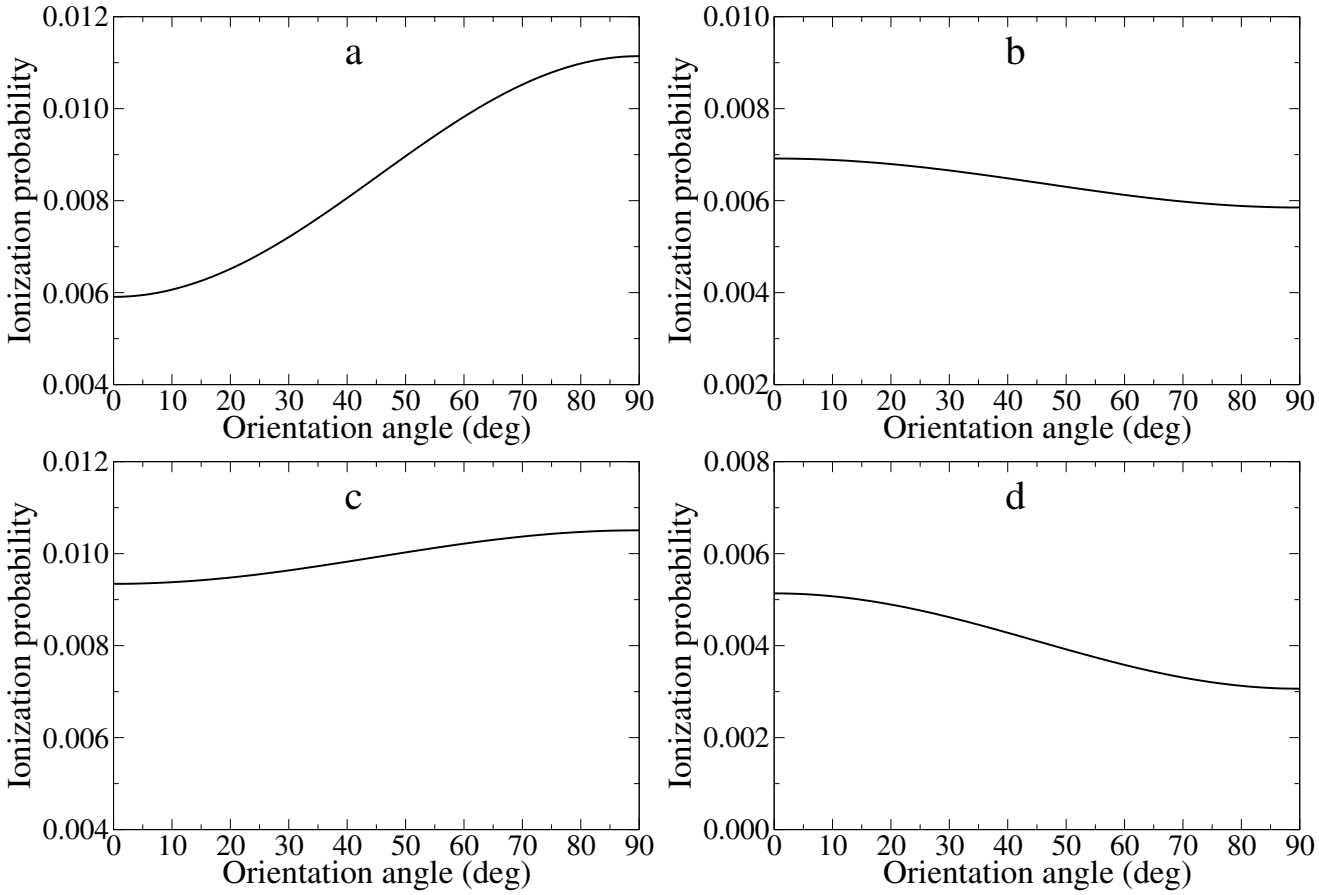

Figure 1.3: Ionization probability H_2^+ as a function of the angle β between the field polarization vector and the molecular axis: (a), initial $1\sigma_u$ state, $R = 2$ a.u., $\lambda = 12.5$ nm; (b), initial $1\sigma_g$ state, $R = 2$ a.u, $\lambda = 11.2$ nm; (c), initial $1\sigma_u$ state, $R = 1.6$ a.u, $\lambda = 12.5$ nm; (d), model atomic ion with $Z = 2.31$, initial $2p_0$ state, $\lambda = 12.5$ nm. The pulse duration is 8 optical cycles and the peak intensity $I_0 = 5 \times 10^{16}$ W/cm^2.

dependence for the initial state $1\sigma_u$ becomes flatter as the internuclear distance decreases. Eventually, the maximum jumps from $\beta = 90°$ to $\beta = 0°$.

Fluctuations in the ratio $P_\perp/P_\parallel$ observed in figure 1.2 and the anomalous orientation dependence of the ionization probability in the wavelength range 6–23 nm for the initial state $1\sigma_u$ for $R = 2$ a.u. can be explained by the effect of two-center interference. A very rough, but useful approximation for the dipole matrix elements can be made by using a linear combination of displaced spherically symmetric orbitals to describe the $1\sigma_u$ state:

$$\Psi_i \approx \Phi(|\mathbf{r} + a\mathbf{e}_z|) - \Phi(|\mathbf{r} - a\mathbf{e}_z|), \tag{1.52}$$

and replace the continuum states with the plane waves $\exp(i\mathbf{k}\cdot\mathbf{r})$). This approximation can be traced back to the early work of Cohen and Fano [80] who studied interference effects in total photoionization cross sections of diatomic molecules. Then the squared matrix elements of the momentum operator (velocity gauge (1.3) is used for the interaction with the external field) have the following approximate expressions:

$$\begin{aligned} |\langle\exp(i\mathbf{k}\cdot\mathbf{r})|\hat{p}_z|\Psi_i\rangle|^2 &\approx 4k_z^2\sin^2(k_z a)\,|\tilde{\Phi}(k)|^2, \\ |\langle\exp(i\mathbf{k}\cdot\mathbf{r})|\hat{p}_x|\Psi_i\rangle|^2 &\approx 4k_x^2\sin^2(k_z a)\,|\tilde{\Phi}(k)|^2, \end{aligned} \tag{1.53}$$

where k_x and k_z are projections of the electron momentum $\mathbf{k}$ on the x and z axes, respectively, and $\tilde{\Phi}(k)$ is a Fourier transform of the spherically symmetric orbital $\Phi(r)$. After integration (1.53) over the angles of the vector $\mathbf{k}$, an analytical approximation for the ratio $P_\perp/P_\parallel$ is obtained:

$$\frac{P_\perp}{P_\parallel} \approx \frac{\varkappa^3 + 3\varkappa\cos\varkappa - 3\sin\varkappa}{\varkappa^3 - 3\varkappa^2\sin\varkappa - 6\varkappa\cos\varkappa + 6\sin\varkappa}, \tag{1.54}$$

where $\varkappa = 2ka$. The function on the right-hand side of (1.54) has an oscillatory dependence on the scaled electron momentum ka (the electron momentum multiplied by the half internuclear distance), which originates from the two-center interference factor in he matrix elements (1.53). Although the oscillatory structure of $P_\perp/P_\parallel$ is qualitatively reproduced by the function (1.54), quantitative agreement between the numerical data and analytical approximation is rather poor, particularly at low scaled electron momenta. The related issues were discussed in the literature with respect to photoionization of H_2^+ in the ground electronic state [81] as well as electron

spectra after above-threshold multiphoton ionization [16] and photon momentum transfer [82]. A conclusion was made that approximations of the initial and final states by a linear combination of atomic orbitals and a free-particle wave function, respectively, are not good enough to reproduce the numerical data accurately [81]. Regarding the plane wave approximation for the final electronic states, it is expected to be not very good at low electron energies (like the Born approximation of the scattering theory). While a rigorous approach to improving the quality of the approximation would be to use more accurate continuum wave functions that include scattering phases, this thesis proposes a simple empirical correction to the model (1.54). The plane wave approximation does not take into account the increase in electron momentum in a potential well near nuclei. This region makes the main contribution to the matrix elements of the momentum operator, calculated by spatial integration in (1.53). To take this effect into account to some extent, the following substitution can be made in the (1.54) function:

$$\varkappa \to \sqrt{\varkappa^2 + \varkappa_0^2}, \tag{1.55}$$

where $\varkappa_0^2$ is a fitting parameter, effectively representing the depth of the potential well. The corrected results for $\varkappa_0^2 = 5.5$ are also shown in figure 1.2. As one can see, agreement with the numerical data is much better in this case. Regarding figure 1.2, right panel, the numerical data for various internuclear distances, presented as functions of the scaled electron momentum ka, are close to each other, which confirms the role of this parameter in describing photoionization.

The energy and angular distributions of the outgoing photoelectrons can also help to understand the two-center interference nature of anomalous orientation dependence of the ionization probability. A simple relation describing the condition of constructive interference of the waves from two centers can be represented in the following form (see, for example, [21], where the effects of two-center interference in high harmonic generation were discussed):

$$ka\cos\theta = \left(n + \frac{1}{2}\right)\pi \quad (n = 0.1, 2\dots). \tag{1.56}$$

Here θ is the electron emission angle relative to the molecular axis. Accordingly, the condition of destructive interference can be written as:

$$ka\cos\theta = n\pi \quad (n = 0.1, 2\dots). \tag{1.57}$$

The formulas (1.56) and (1.57) take into account that the initial wave function $1\sigma_u$ is antisymmetric, giving rise to an additional phase π difference π between the contributions to the ionization amplitude from the vicinities of the two nuclei. As noted above, the destructive interference corresponds to the electron emission angle $\theta = 90^\circ$ irrespective of the internuclear distance and laser wavelength, with $n = 0$ in the formula (1.57). Constructive interference can be achieved if $n = 0$ and $ka > \pi/2$ in the formula (1.56). The value $ka = \pi/2$ agrees well withthe beginning of the region of anomalous dependence, shown in figure 1.2 (the right picture). If $\lambda < 8$ nm, the destructive interference condition (1.57) can be satisfied with $n = 1$. Initially at $\lambda = 8$ nm, the corresponding emission angle is $\theta = 0^\circ$, suppressing the electron emission along the molecular axis and still favoring the anomalous orientation dependence of the ionization probability. However, at shorter wavelengths, this destructive interference minimum is shifted to larger emission angles. Eventually, around $\lambda = 6$ nm, the pattern in the orientation dependence changes as seen in figure 1.2. At even shorter wavelengths, multiple interference minima and maxima give rise to alternating wavelength intervals with $P_\perp > P_\parallel$ and $P_\perp < P_\parallel$.

To illustrate the effect of constructive interference on the angular distributions of photoelectrons, energy and emission angle distributions were plotted for a wavelength $\lambda = 12.5$ nm. The same wavelength was used in the calculations of the photoelectron spectra for the circularly polarized laser pulses [37]. In this case, according to (1.56), the interference maximum should be observed at the emission angle $\theta \approx 50^\circ$ (and also for the angle $\theta = 180^\circ - 50^\circ = 130^\circ$ if the angle θ is measured from the selected positive direction of the z axis). If the electron escapes along the molecular axis ($\theta = 0^\circ$ или $\theta = 180^\circ$) upon ionization of H_2^+, the phase difference between the waves coming from the vicinities of the nuclei makes the differential ionization probability weaker by a factor of 2.4 compared to the largest possible value at $\theta = 50^\circ(130^\circ)$. As a result, in the case of the parallel orientation of the molecular axis ($\beta = 0^\circ$), where the photoelectrons should be ejected predominantly along the molecular axis, the total ionization is also suppressed. These considerations are illustrated by the distributions of photoelectrons with respect to their energies and emission angles presented in figure 1.4. The distributions are shown in the $x - z$ plane, where both the molecular axis and the laser electric field vector lie. Such a plane is not uniquely defined for the parallel orientation of the molecule

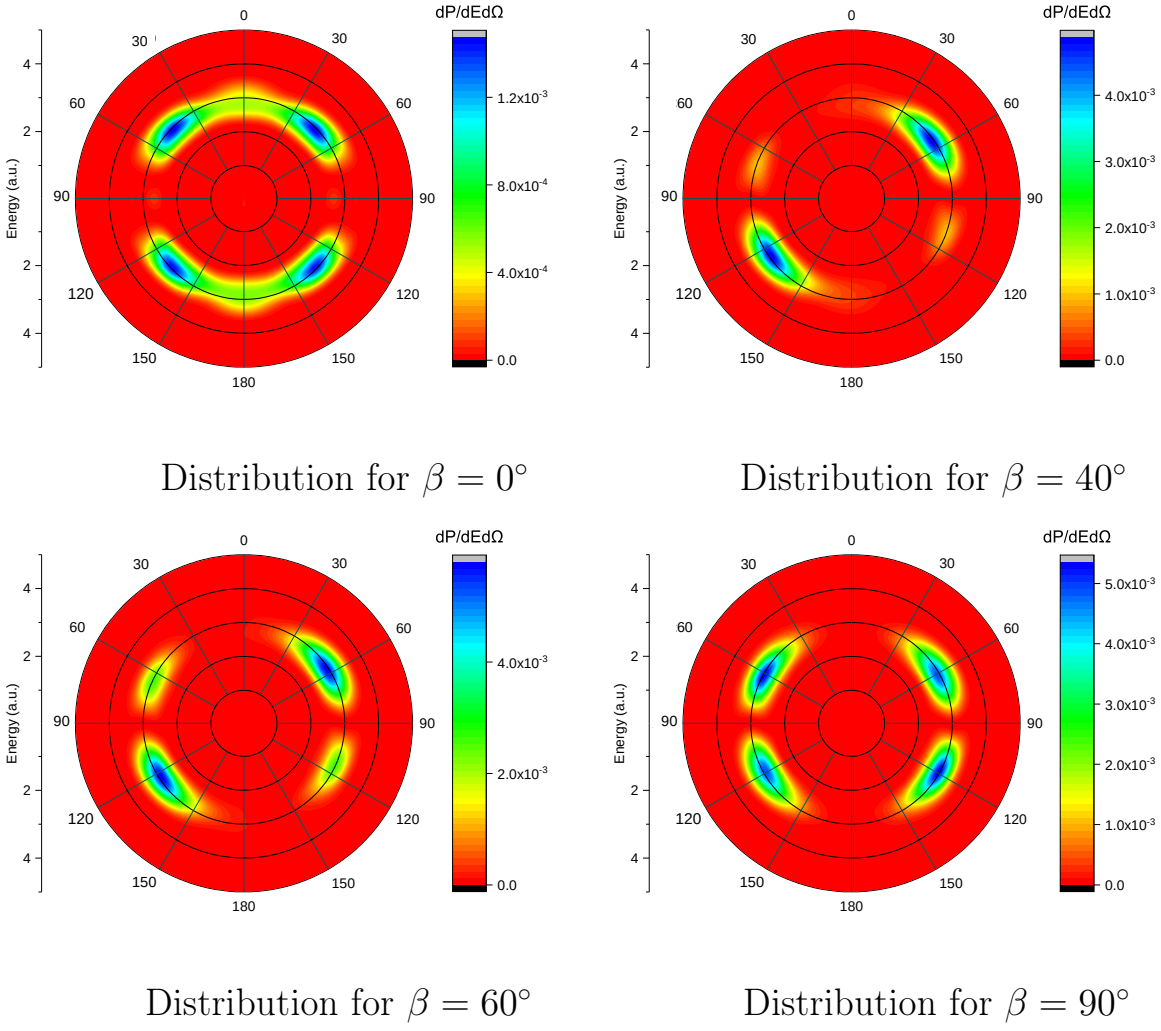

Figure 1.4: Energy and angular distributions of photoelectrons for the H_2^+ molecule prepared in the $1\sigma_u$ state by a linearly polarized pulse with a wavelength of 12.5 nm and a peak intensity of 5×10^{16} W/cm^2 for various orientations of the molecular axis.

($\beta = 0°$), but in this case the electron distributions are invariant with respect to rotation about the z axis and look the same in any plane which contains this axis. In figure 1.4 (and also in figures 1.5 and 1.6 below) the right half-planes of all panels correspond to the positive semiaxis x, where the azimuthal angle $\phi = 0°$. The left half-planes correspond to the negative semiaxis x, where $\phi = 180°$.

The energy distributions in Figure 1.4 describe the first peak of above-threshold ionization, with a maximum at the electron kinetic energy $E = 2.98$ a.u. The width of this peak in the energy region is determined mainly by the width of the frequency spectrum of the laser pulse. With a parallel orientation of the molecule ($\beta = 0°$), the maximum is located not in the direction of the axis of the molecule and the polarization vector of the laser field [$\theta = 0°(180°)$], and for $\theta \approx 45°(135°)$. Such a

position of the maximum is due to the balance of two factors: on the one hand, the electric field of the laser is directed along the molecular axis and tends to knock out the electron in this direction, and on the other hand, the greatest amplification of the signal due to the constructive interference takes place at $\theta = 50°$. Similar angular distributions of electrons at $\beta = 0°$ were obtained and explained by the presence of a two-center interference maximum in the work of [38], where the two-dimensional model H_2^+ was used. For the orientations $\beta = 40°$ and $\beta = 60°$, the maximum in the angular distribution is located in the vicinity of $\theta = 50°$, that is, in the direction of the strongest constructive interference and close to the polarization direction of the external field. Finally, at $\beta = 90°$, the maximum in the angular distribution is located approximately at $\theta = 60°(120°)$. As in the case of $\beta = 0°$, this is due to the balance of two factors: on the one hand, suppression of the electron emission perpendicular to the molecular axis due to the destructive interference, and on the other hand, constructive interference at $\theta = 50°$. In this case, the total ionization probability turns out to be higher than for $\beta = 0°$. As a result, an anomalous dependence of the total ionization probability on the orientation of the molecule emerges, as shown in figure 1.3.

Figure 1.5 displays the distributions of photoelectrons with respect to the energy and emission angle after ionization of H_2^+ initially in the $1\sigma_u$ state by a pulse with the wavelength 39 nm and peak intensity of 5×10^{14} W/cm^2, figure 1.6 shows similar distributions for the ionization of an atomic ion with the nuclear charge $Z = 2.31$ for the initial state $2p_0$ by a laser pulse with the wavelength $\lambda = 12.5$ nm and peak intensity 5×10^{16} W/cm^2. In both cases, for the orientation, $\beta = 0°$ one can see a prominent maximum in the photoelectron angular distribution at the emission angle $\theta = 0°(180°)$. At the laser wavelength $\lambda = 39$ nm, the two-center interference pattern in H_2^+ does not contain a maximum inside the emission angle interval $[0°, 90°]$, and the differential ionization probability decreases monotonically as the emission angle changes from 0° to 90°. At $\theta = 90°$, the differential ionization probability is close to zero due to the destructive two-center interference. For the atomic ion (figure 1.6, $\beta = 0°$), there is no two-center interference, and a local maximum in the angular distribution is observed at the emission angle $\theta = 90°$, although this maximum is less pronounced than the main maximum at $\theta = 0°$. When the orientation angle β is changed from 0° to 90°, the main maximum in the

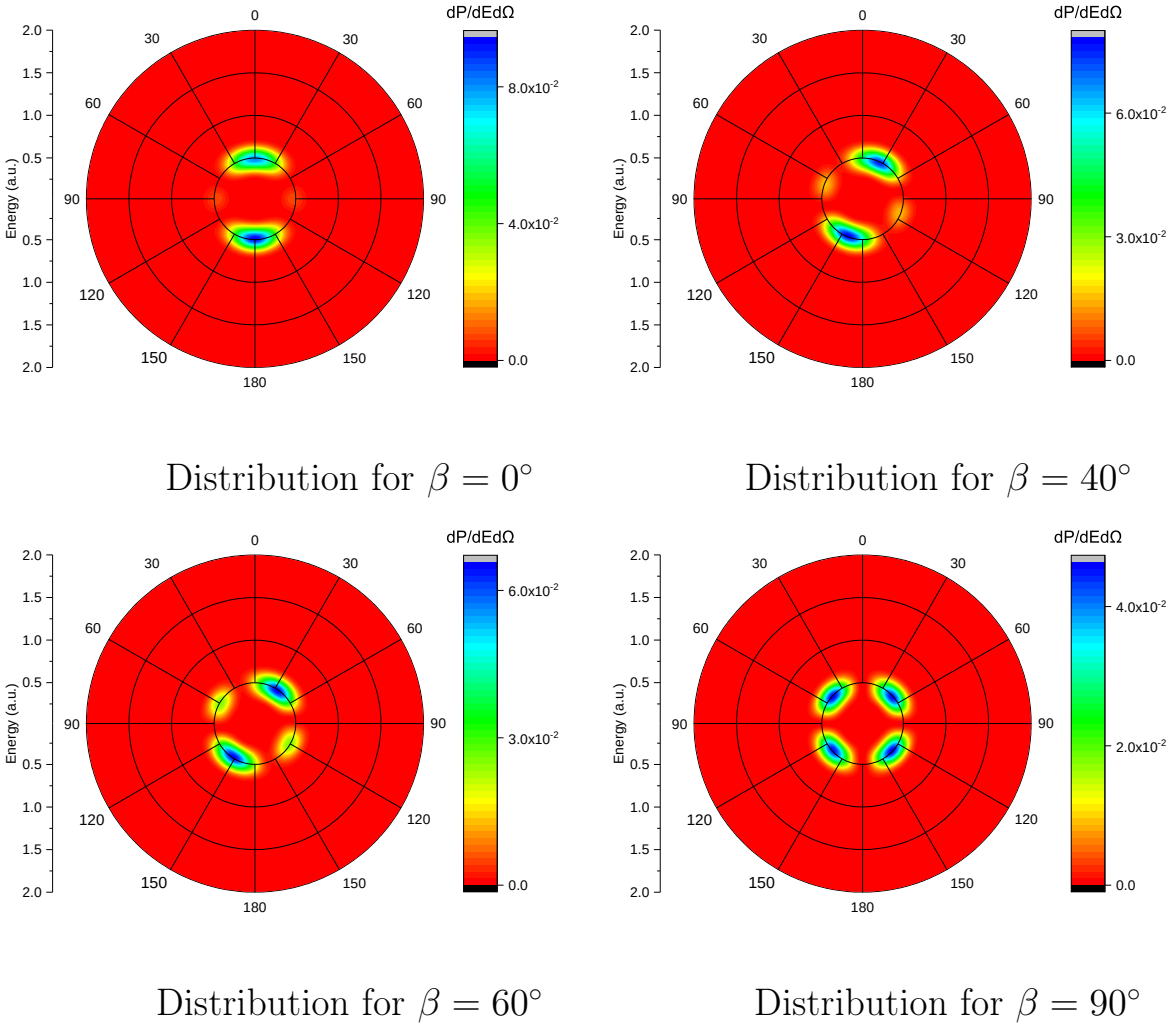

Figure 1.5: Energy and angular distributions of photoelectrons for the H_2^+ molecule prepared in the $1\sigma_u$ state by a linearly polarized pulse with a wavelength of 39 nm and a peak intensity of 5×10^{14} W/cm^2 for various orientations of the molecular axis.

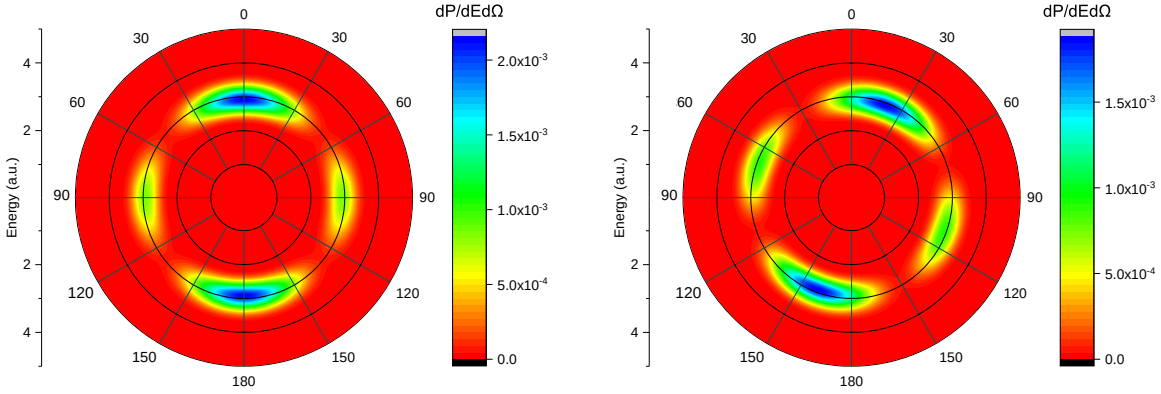

distribution for $\beta = 0°$

distribution for $\beta = 40°$

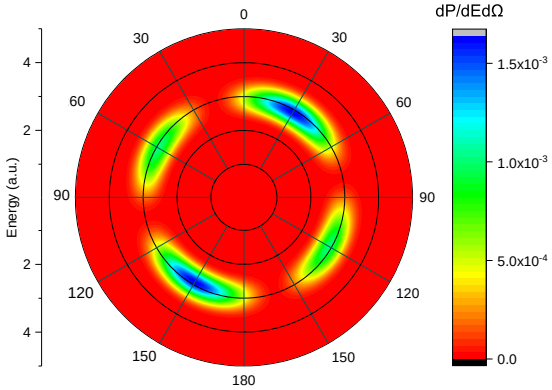

Distribution for $\beta = 60°$

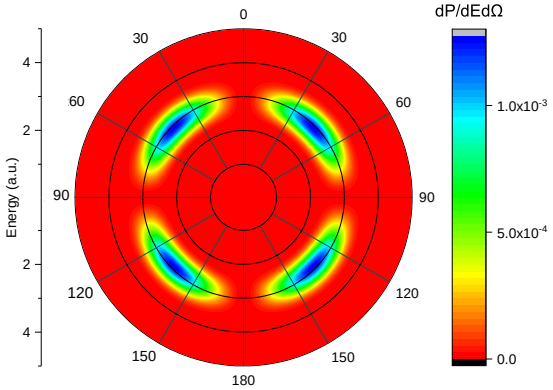

Distribution for $\beta = 90°$

Figure 1.6: Energy and angular distributions of photoelectrons during ionization of a model atomic ion with a nuclear charge of $Z = 2.31$, initially prepared in the $2p_0$ state, by a linearly polarized pulse with a wavelength of 12.5 nm and a peak intensity of 5×10^{16} W/cm^2 for various angles between the polarization vector of the laser field and the z axis.

angular distribution is gradually shifted from $\theta = 0°(180°)$ to $\theta = 45°(135°)$.

1.5 Chapter 1 Summary

This chapter of the dissertation considers the effect of two-center interference on the process of ionization of the H_2^+ molecule prepared in the $1\sigma_u$ excited electronic state by a linearly polarized laser pulse with a carrier wavelength in the far ultraviolet region . The result of such interference, in the wavelength range of $6 - -23$ nm, is an anomalous dependence of the ionization probability on the orientation of the molecule axis, in which the maximum ionization probability is observed when the molecule is perpendicular to the polarization of the external field, and ionization is, on the contrary, suppressed when the orientation is parallel. In this case, the angular distributions of photoelectrons exhibit a minimum for the emission angle along the molecular axis. Typically, the effect of two-center interference is associated with the destructive nature of such interference, which leads to the appearance of a minimum in the differential ionization probability or harmonic spectrum. In this case, constructive interference takes place, which enhances the flow of emitted electrons at a certain angle in the range from 0° to 90° relative to the same flow along the axis of the molecule. As a result, the maximum in the angular distribution of photoelectrons shifts from the molecular axis, even if this axis is parallel. As a consequence, the total ionization probability for parallel orientation also has a minimum. The position of the interference maximum in the angular distribution of photoelectrons is well described by a simple formula for the interference of waves from two point sources, the distance between which is equal to the internuclear distance in the molecule. Based on this formula, it is possible to estimate the upper limit of laser wavelengths at which the maximum constructive interference of electrons emitted from the vicinity of two nuclei at any angle from the interval $[0°, 90°]$ is observed. For the initial state $1\sigma_u$ and internuclear distance $R = 2$ a.u. this boundary is equal to 24 nm. For large wavelengths, there is no such constructive interference, and the maximum of the differential ionization probability for a parallel orientation corresponds to the direction along the axis of the molecule. The anomalous dependence of the total ionization probability on orientation then disappears, which is confirmed by calculations for a wavelength of 39 nm.

Chapter 2. Multiphoton Ionization of one-electron relativistic Diatomic molecules in strong laser fields

This chapter of the dissertation is devoted to the study of relativistic effects in single-electron quasimolecules exposed to an external field and effects arising from going beyond the dipole approximation. To do this, the Dirac equation is solved in prolate spheroidal coordinates using the numerical methods outlined in the previous chapter. The Schrödinger equation with Coulomb nucleus-electron interaction allows scaling with respect to the nuclear charge Z in the dipole approximation, while the Dirac equation is not invariant under such a transformation. The difference in results predicted by the Schrödinger equation and the Dirac equation is identified with relativistic effects. It is expected that the role of relativistic effects increases with increasing nuclear charge Z, due to such effects as the deepening of the energy level of the ground state with increasing Z, relativistic shift of the resonant frequency.

The end of the chapter is devoted to going beyond the dipole approximation and studying the resulting effects that change the dynamics of ionization.

2.1 Time-dependent Dirac equation for a one-electron quasimolecule in a linearly polarized electromagnetic field

For the purposes of this chapter of the dissertation, it is necessary to solve the nonstationary Dirac equation for a one-electron quasimolecule. The time-dependent Dirac equation for the electron interacting with the atomic core and external electromagnetic field reads as:

$$i\frac{\partial}{\partial t}\Psi(\mathbf{r},t) = [H_0 + V(\mathbf{r},t)]\Psi(\mathbf{r},t), \tag{2.1}$$

where $\Psi(\mathbf{r},t)$ is a four-component wave function and the unperturbed Hamiltonian H_0 takes the form:

$$H_0 = c(\alpha \cdot \mathbf{p}) + m_e c^2 \beta + UI_4. \tag{2.2}$$

where c is the speed of light, $\mathbf{p}$ is the momentum operator, m_e is the electron mass, U is the atomic potential of nuclei, I_4 is the 4x4 diagonal unit matrix, and α and β Dirac matrices:

$$\beta = \begin{pmatrix} I & 0 \\ 0 & -I \end{pmatrix}, \quad \alpha = (\alpha_x, \alpha_y, \alpha_z), \tag{2.3}$$

$$\alpha_x = \begin{pmatrix} 0 & 0 & 0 & 1 \\ 0 & 0 & 1 & 0 \\ 0 & 1 & 0 & 0 \\ 1 & 0 & 0 & 0 \end{pmatrix}, \quad \alpha_y = \begin{pmatrix} 0 & 0 & 0 & -i \\ 0 & 0 & i & 0 \\ 0 & -i & 0 & 0 \\ i & 0 & 0 & 0 \end{pmatrix}, \quad \alpha_z = \begin{pmatrix} 0 & 0 & 1 & 0 \\ 0 & 0 & 0 & -1 \\ 1 & 0 & 0 & 0 \\ 0 & -1 & 0 & 0 \end{pmatrix}. \tag{2.4}$$

The interaction with the external field V is written as:

$$V = (\alpha \cdot \mathbf{A}). \tag{2.5}$$

In the formula (2.5) $\mathbf{A}(\mathbf{r}, t)$ is the vector potential, which is selected in the Coulomb gauge $(\nabla \cdot \mathbf{A}) = 0$. When choosing an electromagnetic field linearly polarized along the z axis, only one term remains in the expression (2.5):

$$V = A(\mathbf{r}, t) \begin{pmatrix} 0 & 0 & 1 & 0 \\ 0 & 0 & 0 & -1 \\ 1 & 0 & 0 & 0 \\ 0 & -1 & 0 & 0 \end{pmatrix} \tag{2.6}$$

It turns out to be convenient to make the following transformation of the wave function

$$\mathbf{\Psi} \equiv \begin{pmatrix} \psi_1 \\ \psi_2 \\ \psi_3 \\ \psi_4 \end{pmatrix} = \begin{pmatrix} \tilde{\psi}_1 \\ \tilde{\psi}_2 exp(i\phi) \\ i\tilde{\psi}_3 \\ i\tilde{\psi}_4 exp(i\phi) \end{pmatrix}. \tag{2.7}$$

ϕ-azimuthal angle describing rotation around the z axis. With this transformation, the Unperturbed Hamiltonian takes the following form:

$$\tilde{H}_0 = m_e c^2 \begin{pmatrix} 1 & 0 & 0 & 0 \\ 0 & 1 & 0 & 0 \\ 0 & 0 & -1 & 0 \\ 0 & 0 & 0 & -1 \end{pmatrix} + c \begin{Vmatrix} 0 & B \\ B^\dagger & 0 \end{Vmatrix} + c \begin{Vmatrix} 0 & D \\ D^\dagger & 0 \end{Vmatrix} + U \begin{Vmatrix} 1 & 0 \\ 0 & 1 \end{Vmatrix}. \tag{2.8}$$

In the equation (2.8), the notations B and D correspond to 2x2 matrices, which in prolate spheroidal coordinates have the form:

$$B = \begin{pmatrix} +\frac{\eta(\xi^2-1)}{a(\xi^2-\eta^2)}\frac{\partial}{\partial\xi} + \frac{\xi(1-\eta^2)}{a(\xi^2-\eta^2)}\frac{\partial}{\partial\eta} & \frac{\sqrt{(\xi^2-1)(1-\eta^2)}}{a(\xi^2-\eta^2)}[\xi\frac{\partial}{\partial\xi} - \eta\frac{\partial}{\partial\eta}] \\ \frac{\sqrt{(\xi^2-1)(1-\eta^2)}}{a(\xi^2-\eta^2)}[\xi\frac{\partial}{\partial\xi} - \eta\frac{\partial}{\partial\eta}] & -\frac{\eta(\xi^2-1)}{a(\xi^2-\eta^2)}\frac{\partial}{\partial\xi} - \frac{\xi(1-\eta^2)}{a(\xi^2-\eta^2)}\frac{\partial}{\partial\eta} \end{pmatrix}, \tag{2.9}$$

$$D = \begin{pmatrix} 0 & -\frac{i}{a\sqrt{(\xi^2-1)(1-\eta^2)}}\frac{\partial}{\partial\phi} + \frac{1}{a\sqrt{(\xi^2-1)(1-\eta^2)}} \\ \frac{i}{a\sqrt{(\xi^2-1)(1-\eta^2)}}\frac{\partial}{\partial\phi} & 0 \end{pmatrix}. \tag{2.10}$$

The interaction operator V, after transforming the wave function, takes the following form:

$$\tilde{V} = A(\mathbf{r}, t) \begin{pmatrix} 0 & 0 & i & 0 \\ 0 & 0 & 0 & -i \\ i & 0 & 0 & 0 \\ 0 & -i & 0 & 0 \end{pmatrix}. \tag{2.11}$$

Now for the four-component wave function $\tilde{\psi}$, representable as:

$$\tilde{\Psi} \equiv \begin{pmatrix} \tilde{\psi}_1 \\ \tilde{\psi}_2 \\ \tilde{\psi}_3 \\ \tilde{\psi}_4 \end{pmatrix}. \tag{2.12}$$

The Dirac equation takes the form:

$$i\frac{\partial}{\partial t}\tilde{\Psi} = [\tilde{H}_0 + \tilde{V}]\tilde{\Psi}, \tag{2.13}$$

the wave function $\tilde{\Psi}$ can be expanded in a Fourier series as a function of the azimuthal angle ϕ:

$$\tilde{\Psi} = \sum_{m=-\infty}^{\infty} \exp(im\phi)\tilde{\Psi}^{(m)}. \tag{2.14}$$

Each term on the right side corresponds to the projection onto the z axis, $M = m + 1/2$ of the total angular momentum. The Hamiltonian $\tilde{H}_0^{(m)}$ is completely real and can be represented as:

$$\begin{aligned}\tilde{H}_0^{(m)} = m_e c^2 \begin{pmatrix} 1 & 0 & 0 & 0 \\ 0 & 1 & 0 & 0 \\ 0 & 0 & -1 & 0 \\ 0 & 0 & 0 & -1 \end{pmatrix} + c \begin{Vmatrix} 0 & B \\ B^\dagger & 0 \end{Vmatrix} \\ + c \begin{Vmatrix} 0 & D_m \\ D_m^\dagger & 0 \end{Vmatrix} + U \begin{Vmatrix} 1 & 0 \\ 0 & 1 \end{Vmatrix}\end{aligned}. \tag{2.15}$$

Where the matrix D_m can be represented as:

$$D_m = \begin{pmatrix} 0 & \frac{m+1}{a\sqrt{(\xi^2-1)(1-\eta^2)}} \\ -\frac{m}{a\sqrt{(\xi^2-1)(1-\eta^2)}} & 0 \end{pmatrix} \tag{2.16}$$

If the field is considered in the dipole approximation and the field is linearly polarized along the molecular axis, the projection of the angular momentum onto the z axis is preserved. For an initial state with a certain angular momentum projection, only one term with the corresponding value of m needs to be retained in the equation

$$\tilde{H}_0^{(m)}\tilde{\Psi}_n^{(m)} = E_n^{(m)}\tilde{\Psi}_n^{(m)}. \tag{2.17}$$

2.2 Electron interaction potential with nuclei

The finite size of the nuclei may not be taken into account for the molecule H_2^+ under the influence of an electromagnetic field and the coulomb interaction operator can be used:

$$U(\mathbf{r}) = -\frac{Z}{\mathbf{r}+\mathbf{a}} - \frac{Z}{\mathbf{r}-\mathbf{a}}, \tag{2.18}$$

where $\mathbf{a}$ is a vector directed along the molecular axis and equal to half the internuclear distance:

$$\mathbf{a} = \frac{1}{2}R\mathbf{e}_z, \tag{2.19}$$

vector $\mathbf{e}_z$ is a unit vector along the molecular axis z. charge $Z = 1$ (for molecule H_2^+). For nuclei with large charges, the point nucleus approximation is no longer applicable, since such an approximation leads to an ever-increasing error in calculations with increasing nuclear charge Z due to the singularity of the wave function on the nuclei of the molecule. The interaction potential is determined by the nuclear charge distribution $\rho_n(\mathbf{r})$:

$$U(\mathbf{r}) = -\int d^3r' \frac{\rho_n(\mathbf{r}' + \mathbf{a})}{|\mathbf{r} - \mathbf{r}'|} - \int d^3r' \frac{\rho_n(\mathbf{r}' - \mathbf{a})}{|\mathbf{r} - \mathbf{r}'|}. \tag{2.20}$$

In this work, the spherically symmetric Fermi distribution is used to describe the nuclear charge density distribution [83]:

$$\rho_n(r) = \rho_0 \frac{1 + \exp[-r_0/b]}{1 + \exp[(r - r_0)/b]} \tag{2.21}$$

where the parameter b is set to $2.3/(4ln3)$ fm [83] and parameters ρ_0 and r_0 are calculated given the total nucleus charge Z and experimental values of the nucleus root mean square radius [84]. Note that the potential (2.20) with the smooth nuclear charge distribution (2.21) does not have Coulomb singularities at the nuclei centers r=$\pm a$, hence the Dirac wave function is also regular there.

2.3 Type of vector potential

When studying multiphoton ionization, a linearly polarized laser field is used and the vector potential $\mathbf{A}$ is assumed to be directed along the z axis, which is parallel to the molecular axis. In the dipole approximation, the laser pulse has a Gaussian form:

$$A(t) = \frac{cF_0}{\omega} \exp\left(-2\ln 2(\frac{t^2}{\tau^2})\right) \sin(\omega t). \tag{2.22}$$

In the formula (2.22) F_0 is the peak electric field strength, τ has the meaning of full width at half maximum (FWHM). For all calculations, τ was chosen to be equal to:

$$\tau = 7.5\frac{\pi}{\omega}. \tag{2.23}$$

Therefore, the FWHM value was equal to 3.75 optical cycles. Outside the dipole approximation, the vector potential depends on both time and spatial coordinates and the vector potential (2.22) should be modified using the following substitution:

$$t \to t - \frac{x}{c}. \tag{2.24}$$

With this substitution, the vector potential satisfies the wave equation for electromagnetic fields in vacuum and describes a laser pulse linearly polarized in the z direction and propagating in the x direction. As shown in [57], it is most important to preserve spatial dependence of the pulse envelope, since non-dipole effects in the pulse envelope provide the dominant contribution (relative to the contribution of the pulse carrier) beyond the dipole approximation.

2.4 Numerical solution of the nonstationary Dirac equation

First, the stationary Dirac equation is solved to obtain the energies and wave functions of the bound states. To numerically solve the stationary Dirac equation, the methods described in Chapter 1 are used. The evolution of the wave function in time, after solving the stationary equation, can be described by two different methods. The first is the split operator method in the energy representation [77], which is also used to solve the non-stationary Schrödinger equation [85, 86]. The following scheme is used to describe the evolution of the wave function:

$$\begin{aligned}\tilde{\Psi}(t+\Delta t) = \exp\left(-i\frac{1}{2}\Delta t\tilde{H}_0\right)\times \\ \exp\left(-i\Delta t\tilde{V}(t+\frac{1}{2}\Delta t)\right)\exp\left(-i\frac{1}{2}\Delta t\tilde{H}_0\right)\tilde{\Psi}(t).\end{aligned} \tag{2.25}$$

The expression $\exp\left(-i\frac{1}{2}\Delta t\tilde{H}_0\right)$ is a free propagator. The free propagator can be expressed in terms of propagators corresponding to specific angular momentum projections:

$$\exp\left(-i\frac{1}{2}\Delta t\tilde{H}_0\right)\tilde{\Psi}(t) = \sum_{m=-\infty}^{\infty}\exp(im\phi)\exp\left(-i\frac{1}{2}\Delta t\tilde{H}_0^m\right)\Psi^m(t). \tag{2.26}$$

The propagator $\exp\left(-i\frac{1}{2}\Delta t\tilde{H}_0^m\right)$ is sought in the form of a spectral decomposition:

$$\exp\left(-i\frac{1}{2}\Delta t\tilde{H}_0^m\right) = \sum_n \exp\left(-i\frac{1}{2}\Delta t E_n^{(m)}\right)|\tilde{\Psi}_n^{(m)}\rangle\langle\tilde{\Psi}_n^{(m)}|, \tag{2.27}$$

where the wave functions $\tilde{\Psi}_n^{(m)}$ and energies $E_n^{(m)}$ are found as a solution to the eigenvalue problem of the equation (2.17). The equation (2.26) is very useful for calculations beyond the dipole approximation, where the projection of angular momentum

is not conserved: in the matrix-vector product, this allows the use of several lower-dimensional matrices (partial propagators) rather than a single higher-dimensional matrix (full propagator). The external field propagator $\exp\left(-i\Delta t\tilde{V}\right)$ can be represented analytically as:

$$\exp\left(-i\Delta t\tilde{V}\right) = \begin{Vmatrix} \cos(A\Delta t) & \sin(A\Delta t)\sigma_z \\ -\sin(A\Delta t)\sigma_z & \cos(A\Delta t) \end{Vmatrix} \tag{2.28}$$

In coordinate representation, where the angle is discretized on a uniform grid, the matrix is quasi-diagonal in the sense that it consists of four square blocks, each of which represents a diagonal matrix. The field propagator is time-dependent and must be calculated at each time step. However, this operation does not require much time, since the propagator matrix is quasi-diagonal. Before applying partial free propagators at each time step, the wave function must be converted from a full coordinate representation to an angular momentum projection representation. This is done using the fast Fourier transform along the ϕ coordinate. This operation is performed by hardware-optimized FFT (fast Fourier transform) procedures and does not take much time.

Another method is based on the application of the Crank-Nicholson algorithm, which was used in the first chapter of the dissertation to solve the Schrödinger equation. For the Dirac equation, the evolution of the wave function is described as follows:

$$\begin{aligned} &\left[1 + \frac{i}{2}\Delta t\tilde{H}\left(t + \frac{1}{2}\Delta t\right)\right]\tilde{\Psi}(t + \Delta t) \\ &= \left[1 - \frac{i}{2}\Delta t\tilde{H}\left(t + \frac{1}{2}\Delta t\right)\right]\tilde{\Psi}(t), \end{aligned} \tag{2.29}$$

where $\tilde{H}(t) = \tilde{H} + \tilde{V}(t) - m_e c^2$ is the complete time-dependent Hamiltonian without the rest energy of the electron. Calculating the wave function at each time step in this method involves not only multiplying a matrix by a vector, but also solving a system of linear equations, so it requires more time than in the split operator method. On the other hand, when the large energy $m_e c^2$ is removed from the upper half of the diagonal of the Hamiltonian and transitions to the continuum of negative energies are negligible, the time step can be greatly increased without loss of calculation accuracy.

As has been verified numerically, the time step can be set to approximately 100

times larger than the split operator method to achieve the same level of accuracy, significantly reducing the overall number of time steps. In the dipole approximation, where the dimension of the full Hamiltonian matrix is reduced to the dimension of the partial Hamiltonian for a particular value of m, it turns out that the Crank–Nicholson propagator works better for medium matrix sizes, while the split operator propagator is more efficient for large matrices. Beyond the dipole approximation, it turns out to be more advantageous to use the split operator method, since the Crank-Nicholson method uses a matrix with a full Hamiltonian having a dimension several times larger than the dimension of the partial Hamiltonians. As the wave function evolves in time, it propagates to the boundaries of the spatial domain. To prevent nonphysical reflection of the wave function from the boundaries of the spatial domain, the wave function at each step is multiplied by a mask function, which smoothly decreases to zero towards the boundaries of the spatial domain:

$$\begin{gathered} F(\xi) = \cos\left(\frac{\pi(\xi - R_m}{2(R_b - R_m)}\right)^{1/4} \quad (R_b - R_m) \leqslant \xi \\ F(\xi) = 1 \quad 1 \leqslant \xi < (R_b - R_m), \end{gathered} \tag{2.30}$$

where R_m is a parameter that determines the value ξ at which the mask function begins to decrease.

2.5 Results of the eigenvalue problem for the Dirac equation.

The solution of the non-stationary Dirac equation (2.17) is carried out in a spatial domain, the linear size of which is limited to $50/Z$ a.u. for a quasimolecule with nuclear charge Z. Numerical calculations demonstrate that this size of the spatial region is sufficient for a correct description of the dynamics of ionization in a laser field in further non-stationary calculations. The classical electron excursion distance in a laser field can be estimated by the expression F_0/ω^2, this number is significantly less than $50/Z$ a.u. for all quasimolecules and laser field parameters used in this chapter. The calculations use a moderate number of collocation points: 70 points for the ξ coordinate and 32 points for the η coordinate to allow subsequent non-stationary calculations with partial propagators. The linear dimension of the partial Hamiltonian matrix for any m is equal to 8960. The eigenvalues of the energy of the first few bound states turn out to be quite accurate. For example, the error in

calculating the eigenvalues H_2^+ with $m = 0$ given in table 2.1 is estimated as 10^{-10} a.u. To evaluate the convergence of the eigenvalues, another calculation was carried out with a large number of collocation points (96 points for ξ and 48 points for η). The obtained results are compared with results from the literature. All calculations use the speed of light c = 137.035999139 a.u. (2014 CODATA recommended inverse fine structure constant).

It is well known that the numerical solution of the stationary Dirac equation using basis set expansions leads to the appearance of spurious eigenstates among the true bound states in a discrete region of the spectrum [87]. To eliminate such undesirable states, various methods have been proposed, from imposing special boundary conditions [88, 89] to using kinetically balanced basis sets. However, spurious states do not appear when generalized pseudospectral methods in prolate spheroidal coordinates are used to solve the Dirac eigenvalue problem with the numerical parameters used in the present calculations, at least among the first 35 bound states (due to the finite size of the spatial domain, highly excited bound states may not be accurate in any case). The energies listed in table 2.1 are a fragment of the sequential eigenvalues returned by the computational program without any steps to remove spurious states. The same is true for calculations of atomic hydrogen in prolate spheroidal coordinates, as opposed to calculations in spherical coordinates, where some eigenvalues are duplicated due to the presence of spurious states. Previously, the absence of spurious states in two-center Coulomb systems treated with kinetically balanced B-spline basis sets in prolate spheroidal coordinates was reported in [94].

Table 2.1: Energies of the ground and low-lying excited states H_2^+ (in a.u.) for the projection of the total angular momentum $M = 1/2$ at $R = 2$ a.u. A–calculation with grid 70×32; B – calculation with grid 96×48; C – other calculations. All results were obtained for point nuclei.

State	A	B	C
$1\sigma_g$	-1.1026415810753	-1.1026415810315	-1.102641581032 [90]
			-1.1026415810336 [91]
$1\sigma_u$	-0.6675527720388	-0.6675527719950	-0.667552771996 [92]
			-0.6675527719955 [91]
$1\pi_u$	-0.4287811602120	-0.4287811602141	-0.428781160 [93]
			-0.4287811584 [94]
$2\sigma_g$	-0.3608710705821	-0.3608710705758	-0.3608710705784 [91]
			-0.3608710695 [94]
$2\sigma_u$	-0.2554197047559	-0.2554197047496	-0.255419705 [93]
			-0.2554197033 [94]
$3\sigma_g$	-0.23578126845559	-0.2357812684555	-0.2357812681 [94]

2.6 Nonrelativistic scaling and relativistic effects in quasimolecules

It is well known that the nonstationary Schrödinger equation satisfies exact scaling relations with respect to the nuclear charge parameter Z in such a way that the result of numerical calculations of the interaction of matter with an external field remains unchanged for any nuclear charge Z [95]. For quasimolecules, this scaling of the spatial, temporal, and momentum variables in the equation transforms the equation for a molecule with nuclear charges Z into an equation for H_2^+ ($Z = 1$). This non-relativistic scaling is performed by the following transformation of the system parameters:

$$\begin{aligned} r = \tilde{r}/Z, \quad R = \tilde{R}/Z, \\ t = \tilde{t}/Z^2, \quad \omega = \tilde{\omega} Z^2, \\ F_0 = \tilde{F}_0 Z^3. \end{aligned} \tag{2.31}$$

Variables and parameters with a tilde correspond to a quasimolecule with a nuclear charge of Z=1, i.e. a molecule H_2^+. Exact scaling with the nuclear charge does not hold for relativistic systems described by the Dirac equation, although some approximate relations have been suggested [52]. Strictly speaking, the scaling (2.31)

does not hold exactly even for the time-dependent Schrödinger equation, if the electron–nucleus interaction is described within the extended nucleus model, and not by the pure Coulomb potential. However, because of the large difference between the electronic and nuclear length scales, the effect of the finite nucleus dimension on the electronic motion is very small. Even for the heaviest nucleus used in our calculations ($Z = 92$), the relative shift of the ground electronic state energy level due to the extended nuclear charge distribution does not exceed 10^{-4}, therefore the deviation from the nonrelativistic scaling relations caused by the finite nucleus size is insignificant.

Generally, any difference between the time-dependent Dirac equation predictions and the corresponding time-dependent Schrödinger equation results for the same system can be attributed to relativistic effects. As discussed in [52], for multiphoton ionization of hydrogen-like ions, the main effect is the shift of the ionization potential (the latter becomes larger in the relativistic case). For quasimolecules, this shift depends also on the internuclear distance. n figure 2.1 shows the scaled difference between the relativistic and non-relativistic energies of the ground state $1\sigma_g$ for several quasimolecules used in the calculations. For the quasimolecules with $Z \neq 1$, the nonrelativistic energies are calculated from the H_2^+ data with the help of the scaling relations (2.31), thus not taking into account the finite nucleus size. The energy difference depicted in figure 2.1 therefore includes both corrections, due to the relativistic effects and extended nuclear charge distribution. However, as mentioned earlier, the last correction is small and can be neglected for all quasimolecules used in the calculations. For H_2^+ the relativistic correction is also small, and the energy difference is not visible in figure 2.1. For the heavier quasimolecules, the difference between the relativistic and nonrelativistic ground state energies gradually increases with the nuclear charge Z. As expected, it also becomes larger at smaller internuclear distances where the relativistic ground state energy level approaches the negative continuum boundary if the nuclear charge Z is large enough. In the united atom limit $R \to 0$, the core charge is equal to $2Z$ and may exceed the critical value ≈ 170. At this critical charge, the ground state energy level dives into the negative continuum and spontaneous electron–positron pair creation takes place [96].

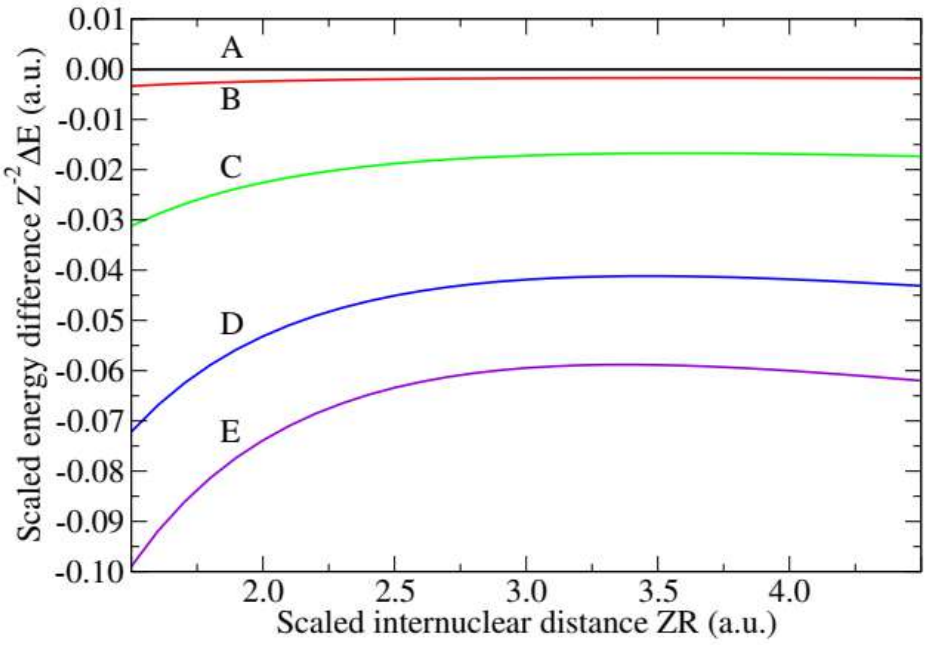

Figure 2.1: Scaled difference between relativistic and non-relativistic ground state energies $1\sigma_g$ for several one-electron homonuclear quasimolecules with nuclear charge Z: (A), Z=1; (B), Z=18; (C), Z=54; (D), Z=80; (E), Z=92.

2.7 Multiphoton ionization of quasimolecules in the dipole approximation

For relatively low carrier frequencies (when the wavelength considerably exceeds the molecular size), the dipole approximation is well justified. This section presents the results of calculations of multiphoton ionization for several quasimolecules as a function of internuclear distance (scaled internuclear distances ZR vary from 2 to 4 a.u.). In all the calculations, the quasimolecules are initially in the ground $1\sigma_g$ electronic state, and the laser electric field is linearly polarized parallel to the molecular axis. For H_2^+, the carrier wavelength is set to 248 nm ($\omega = 0.1837$ a.u.), and the peak intensity is 5×10^{14} W/cm^2. For the other quasimolecules, the scaled field parameters are used, as discussed above. The laser pulse shape is Gaussian, as described by equation (2.22). The total propagation time is 15 optical cycles (from -7.5 optical cycle to 7.5 optical cycle). The ionization probability P_i is calculated as:

$$P_i = 1 - P_b, \tag{2.32}$$

where P_b is the population of bound states at the end of the wave function evolution process in an external field. This calculation uses a Crank-Nicholson propagator

with 512 steps per optical cycle. It was found that with the matrix dimension of 8960 used in the calculations, the Crank–Nicholson method is more efficient than the split operator method, where 65536 time steps per optical cycle are necessary to obtain a result with the same accuracy.

When the scaled internuclear separation ZR varies from 2 to 4 a.u., the vertical ionization potential of the quasimolecule gradually decreases. At $ZR = 4$ a.u. to enter the continuum ($E>0$), the absorption of 5 photons is sufficient, so the threshold of 6-photon and 5-photon ionization is passed when the scaled internuclear distance ZR changes from 2 to 4 a.u. The position of the 6-photon ionization threshold varies from $ZR = 2.01$ a.u. for $Z = 1$ to $ZR = 2.25$ a.u. for $Z = 92$, while the corresponding ZR interval for the 5-photon threshold is 2.95 a.u. up to 3.40 a.u. The position of the 6-photon ionization threshold varies from $ZR = 2.01$ a.u. for $Z = 1$ to $ZR = 2.25$ a.u. for $Z = 92$, while the corresponding ZR interval for the 5-photon threshold is 2.95 a.u. up to 3.40 a.u. The probability of ionization can be expected to increase as the ionization potential and the minimum number of photons required for ionization decreases. The calculations carried out in this chapter of the dissertation, presented in figure 2.2 generally confirm this assumption: at $ZR = 2$ a.u. ionization probabilities do not exceed 0.02, and at $ZR = 4$ a.u. they are 20–35 times larger. Relativistic effects during multiphoton ionization can be assessed by the deviation of the ionization probabilities of different quasimolecules from each other at a fixed value of ZR: in the nonrelativistic case, they would be the same due to precise scaling. As expected, relativistic effects are less important for lighter nuclei. The ionization probabilities of H_2^+ and Ar_2^{35+} are very close to each other for ZR in the range from 2 to 3.25 a.u. The difference becomes somewhat larger for ZR between 3.5 and 4 a.u. For $Z = 54$, the deviation from the ionization probabilities of the H_2^+ molecule is more pronounced. It can be seen from Figure 2.3 that the results for $Z = 80$ and $Z = 92$ are very different from each other and from the results obtained for H_2^+. For some scaled internuclear distances ZR, the difference can exceed 100%, so relativistic effects are very important for one-electron quasimolecules with heavy, highly charged nuclei. One of the obvious effects is a relativistic shift in the energy level of the ground state towards a decrease in energy, which is greater the higher Z. Due to this effect, the ionization potential increases and quasimolecules with higher nuclear charge exhibit lower ionization probabilities, as can be seen in figure

2.2. It is important to note, that the relativistic nature of the electron dynamics in

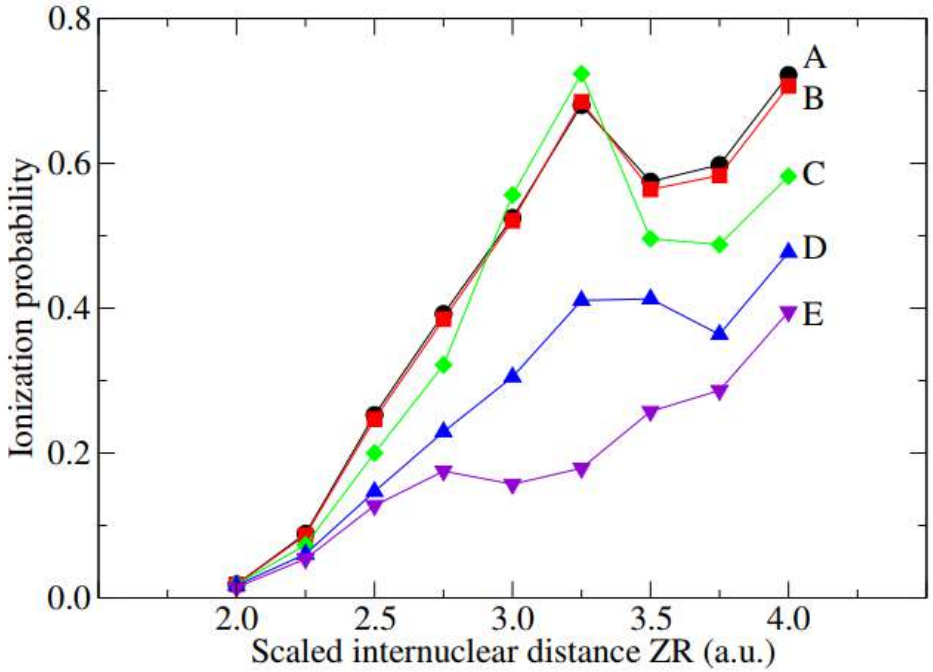

Figure 2.2: Probabilities of ionization of one-electron homonuclear quasimolecules with nuclear charge Z depending on the scaled internuclear distance ZR: (A), $Z = 1$; (B), $Z = 18$; (C), $Z = 54$; (D), $Z = 80$; (E), $Z = 92$. For H_2^+, the wavelength of the laser pulse is 248 nm, peak intensity 5×10^{14} W/cm^2, for other molecules the parameters are scaled according to (2.31).

these scaled quasimolecules is related not only to the interaction with the nuclei but also to the external field. The peak value of the classical electron momentum in the laser field can be estimated as F_0/ω. For H_2^+, this quantity is approximately equal to 0.65 a.u., that is very small compared to the speed of light. However, it scales as Z (from Eq. (2.31) it follows that the peak value of the speed is proportional to Z) for higher nuclear charges and reaches the value of 60 a.u. for $Z = 92$. This rough estimate indicates the relativistic nature of electron motion induced by an external electromagnetic field for quasimolecules with high nuclear charges and field parameters used in the calculations.

Another effect observed in figure 2.2 is related to the shift of the resonance frequency in the relativistic case. Homonuclear one-electron quasimolecules are the quantum systems where the ground $1\sigma_g$ and first excited $1\sigma_u$ states may become nearly degenerate at larger internuclear separations with a strong dipole coupling between them (charge resonance effect [97]). This effect is observed in the figure. 3 in the vicinity of $ZR = 3.25$ a.u. for quasimolecules with $Z = 1$, 18 and 54. This maximum (on the graph) of the ionization probability is due to the single-photon

resonance between the $1\sigma_g$ and $1\sigma_u$ states. This maximum is less pronounced for $Z = 80$ and does not exist for $Z = 92$. Since in the nonrelativistic case the position of the resonance must be the same for all scaled systems, the latter observation indicates that the relativistic effects may be responsible for the disappearance of the resonance in the heavier quasimolecules. In figure 2.3 shows the scaled energy difference between the $1\sigma_u$ and $1\sigma_g$ states as a function of the scaled internuclear distance ZR. For H_2^+, the one-photon resonance corresponds to $ZR = 3.18$ a.u., in good agreement with the position of the maximum in figure 2.2. For $Z = 18$, the shift of the resonance frequency is insignificant, so the position of the maximum does not visibly change. It is somewhat surprising that the maximum of the ionization probability is still at $ZR = 3.25$ a.u. for $Z = 54$, although the resonance frequency corresponds to $ZR = 3.03$ a.u. This can be explained as follows. At $ZR = 3.03$ a.u., ionization still requires absorption of 6 photons for $Z = 54$ (the 5-photon threshold corresponds to $ZR = 3.07$ a.u.), therefore the ionization probability for $Z = 54$ (see the data at $ZR = 3$ a.u. in figure 2.2) does not reach its maximum, although exceeds the probabilities for $Z = 1$ and $Z = 18$. The maximum is observed at $ZR = 3.25$ a.u. where the resonance is still nearby, but ionization takes place well above the 5-photon threshold. For $Z = 80$, the resonance position is at $ZR = 2.84$ a.u. while the 5-photon threshold is located at $ZR = 3.25$ a.u. The resonance lies well below the threshold in the 6-photon ionization region and does not significantly affect the ionization dynamics. A similar situation takes place for $Z = 92$, where the resonance and 5-photon threshold are located at $ZR = 2.71$ a.u. and $ZR = 3.40$ a.u. respectively. For this quasimolecule, however, one can see a weak resonance maximum at $ZR = 2.75$ a.u.

2.8 Nonlinear ionization beyond the dipole approximation

This section briefly discusses non-dipole effects in the ionization of quasimolecules by strong laser pulses, which can become significant at relatively high carrier frequencies. The same Gaussian laser pulse shape is used as described in equations (2.22). Beyond the dipole approximation, the carrier and envelope parts of the laser pulse contain a time dependence:

$$t \to (t - \frac{x}{c}) = \Phi/\omega, \tag{2.33}$$

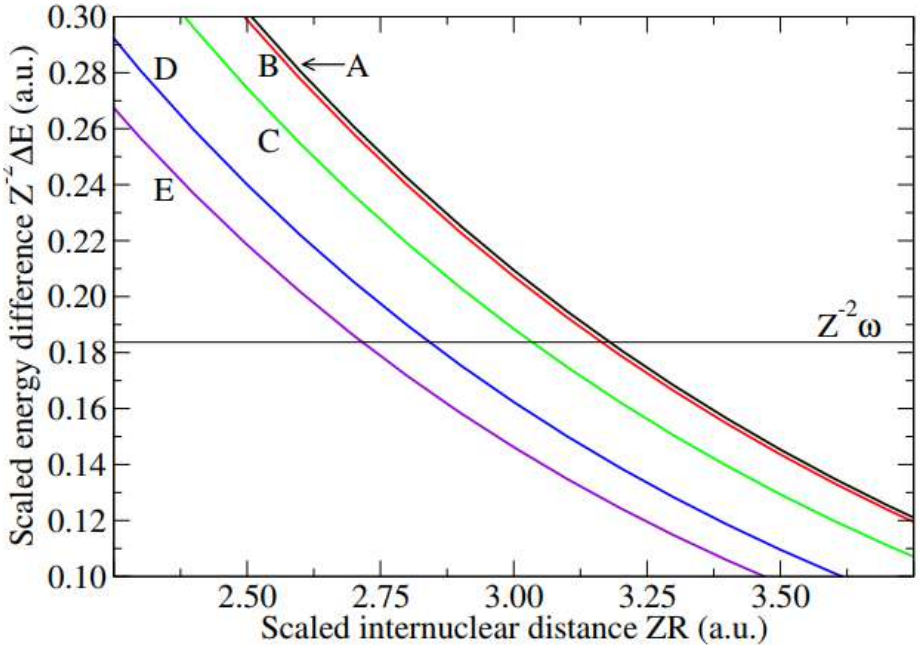

Figure 2.3: Scaled difference between the relativistic energies of the $1\sigma_u$ and $1\sigma_g$ states for several one-electron homonuclear quasimolecules with nuclear charge Z: (A), $Z = 1$; (B), $Z = 18$; (C), $Z = 54$; (D), $Z = 80$; (E), $Z = 92$. The horizontal line $Z^{-2}\omega$ corresponds to the scaled laser frequency

where Φ is the field phase. Upon the scaling transformation (2.31), the temporal part of this phase, ωt, remains invariant, while the spatial part $\frac{\omega x}{c}$ is multiplied by Z. Consequently, interaction with the electromagnetic field beyond the dipole approximation violates invariance with respect to the nonrelativistic scaling (2.31), even if the dynamics of the system is essentially nonrelativistic (that is, described by the time-dependent Schrödinger equation, which is exactly invariant under the transformation (2.31) in the dipole approximation). For the set of the scaled quasimolecules under consideration, the nondipole effects are more significant for the larger nuclear charge Z. In previous studies [57, 68] for numerical implementation it was necessary to separate the spatial and temporal dependence in the vector potential using the Fourier expansion in Φ or the Taylor series expansion in powers of x. However, as the field strength increases, this approach may require the inclusion of more and more expansion terms to achieve convergence [54]. In the method used in this work, this is not required for the vector potential, and it can be used without any expansions. The x coordinate, expressed in prolate spheroidal coordinates, depends on

the azimuthal angle ϕ:

$$x = a\sqrt{(\xi^2 - 1)(1 - \eta^2)}\cos\phi. \tag{2.34}$$

This angle is discretized on a uniform grid in the interval $[0, 2\pi]$. The number of grid nodes ϕ is equal to the number of angular momentum projections remaining in the wave function (2.14). Thus, the accuracy of the vector potential representation is controlled by the number of angular momentum projections used. If the non-dipole corrections are not very large, a few components of the wave function are usually sufficient for convergence (2.14).

As an example of non-dipole effects in quasimolecules, calculations were carried out for H_2^+ and for Ar_2^{35+} at a laser field frequency of $\omega = 3.5$ a.u., recently used in relativistic calculations hydrogen atom [57, 68] and peak value $F_0 = 40$ a.u. and internuclear distance $R = 2$ a.u. For Ar_2^{35+} the parameters were scaled accordingly. This calculation used a split operator method with 65536 time steps in an optical cycle with 15 optical cycles (from -7.5 to 7.5 optical cycles). Figure 2.4 demonstrates the population of bound states P_b(t) in the case of the dipole approximation and in the case when it goes beyond it. Here it is interesting to see how the difference between the results of the dipole approximation (DA) and the full interaction with the included projections $|m| \leq 1$ (F1) or $|m| \leq 3$ (F3) increases with time. The results of calculations in the dipole approximation for H_2^+ and Ar_2^{35+} differ from each other much more strongly than in the case of multiphoton ionization, as can be seen from figure 2.4, and the probability of ionization Ar_2^{35+} is greater than the ionization probability of H_2^+, in contrast to the trend observed in figure 2.2. The thing is that, for the chosen field parameters, the relativistic effects caused by the external field are much stronger for Ar_2^{35+}. For this quasimolecule, the peak velocity of a classical electron oscillating in a field exceeds the speed of light, indicating an ultrarelativistic regime. For H_2^+ this speed is about $v = 0.08c$.

For H_2^+ the non-dipole effects are quite small, as can be seen in figure 2.4. The difference between the results for the full interaction with the (F1) and (F3) projections included is not visible even at the magnification shown in the inset. It can be concluded that calculations with complete interaction in this case converge well already at the (F1) level. If for the first 3 optical cycles the discrepancy between (DA) on the one hand and (F1), (F3) on the other is still insignificant, then at

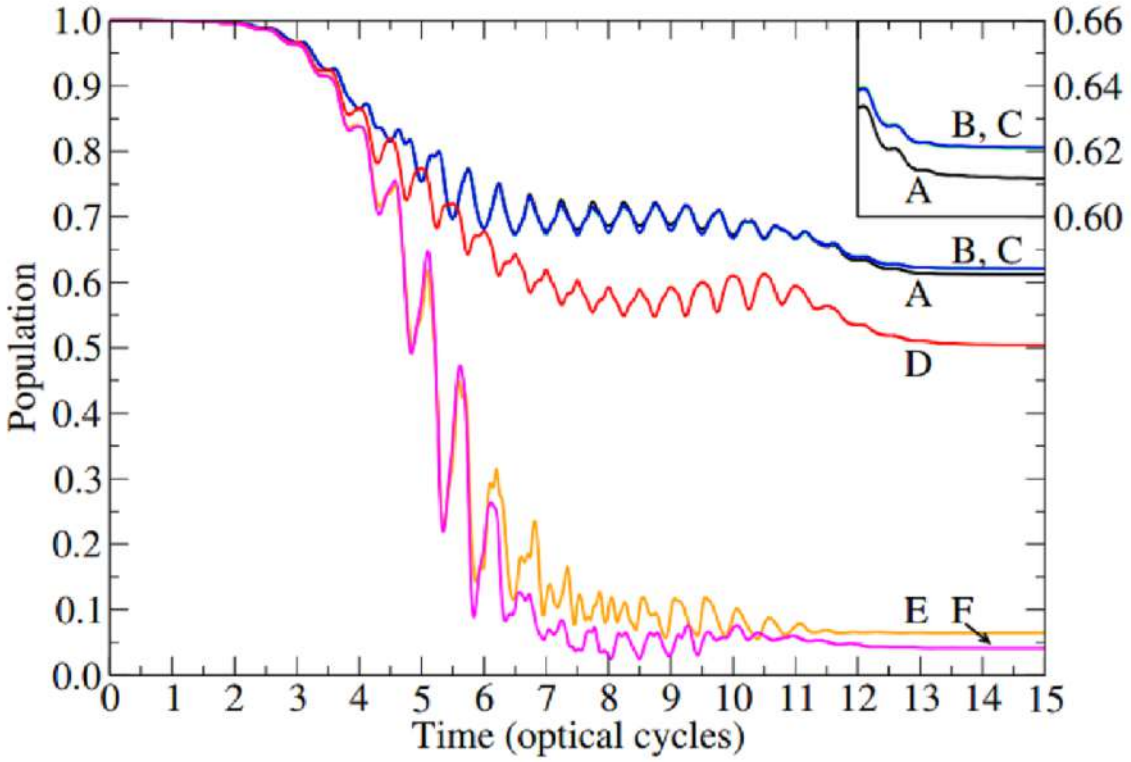

Figure 2.4: Time-dependent population of bound states for H_2^+ and Ar_2^{35+}. A, B, C – (DA), (F1), and (F3) data for H_2^+; D, E, F – (DA), (F1) and (F3) data for Ar_2^{35+} respectively (see text for explanation). The inset shows the H_2^+ data zoomed vertically from a population value of 0.60 to 0.66 for the last 3 optical cycles. For H_2^+ the carrier frequency is 3.5 a.u. and peak field strength is 40 a.u.; scaled field parameters are used for Ar_2^{35+}.

later times it quickly increases, leading to almost complete ionization by the middle of the laser pulse if the interaction is described outside the dipole approximation. The difference between (F1) and (F3) is much smaller and increases as the field becomes even stronger, starting from the fifth optical cycle. In the second half of the pulse, the picture does not change qualitatively. The probability of ionization reaches 93.5 % (F1) or 96 % (F3) when using the full interaction, and in the dipole approximation does not exceed 50 %. Strong non-dipole effects in Ar_2^{35+} contribute to the ionization of this quasimolecule: the ionization probability calculated outside the dipole approximation is significantly greater than in the dipole approximation. On the contrary, for the H_2^+, weak non-dipole effects lead to relative stabilization. The ionization probabilities (F1) and (F3) are only slightly less than the (DA) result for the molecule H_2^+. The contrast between the results for scaled H_2^+ and Ar_2^{35+} is easy to explain. In the case of H_2^+, the vector potential of the laser field, due to its spatial dependence, changes sign at a distance of about 120 a.u., which significantly exceeds the size of the molecule estimated from the internuclear distance R = 2 a.u. For Ar_2^{35+}, with the same scaled internuclear distance ZR = 2 a.u., the vector potential changes sign at a scaled distance of about 7 a.u., comparable to the size of the electron wave packet. The pulse envelope in space, relative to the scale coordinate Zx, is also 18 times narrower than in the case of H_2^+. This means that the external field is significantly inhomogeneous even for an electron in the initial ground state. Different parts of the electron wave packet then experience opposing forces and move out of phase, promoting irreversible transitions to higher energy bound and continuum states.

2.9 Chapter 2 Summary

In this chapter of the dissertation, a method for calculating the interaction of single-electron homonuclear quasimolecules for the relativistic Dirac equation in a high-intensity external field is developed. It was found that when solving the eigenvalue problem for the nonstationary Dirac equation (as well as for the Schrödineger equation) using this method, spurious states do not arise, at least among low-lying bound states, so no additional effort is required to remove them. An analysis of relativistic and non-dipole effects is carried out for various quasimolecules and external

field parameters subject to nuclear charge scaling. The deviation of the results for the scaled relativistic calculation from the scaled non-relativistic calculation indicates the role of relativistic dynamics and the importance of describing the interaction with the external field beyond the dipole approximation. One of the well-known relativistic effects of multiphoton ionization, common to atomic and molecular ions, is the decrease in the probability of ionization with increasing nuclear charge due to the relativistic deepening of the energy level of the ground state. Quasimolecules have a large number of degrees of freedom compared to atoms and atomic ions, which opens up new opportunities for research. For example, by changing the internuclear distance, the transition frequency between two specific electronic states can be tuned to resonate with the carrier frequency of the laser pulse. At such internuclear distances, ionization can be significantly enhanced.

Unlike relativistic effects, which can be significant even at low scaled frequencies and moderate peak intensities, non-dipole effects become more noticeable at high scaled frequencies. For quasimolecules, an increase in non-dipole corrections to the probability of ionization is observed with increasing nuclear charge. Calculations at a carrier frequency of 3.5 a.u. and peak field strength 40 a.u. show that the difference between the dipole approximation and the results of the full interaction for H_2^+ is still insignificant, while for Ar_2^{35+}, the dipole approximation leads to incorrect results. The same decay can be expected for other quasimolecules with higher nuclear charges.

Chapter 3. Influence of the phase of the electromagnetic field on the processes of charge transfer and ionization in laser-assisted collisions of protons with hydrogen atoms

This chapter of the dissertation examines the influence of the phase and intensity of a laser field, linearly polarized in the plane of collision of a proton with a hydrogen atom, on charge transfer and ionization for the symmetric $H–H^+$ system. The collision dynamics are studied using the unsteady Schrödinger equation, which is initially written in the center of mass frame. Then a transition is made to a non-inertial rotating reference frame, which leads to the appearance of additional terms in the Hamiltonian that take rotation into account. The velocity of the incident proton is chosen to be quite low ($v_0 = 0.1$ a.u., which corresponds to an energy of 0.25 keV). The main goal was to obtain the dependence of the charge transfer probability $P_{\text{ct}}(b)$ (where b is the impact parameter), the ionization probability $P_{\text{i}}(b)$, as well as electron cross sections capturing σ_{ct} for various field parameters. Calculations were carried out at field strengths of 1×10^{12} W/cm^2 and 1×10^{13} W/cm^2 for a frequency of 0.01 a.u. and 5×10^{14} W/cm^2 for frequency 2 a.u. At an intensity of 1×10^{12} W/cm^2 the probability of ionization is small (does not exceed a few percent), and at an intensity of 1×10^{13} W/cm^2 significant ionization is expected for small impact parameters at low frequency 0.01 a.u. Regarding the phase of the external field, one can expect that the dynamics of charge transfer significantly depends on the phase in the low-frequency case and, conversely, at high frequencies the field phase does not play a significant role. The results obtained are compared with the case of a collision in the absence of a field.

3.1 Taking into account the motion of an incident proton in the Schrödinger equation during a collision

Let us place the center of the fixed coordinate system in the center of mass of the two nuclei. In this coordinate system, the time-dependent Schrödinger equation for the electron interacting with the nuclei and external field has the conventional form:

$$i\frac{\partial}{\partial t}\Psi(\mathbf{r},t) = [H_0 + V(\mathbf{r},t)]\Psi(\mathbf{r},t), \tag{3.1}$$

where H_0 is the unperturbed Hamiltonian of the quasimolecule including the kinetic energy operator and the interaction potential $U(\mathbf{r})$ between the electron and the nuclei:

$$H_0 = -\frac{1}{2}\nabla^2 + U(\mathbf{r}), \tag{3.2}$$

$$U(\mathbf{r}) = -\frac{Z_A}{|\mathbf{r}-\mathbf{R}_A|} - \frac{Z_B}{|\mathbf{r}-\mathbf{R}_B|}, \tag{3.3}$$

where Z_A, Z_B and $\mathbf{R}_A$, $\mathbf{R}_B$ are the nuclei charges and radius-vectors, respectively. Note that $U(\mathrm{r})$ and H_0 depend on time through the radius-vectors of the moving nuclei. The operator $V(\mathrm{r},t)$ describes the interaction of the electron with the external electromagnetic field. In the charge exchange problem, the electromagnetic field is considered in the dipole approximation in the velocity gauge, so the interaction operator takes the form:

$$V(\mathbf{r},t) = -i(\mathbf{A}\cdot\nabla) + \frac{1}{2}A^2, \tag{3.4}$$

where the vector potential $\mathbf{A}(t)$ depends on time but does not depend on the coordinates.

The motion of nuclei is described within the framework of classical mechanics. When considering an electron in the Coulomb field of nuclei, the trajectories of the incident particle and the target are hyperbolic. However, in the case of a collision H–H^+, the target is initially neutral. In this case, you can use the approximation when the incident particle and the target move with constant speeds $-\frac{1}{2}\mathbf{v}_0$ and $\frac{1}{2}\mathbf{v}_0$ respectively along rectilinear trajectories. The collision plane is perpendicular to the angular momentum vector of the incident particle and is formed by the z_0 and x_0 axes (figure 3.1). When the nuclei move (target A and incident particle B in figure 3.1), the molecular axis (denoted as z) rotates in the $z_0 - x_0$ plane. In this

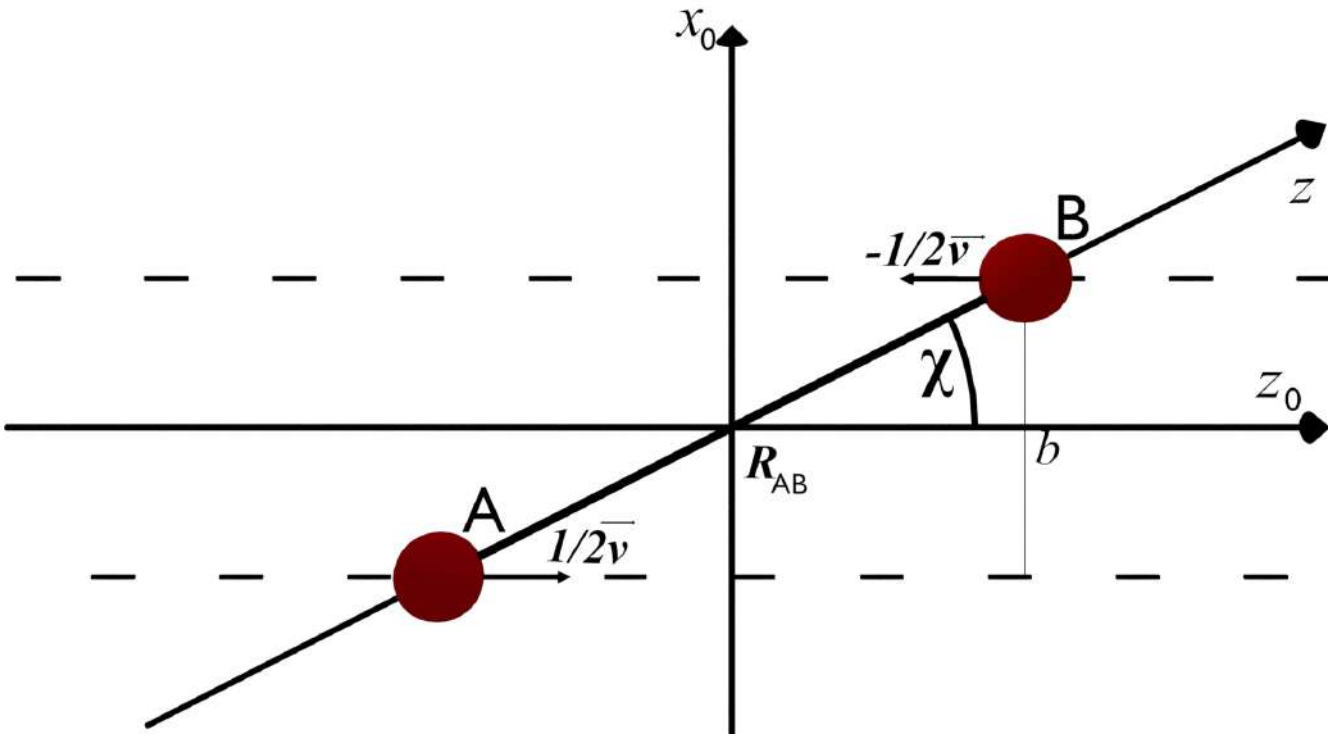

Figure 3.1: Collision of incident particle B (proton) with target A (hydrogen atom) in the center of mass system. The stationary axes z_0 and x_0 and the rotating molecular axis z are shown. Other notations: b is the impact parameter, R_{AB} is the internuclear distance, χ is the angle between z and z_0.

chapter, the motion of nuclei was considered on a symmetric time interval $[-t_0, t_0]$, from the initial internuclear distance $R_{AB}(t_0) = 40$ a.u. until the moment when the internuclear distance again becomes equal to 40 a.u. Initial internuclear distance 40 a.u. is quite large, so the interaction of an electron localized on the target with the incident particle is negligible. As was verified in calculations, an increase in the initial internuclear distance does not lead to a change in the charge transfer pattern, but only increases the probability of ionization due to an increase in the time of interaction of the system with an external electromagnetic field.

The position of the incident proton is determined by the internuclear distance R_{AB} and the value of the angle $\chi(t)$ between the axes z and z_0 at each moment of time. The angular velocity $\omega(t) = \dot{\chi}(t)$ is calculated as follows:

$$\omega(t) = \frac{v_0 b}{b^2 + v_0^2 t^2}, \tag{3.5}$$

where b is the impact parameter. The initial value of the internuclear distance $R_{AB}(t_0)$, impact parameter b, proton velocity v_0, and time t_0 are related to each

other as follows:

$$R_{AB}^2(t_0) = (v_0 t_0)^2 + b^2, \tag{3.6}$$

It is convenient to solve the nonstationary Schrödinger equation for a diatomic quasimolecule in a molecular reference frame, where the internuclear axis is chosen as the z axis, the x axis lies in the collision plane, and the y axis is perpendicular to the collision plane. However, the molecular frame of reference rotates around the y axis, so it is non-inertial. This circumstance leads to the appearance of an additional term in the Hamiltonian for the time-dependent Schrödinger equation (3.1) in the molecular frame of reference [98]. In the molecular coordinate system, the transformed nonstationary Hamiltonian H_{mcs} is expressed as follows:

$$H_{\text{mcs}} = H_0 - \omega(t) L_y + V(\mathbf{r}, t), \tag{3.7}$$

where L_y is the operator of the angular momentum projection on the y axis (this axis is fixed in both the molecular and inertial frames). In the molecular system, prolate spheroidal coordinates are again used, since these coordinates fully take into account the two-center nature of the diatomic quasimolecular system. The parameter of the prolate spheroidal coordinate system $a(t)$ specifies half of the internuclear distance: $R_{AB}(t) = 2a(t)$. Before the collision, the electron is localized on the target, therefore the wave function of the initial state of the electron is constructed as a linear combination of the two lowest-energy molecular orbitals of the Hamiltonian H_0 at $t = -t_0$, which are $1\sigma_g$ and $1\sigma_u$ solutions of the stationary Schrödinger equation:

$$H_0(-t_0)\Psi_i(\mathbf{r}) = E_i \Psi_i(\mathbf{r}). \tag{3.8}$$

Since the initial internuclear distance (40 a.u.) is very large for the H–H^+ system, the lowest $1\sigma_g$ and $1\sigma_u$ states are nearly degenerate. A superposition of these states gives an electron density distribution localized around one of the nuclei, which corresponds to the initial conditions of our problem. The equations (3.1) and (3.8) are solved with the help of the generalized pseudospectral (GPS) method. Since the parameter $a(t)$ depends on time, it turns out to be possible either to use a moving grid when discretizing coordinates in the generalized pseudospectral method, or to perform a scaling transformation of the wave function before solving the equation (3.1), so the distance between the centers of the spheroidal coordinate system becomes fixed. In this work, the second approach is used. The wave function $\Psi(\mathbf{r}, t)$

is represented as follows:

$$\Psi(\mathbf{r},t) = [a(t)]^{-3/2}\tilde{\Psi}(\tilde{\mathbf{r}},t), \tag{3.9}$$

$$\mathbf{r} = a(t)\tilde{\mathbf{r}}. \tag{3.10}$$

The scale transformation (3.9) preserves the norm of the wave function:

$$\int d^3r|\Psi(\mathbf{r},t)|^2 = \int d^3\tilde{r}|\tilde{\Psi}(\tilde{\mathbf{r}},t)|^2. \tag{3.11}$$

According to the definition (3.10), the distance between the centers of the spheroidal coordinate system for the scaled coordinates $\tilde{\mathbf{r}}$ is chosen to be 2 a.u. at all times. Once the wave function in the form (3.9) is substituted in the equation (3.1), another term is added to the Hamiltonian. The new Hamiltonian $\tilde{H}_{\rm mcs}$ and the time-dependent equation for the wave function $\tilde{\Psi}(\tilde{\mathbf{r}},t)$ take the following form:

$$\begin{aligned}\tilde{H}_{\rm mcs} = &-\frac{1}{2a^2(t)}\nabla^2_{\tilde{\mathbf{r}}} - \frac{Z_A}{a(t)|\tilde{\mathbf{r}}+\mathbf{e}_z|} \\ &- \frac{Z_B}{a(t)|\tilde{\mathbf{r}}-\mathbf{e}_z|} - \omega(t)L_y + V(a(t)\tilde{\mathbf{r}},t) \\ &+ i\frac{\dot{a}(t)}{a(t)}\left(\frac{3}{2}+\tilde{\mathbf{r}}\cdot\frac{\partial}{\partial\tilde{\mathbf{r}}}\right),\end{aligned} \tag{3.12}$$

$$i\frac{\partial}{\partial t}\tilde{\Psi}(\tilde{\mathbf{r}},t) = \tilde{H}_{\rm mcs}(\tilde{\mathbf{r}},t)\tilde{\Psi}(\tilde{\mathbf{r}},t). \tag{3.13}$$

The first three terms on the right side (3.12) represent the kinetic energy operator and the U interaction potential of the electron with nuclei. The last term in (3.12) arises from scaling by the parameter $a(t)$, where:

$$\tilde{\mathbf{r}}\cdot\frac{\partial}{\partial\tilde{\mathbf{r}}} = \frac{1}{\xi^2-\eta^2}\left(\xi(\xi^2-1)\frac{\partial}{\partial\xi} + \eta(1-\eta^2)\frac{\partial}{\partial\eta}\right). \tag{3.14}$$

Finally, the angular momentum projection operator L_y takes the form:

$$\begin{aligned}L_y = -i\frac{\sqrt{(\xi^2-1)(1-\eta^2)}\cos\varphi}{\xi^2-\eta^2}\left(\eta\frac{\partial}{\partial\xi} - \xi\frac{\partial}{\partial\eta}\right) \\ +i\frac{\xi\eta\sin\varphi}{\sqrt{(\xi^2-1)(1-\eta^2)}}\frac{\partial}{\partial\varphi}.\end{aligned} \tag{3.15}$$

The equation is solved inside a spatial domain with linear size R_b. The value of R_b is chosen large enough so that all physically significant processes occur at distances

smaller than R_b. Calculations were carried out at $R_b = 80$ a.u. for the original (unscaled) coordinates $\mathbf{r}$, this is acceptable for the external field parameters used. For scaled coordinates $\tilde{\mathbf{r}}$, the values of $\tilde{R}_b$ can be found using the transformation formula (3.10) for the smallest value of $a(t)$ at the time of the collision.

In this chapter of the dissertation, it is assumed that the external electromagnetic field is linearly polarized along a fixed z_0 axis. At an arbitrary moment of time t, the polarization vector is directed at an angle $\chi(t)$ to the molecular axis z, as shown in figure 3.1. The vector potential $\mathbf{A}(t)$ is expressed as follows:

$$\mathbf{A}(t) = -\frac{F_0}{\omega_0}\cos(\omega_0 t + \phi)W(t)\mathbf{e}_{z_0}, \tag{3.16}$$

where F_0 is the peak field strength, ω_0 is the carrier frequency of the electromagnetic wave, ϕ is the field phase at $t = 0$, that is, the value at the closest approach between the nucleus and the target. The multiplier $W(t)$ is the field envelope that is used to smoothly turn the field on at time $-t_0$ and turn it off at time t_0. The function $W(t)$ has the form:

$$\begin{aligned} &W(t) = \cos^2[4\pi(\frac{t}{t_0} + 0.875)] \ (-t_0 \le t < -0.875t_0), \\ &W(t) = 1 \quad (-0.875t_0 \le t \le 0.875t_0), \\ &W(t) = \cos^2[4\pi(\frac{t}{t_0} - 0.875)] \ (0.875t_0 < t \le t_0). \end{aligned} \tag{3.17}$$

Numerical solution methods (3.13) were presented in Chapter 1 (Here, the Crank-Nicholson method is used to describe the time evolution of the wave function). In this chapter, the number of time steps in the Crank-Nicholson method was equal to $N = 2000$ for calculations with an impact parameter $b > 1.5$ a.u. and the number of time steps $N = 3000$ for calculations with an impact parameter $b \le 1.5$ a.u. To prevent unphysical reflections of the electron wave packet from the boundaries of the spatial domain, the wave function at each time step is multiplied by the mask function $f(\xi)$, which smoothly tends to zero inside the layer between R_a and R_b by the boundary of the spatial domain:

$$\begin{aligned} &f(\xi) = \cos\left[\frac{\pi(a\xi - R_a)}{2(R_b - R_a)}\right]^{1/4} \quad (R_a \le a\xi \le R_b), \\ &f(\xi) = 1 \quad (a \le a\xi \le R_a). \end{aligned} \tag{3.18}$$

In this chapter, calculations were carried out with the boundary layer parameter R_a=65 a.u. The following grid sizes were used in the calculations: the number of collocation points along the ξ coordinate is 80, at the η coordinate—12, at the φ coordinate 7 for the impact parameter $b > 1.5$ a.u. For smaller impact parameters, values of 120 points along ξ, 16 along coordinate η and 7 along coordinate φ were used. Increasing the number of points to 180 points along ξ, up to 24 points along the η coordinate and 9 points along the φ coordinate leads to a deviation of the result by less than 1%.

3.2 Probability of charge transfer

Following the time evolution of the wave function, the electron at the time t_0, when the field is turned off, can remain in a bound state on the target, be in a bound state on the incident particle, and also go into an unbound state with $E > 0$. In the last case, the parts of the wave packet that reach the boundary layer during the propagation will be absorbed, leading to a decrease in the norm of the wave function. The squared norm of the wave function at the time t_0 can be represented as follows:

$$\int \Psi^*(\tilde{\mathbf{r}}, t_0)\Psi(\tilde{\mathbf{r}}, t_0)d^3\tilde{r} = P_\mathrm{c} + P_\mathrm{b}, \tag{3.19}$$

where P_c is the population of unbound states with positive energies whose wave packet has not yet reached the absorbing layer by the time t_0 and P_b is the population of bound states. The population P_c is evaluated by projecting the wave function at t_0 onto the quasimolecular continuum. As the calculations reveal, this quantity is always negligibly small, that means, almost all free electrons reach the absorber by the time t_0 because the propagation time is long enough due to slow nuclear motion. Thus the ionization of the system is determined by the following expression with a good accuracy:

$$P_\mathrm{i} = 1 - \int \Psi^*(\tilde{\mathbf{r}}, t_0)\Psi(\tilde{\mathbf{r}}, t_0)d^3\tilde{r}. \tag{3.20}$$

Probability of the electron capture by the incident particle can be represented as an integral of the squared absolute value of the wave function over the half-space containing the incident particle nucleus. In prolate spheroidal coordinates, this

integral is written as follows:

$$P_{\text{ct}} = \int_1^{\infty} d\xi \int_0^1 d\eta \int_0^{2\pi} d\varphi \; (\xi^2 - \eta^2)|\Psi(\tilde{\mathbf{r}}, t_0)|^2. \tag{3.21}$$

If integration over the coordinate η in the formula (3.21) is carried out in the range from -1 to 0, then the probability of finding an electron on the target will be obtained. In the case of significant population P_{c} of unbound states inside the spatial domain, it is necessary to project the wave function $\Psi(\tilde{\mathbf{r}}, t_0)$ onto the subspace of bound states ($E < 0$) of the Hamiltonian at time t_0 before calculating the charge transfer probability.

3.3 Main results of Chapter 3

The charge transfer probability during a collision H–H^+ is determined by such parameters as the speed of the incident particle, the impact parameter, the frequency and intensity of the laser field, as well as the phase of the field at the moment of closest approach of the colliding particles. In the calculations of this chapter, the collision energy is equal to 0.25 keV, that is, the velocity of the incident particle v_0 is equal to 0.1 a.u. The impact parameter b ranges from 0.125 a.u. up to 8.5 a.u. with a step $\Delta b = 0.125$ a.u., the phase ϕ takes values of 0°, 90°, 180° and 270° degrees. Calculations were carried out for three different combinations of laser field frequency and intensity. In the first series of calculations, the influence of low-intensity (1×10^{12} W/cm^2) and low-frequency ($\omega = 0.01$ a.u.) fields on the probability of charge transfer for various field phases at the moment of the smallest distance between colliding particles. Since the external field is weak, ionization is relatively small. In the second series of calculations, the field strength is much higher (1×10^{13} W/cm^2), which makes it possible to study the process of charge transfer at the same low frequency $\omega = 0.01$ a.u. under conditions of significant ionization of the H–H^+ system. For frequency $\omega = 0.01$ a.u. flight time of an incident particle between the initial and final positions at an internuclear distance of 40 a.u. comparable to the time of one optical field cycle, so that the phase of the external field changes slightly when the incident particle and the target are in close proximity. In the third series of calculations, a high-frequency ($\omega = 2$ a.u.) external

field is used to study the effect of phase on charge transfer under conditions of a rapidly oscillating field. The field strength in this series of calculations is also high (5×10^{14} W/cm^2), although the ionization turns out to be small.

Figure 3.3 shows the dependence of the charge transfer probability P_{ct} on the impact parameter for the laser field with the peak intensity 1×10^{12} W/cm^2 and frequency $\omega = 0.01$ a.u. Presented are the results for different phases ϕ as well as the probability of the charge transfer without the external field. Evidently, the phase ϕ has a significant effect on the probability of electron capture by the incident particle in the region of small impact parameters b. As one can see, at large impact parameters ($b > 1.75$ a.u.), the charge transfer probability remains almost unchanged if the field changes the sign (that is, the phase of the field is changed by π): a difference between the results for $\phi = 0°$ and $\phi = 180°$ is less than 1%, the same is true for the pair of phases $\phi = 90°$ and $\phi = 270°$. In the range of small impact parameters, $b \leq 1.75$, a divergence of the charge transfer probabilities within the same pair of phases becomes noticeable. The results differ substantially between different phase pairs: the difference can reach up to $\approx 30\%$ (for example, at the impact parameter $b = 0.5$ a.u., the charge transfer probability for the field with the phase $\phi = 180°$ is approximately 90% while for the field with phase $\phi = 90°$ it is about 63%).

Figure 3.2, panel a, shows the dependence of the ionization probability P_{i} on the impact parameter b for different phases ϕ. The field parameters and incident particle speed are the same as for the data in figure 3.3. In Figure 3.2 there is no ionization probability for the case without a field, since in this case for all impact parameters the ionization probability $P_{\text{i}}(b)$ is much less than 1%. It turns out that for all impact parameters, the probability of ionization for the $\phi = 180°$ phase is the greatest, and the probability of ionization for the $\phi = 270°$ phase is the smallest. As can be seen, ionization increases significantly in the region of small impact parameters. This can be explained as follows. In close collisions, excited bound states become significantly populated. Such states are then easily ionized by a low-frequency external field via a tunnel or over-barrier mechanism.

Let us proceed with the analysis of the dependence of the charge transfer and ionization probabilities, P_{ct} and P_{i}, on the phase ϕ. Consider the population of the half-space containing the incident particle nucleus calculated according to (3.21) but at an arbitrary time moment. In the case of low ionization, one may think of this

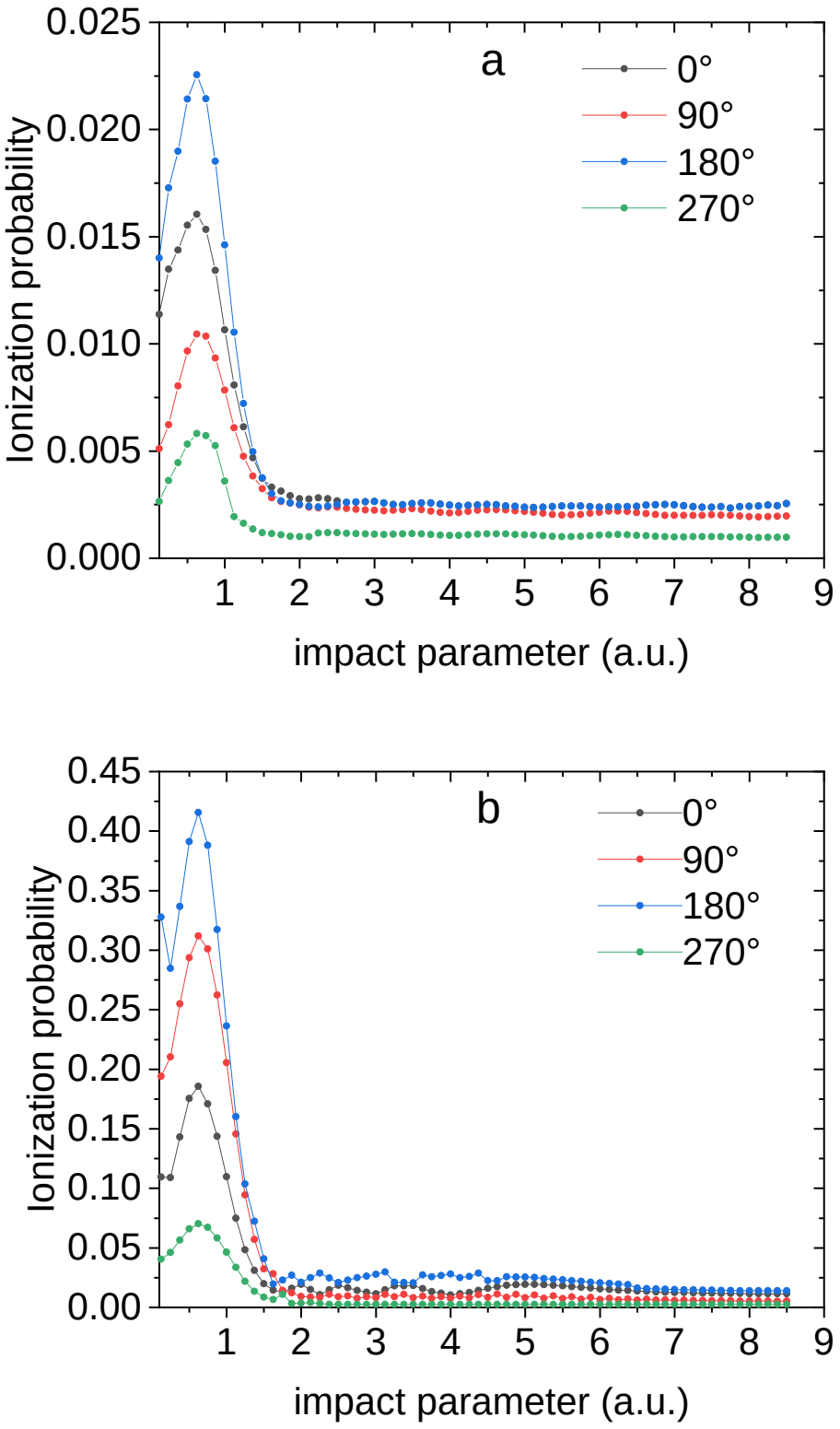

Figure 3.2: Probability of ionization P_{i} of the H–H$^+$ system depending on the impact parameter for different phases ϕ at a collision velocity v_0=0.1 a.u. and frequency ω=0.01 a.u. for two peak field intensities: (a), intensity 1×10^{12} W/cm^2; (b), intensity 1×10^{13} W/cm^2.

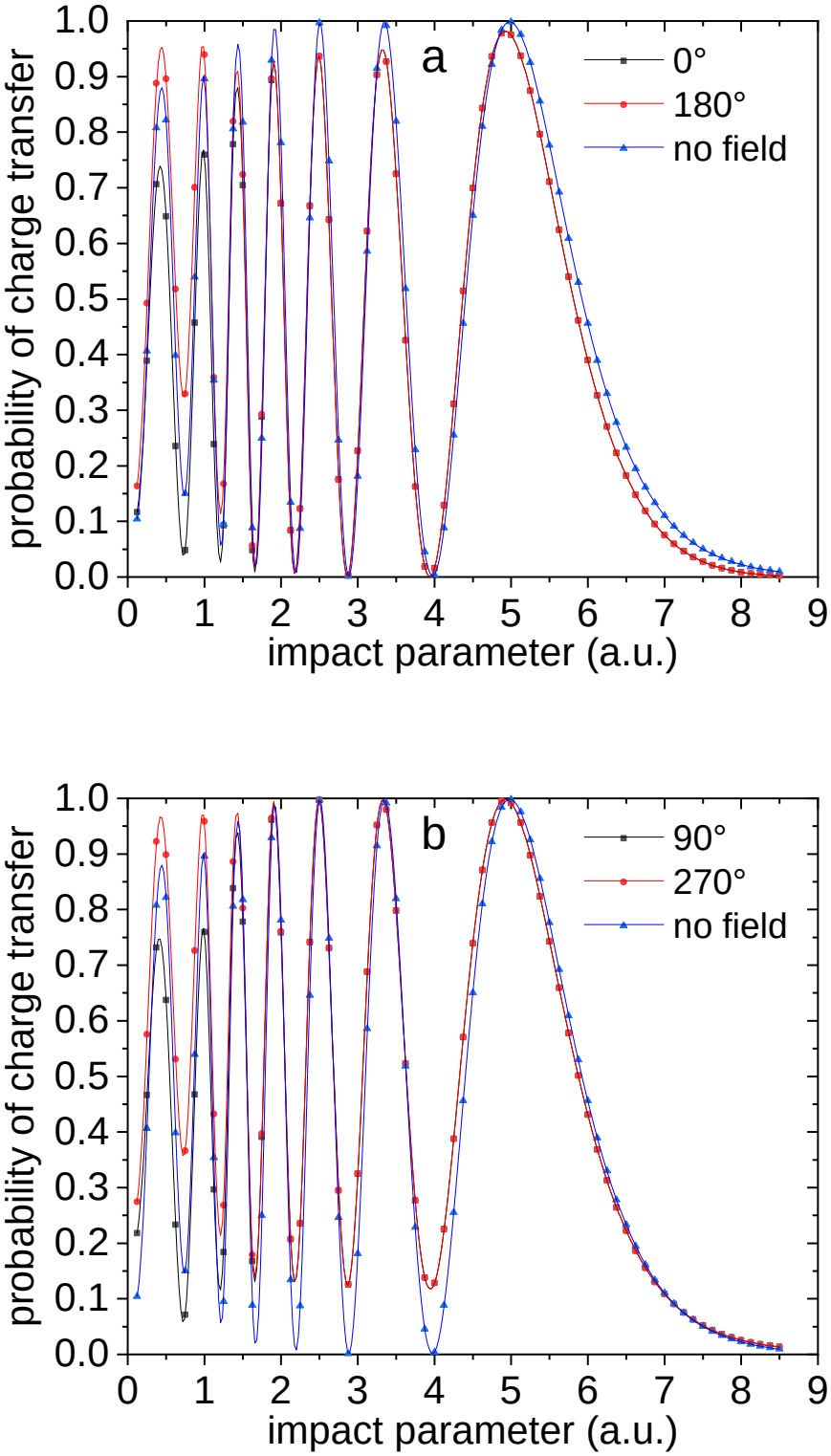

Figure 3.3: Probability of charge transfer P_{ct} depending on the impact parameter when a proton collides with a hydrogen atom in a linearly polarized external field with a frequency $\omega_0 = 0.01$ a.u. and intensity 1×10^{12} W/cm^2, for different field phases: (a), $\phi = 0°$ (black line) and $\phi = 180°$ (red line); (b), $\phi = 90°$ (black line) and $\phi = 270°$ (red line). The blue lines in both panels show P_{ct} without the external field.

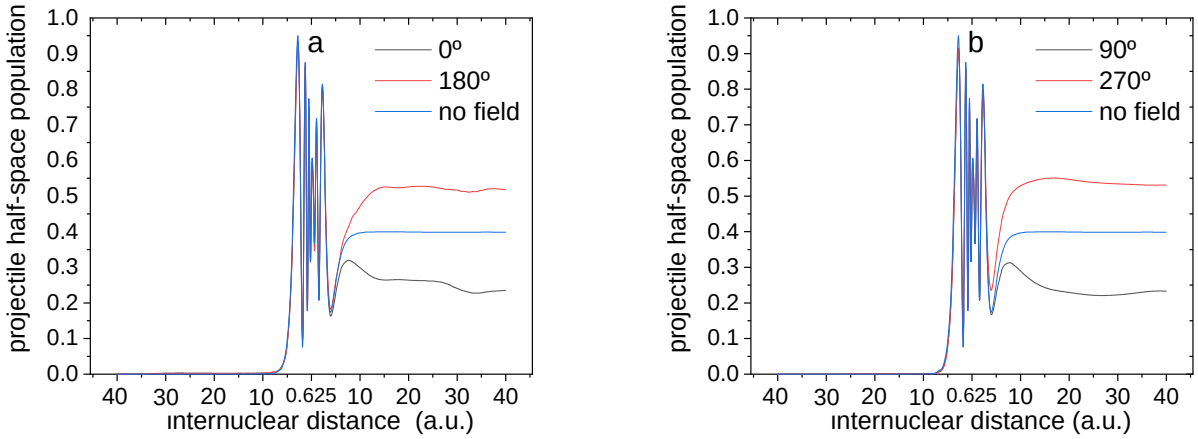

Figure 3.4: The electron population of the incident particle (projectile) in the H–H^+ collision as a function of the internuclear distance R_{AB} for the laser peak intensity 1×10^{12} W/cm^2, collision velocity v_0=0.1 a.u., field frequency $\omega_0 = 0.01$ a.u., and impact parameter $b = 0.625$ a.u.: (a), for the phases $\phi = 0°$, 180° and the case without the field; (b), for the phases $\phi = 90°$, 270° and the case without the field. When approaching, the internuclear distance decreases from 40 a.u. to 0.625 a.u. (left-hand side of the internuclear distance axis). As the nuclei move apart from each other, the internuclear distance increases from 0.625 a.u. to 40 a.u. (right-hand side of the internuclear distance axis).

quantity as the instantaneous charge transfer probability at a given time (or at a given internuclear distance). Figure 3.4 shows the dependence of such population on the internuclear distance R_{AB} for the impact parameter $b = 0.625$ a.u., at which the highest probability of ionization is observed for all values of phase ϕ on Figure 3.2. The following figure 3.5 shows the force F_{z_0} acting on an electron from an external field at a strength of 1×10^{12} W/cm^2. Shown is the dependence of this force on the internuclear distance, for various phases ϕ and the same value of the impact parameter $b = 0.625$ a.u. As one can see in figure 3.4, rapid oscillations of the instantaneous charge transfer probability occur when the incident particle and the target are in close proximity to each other. These oscillations start when the incident particle approaches the target at the internuclear distance $R_{AB} \approx 5$ a.u. and end approximately at the same internuclear distance when the incident particle flies away. Just before the incident particle enters this region around the target, the instantaneous charge transfer probability is close to zero, regardless of the presence of the field and its phase. Therefore, the resulting charge transfer probability is determined by the influence on the electron from nuclear Coulomb forces and the

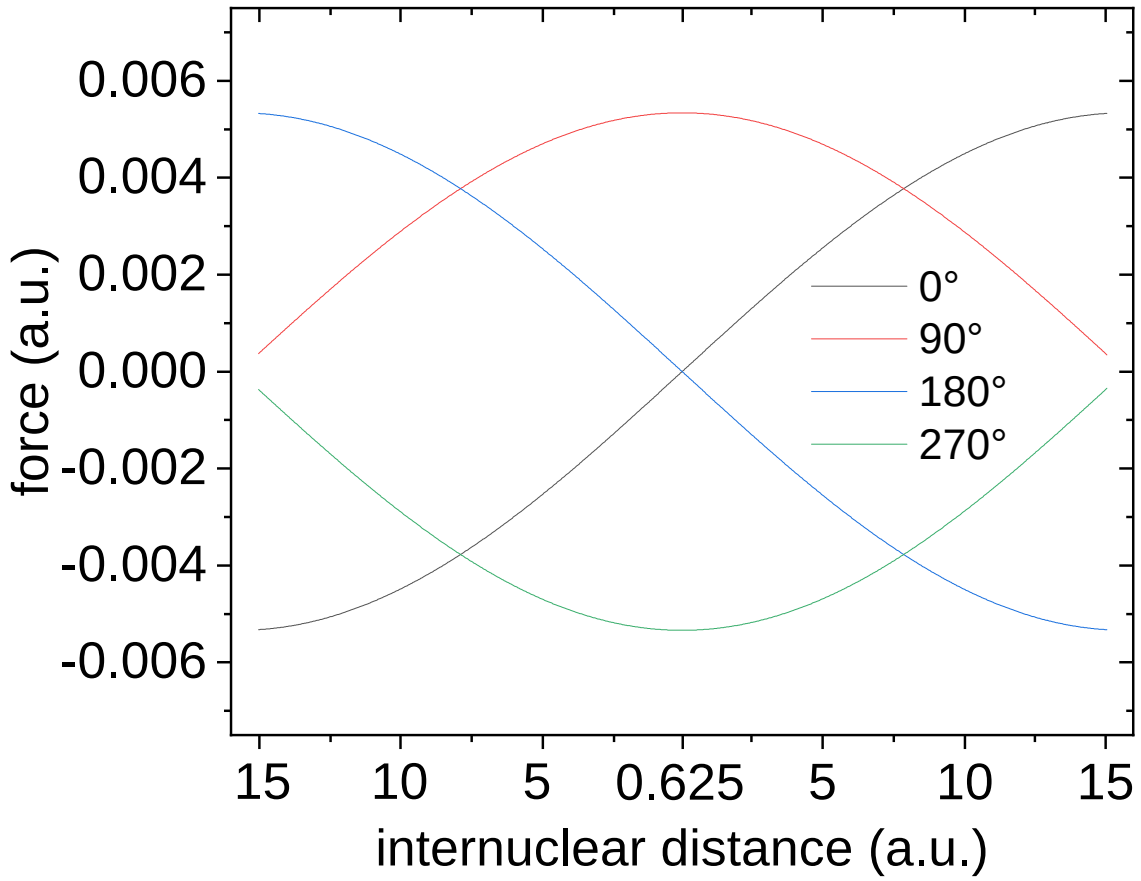

Figure 3.5: The force F_{z_0} experienced by the electron from the external field in the H–H$^+$ collision with the impact parameter $b = 0.625$ a.u., for the frequency $\omega_0 = 0.01$a.u., peak intensity 1×10^{12} W/cm^2 and various phases. The left-hand side and right-hand side of the internuclear distance axis correspond to the incident particle moving toward the target and away from the target, respectively.

force from the external field, in the region of internuclear distances $R_{AB} \lesssim 5$ a.u.

As the incident particle approaches the target, the force from the laser field experienced by the electron has the same direction as the Coulomb force from the incident particle nucleus (the positive direction of the z_0 axis), if the field phase is 90° or 180° (see figure 3.5). In this case, the total force from the incident particle and external field, tending to detach the electron from the target, is greater than the force in the absence of the external field. This leads to enhancement of ionization. For the phases 0° and 270°, on the contrary, the external field weakens the influence of the incident particle on the electron, leading to suppression of ionization in this section of the nuclear motion.

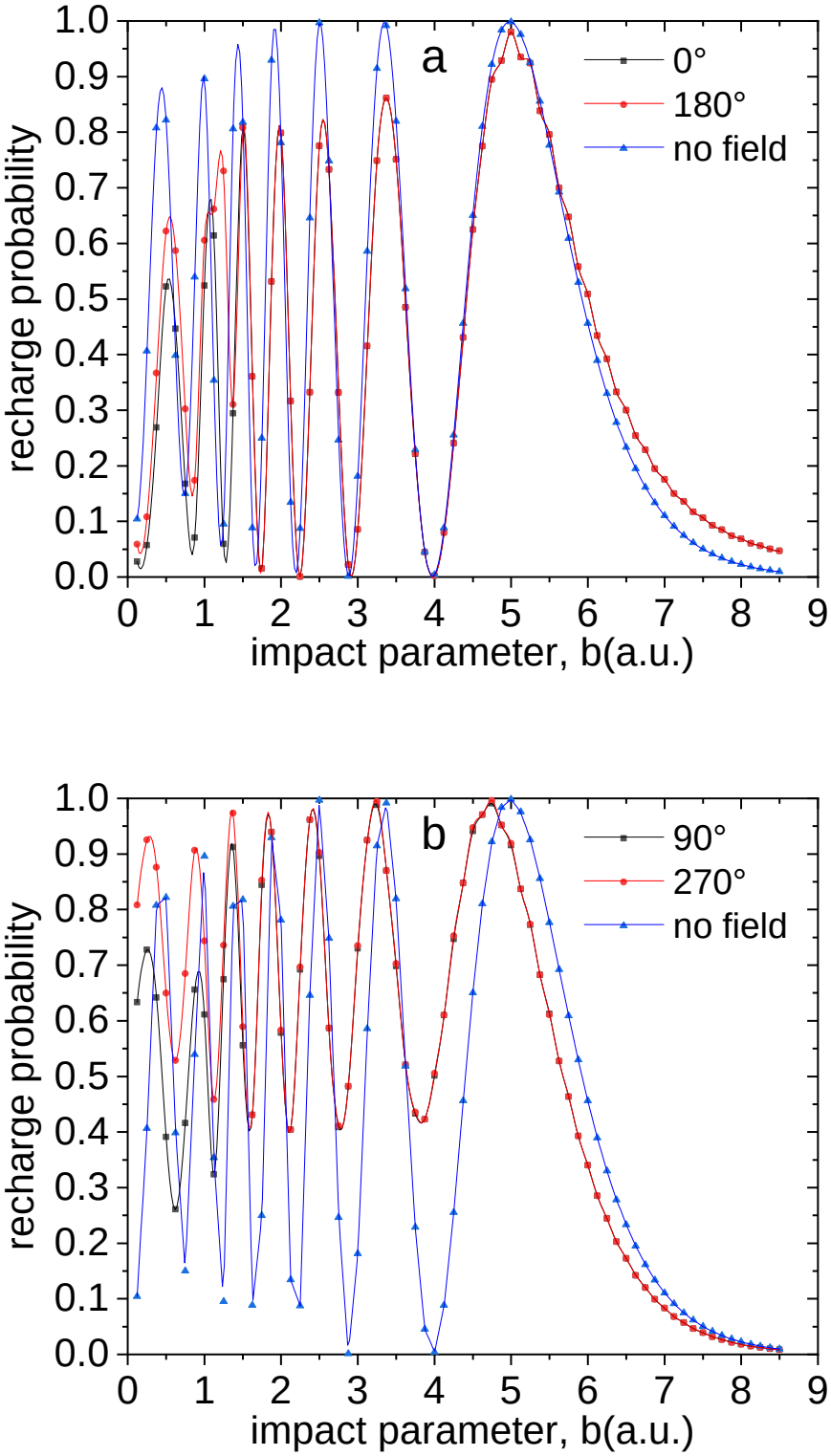

Figure 3.6: Charge transfer probability $P_{\rm ct}$ as a function of impact parameter in the collision of a proton with a hydrogen atom in a linearly polarized external field with the frequency $\omega_0 = 0.01$ a.u. and intensity 1×10^{13} W/cm^2, for different field phases: (a), $\phi = 0°$ (black line) and $\phi = 180°$ (red line); (b), $\phi = 90°$ (black line) and $\phi = 270°$ (red line). Blue lines in both panels show $P_{\rm ct}$ without the external field.

In the section of the nuclear motion when the incident particle flies away from the target, the picture is different. Here the external field is directed towards the incident particle, thus favoring the transfer of the electron from the target to the incident particle, if the field phase is equal to 180° or 270°. Actually, this portion of the nuclear motion has a dominant effect on the charge transfer and ionization during the collision. The argument is as follows. In close collisions, the excited electronic states of the quasimolecule are populated with a high probability. When the incident particle is still approaching the target, the charge transfer is well described by the interference of the $1\sigma_g$ and $1\sigma_u$ molecular orbitals only. However, when the incident particle is moving away, the population of the higher excited bound states is already significant. Our calculations for the field phase $\phi = 270°$ show that at the moment when the instantaneous charge transfer probability reaches its last local minimum ($R_{AB} \approx 4.1$ a.u.), the probability of finding the electron in the ground state is 44%, in the first excited state - 12%, and 43.5% falls on the higher excited bound states. Loosely bound electrons are more susceptible to the influence of the external field, which contributes to the charge transfer between the target and the incident particle, as well as ionization. These considerations explain why the population of the incident particle half-space for the field phases 180° and 270° turns out to be greater than in the case of no external field (see figure 3.4). If the field phase is equal to 0° or 90°, then the force from the external field is directed towards the target as the incident particle moves away, suppressing the charge transfer. In this case, the population of the half-space of the incident particle turns out to be less than in the case without the external field, which also explains the result shown in figure 3.4.

Figure 3.6 shows the results for the probability of charge transfer in the case of an external field with the same frequency $\omega = 0.01$ a.u. but higher intensity 1×10^{13} W/cm^2. These results demonstrate that in a stronger field, the phase significantly affects the charge transfer probability P_{ct}. In the region of impact parameters $b > 2$ a.u., the probabilities P_{ct} for the phases 0° and 180° differ from each other by a value much less than 1%. The same conclusion can be drawn when comparing the results for the phases 90° and 270°. The charge transfer probabilities for the pair of phases 0° and 180°, on the one hand, and the pair of phases 90° and 270°, on the other hand, differ significantly from each other, in accordance with the case of intensity 1×10^{12} W/cm^2. In the field with the intensity 1×10^{13} W/cm^2 this

difference becomes even more noticeable. For smaller impact parameters, $b < 2$ a.u, the value of P_{ct} for the phase 180° turns out to be larger than for the phase 0° , and for the phase 270° it is larger than for the phase 90°. These results also fully agree with what was observed in the calculations with the external field intensity of 1×10^{12} W/cm^2.

The ionization probability P_{i} in the field with the intensity 1×10^{13} W/cm^2 is much larger than in the weaker field with the intensity 1×10^{12} W/cm^2. figure 3.2b shows its dependence on the impact parameter b. It turns out that for the field phase 180° the ionization probability is the largest, and for the phase 270° it is the smallest for all impact parameters b, this observation agrees with that already seen at the intensity 1×10^{12} W/cm^2. In the case of the intensity 1×10^{13} W/cm^2, however, ionization caused by the field with the phase $\phi = 90°$ is larger compared to the field with the phase $\phi = 0°$. This is in contrast with the case of intensity 1×10^{12} W /cm^2 where ionization caused by the field with the phase $\phi = 90°$ was smaller.

The third series of calculations uses an external field with a frequency $\omega = 2$ a.u. and peak field intensity $I_0 = 5 \times 10^{14}$ W/cm^2. The charge transfer probability versus the impact parameter is shown in figure 3.7. Our results confirm the initial assumption: the phase of a rapidly oscillating electromagnetic field does not affect the charge transfer dynamics during slow collisions. At the frequency of the electromagnetic field $\omega = 2$ a.u., the time of flight of the incident particle is on the order of several hundred optical cycles. For example, with the impact parameter $b = 0.625$ a.u., the time of flight of the incident particle is approximately equal to 600 optical cycles of the external field. During one oscillation of the electron density between the target and the incident particle, approximately 90 oscillations of the electromagnetic field occur. Then the particular phase value at $t = 0$ does not play any significant role in the charge transfer process. The ionization probability in the third series of the calculations is about 11-12% for all the impact parameters and phases of the electromagnetic field. Very weak dependence on the impact parameter indicates that the collision of the incident particle with the target does not significantly affect ionization dynamics in this case, which is mainly due to the external field. This conclusion is confirmed by calculations of a single hydrogen atom in the external field with the same parameters. The resulting ionization probability is close

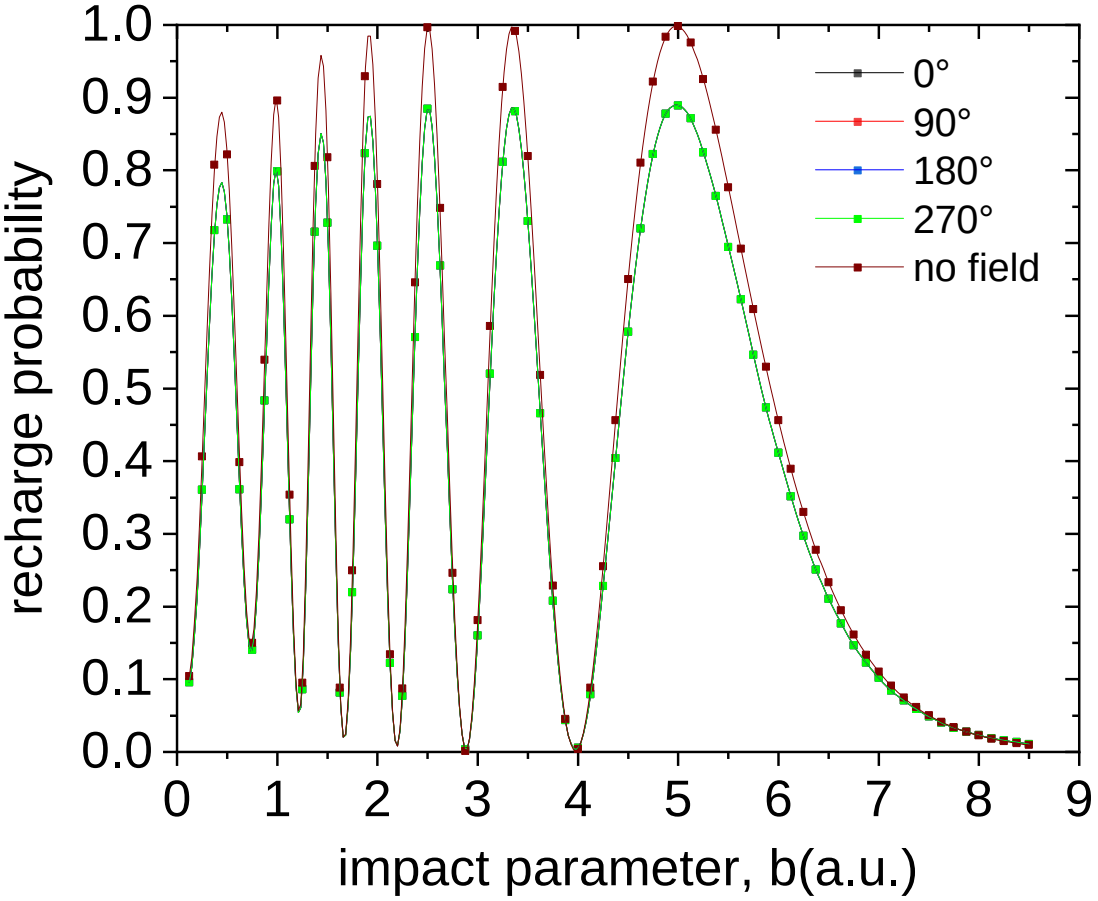

Figure 3.7: Charge transfer probability $P_{\rm ct}$ as a function of impact parameter in the collision of a proton with a hydrogen atom in a linearly polarized external field with the frequency $\omega_0 = 2$ a.u. and intensity 5×10^{14} W/cm^2, for the field phases $\phi = 0°$, $\phi = 90°$, 180°, and 270°. Also shown is the charge transfer probability without the external field. The collision velocity is $v_0 = 0.1$ a.u.

Table 3.1: Charge transfer cross sections depending on phase (10^{-16} cm^2) for laser field frequency $\omega = 0.01$ a.u.

Phase	I_0=1×10^{12} W/cm^2	I_0=1×10^{13} W/cm^2
0°	20.62	22.94
90°	23.37	24.48
180°	20.91	23.24
270°	23.69	24.83

to that obtained for laser-assisted collisions. This is in contrast with the case of a low-frequency laser field, where ionization can be substantially enhanced at small impact parameters (see figure 3.2). While excited bound states are still populated in close collisions, the tunneling and above-the-barrier ionization mechanisms do not work in the high-frequency field.

The phase-dependent capture cross section $\sigma_{\rm ct}(\phi)$ is calculated according to the following equation:

$$\sigma_{\rm ct}(\phi) = 2\pi \int_0^\infty dbbP_{\rm ct}(b,\phi), \tag{3.22}$$

where the charge transfer probability $P_{\rm ct}(b,\phi)$ depends on the impact parameter b and phase ϕ. The results are presented in Table 3.1 for the frequency $\omega = 0.01$ a.u. where the phase dependence is well pronounced. As one can see, upon integration of the charge transfer probability over the impact parameter, the result still exhibits a distinct phase dependence. Similarly, the phase-averaged capture cross section $\bar{\sigma}_{\rm ct}$ is obtained from the equation:

$$\bar{\sigma}_{\rm ct} = 2\pi \int_0^\infty db\, b\, \bar{P}_{\rm ct}(b), \tag{3.23}$$

where $\bar{P}_{\rm ct}(b)$ is the charge transfer probability averaged over the entire phase range:

$$\bar{P}_{\rm ct}(b) = \frac{1}{2\pi} \int_0^{2\pi} d\phi P_{\rm ct}(b,\phi). \tag{3.24}$$

The results for the phase-averaged charge transfer cross section are presented in Table 3.2. In the absence of the laser field our result agrees well with the experimental data [99].

Table 3.2: Charge transfer cross sections depending on phase (10^{-16} cm^2) for laser field frequency $\omega = 0.01$ a.u.

Frequency	Intensity	Result of this work	Result of work [99]
No field		22.33	21.9
0.01 a.u.	1×10^{12} W/cm^2	22.15	
0.01 a.u.	1×10^{13} W/cm^2	23.87	
2 a.u.	5×10^{14} W/cm^2	20.19	

3.4 Chapter 3 Summary

This chapter of the dissertation examines the processes of charge transfer and ionization during collisions of a proton with a hydrogen atom in the presence of a linearly polarized electromagnetic field. Numerical simulations were performed for two frequencies (in the infrared and extreme ultraviolet ranges), three peak intensities and four phase values of the electromagnetic field at the moment of the shortest distance between the incident particle and the target. Results for frequency $\omega = 0.01$ a.u. demonstrate a significant influence on charge transfer and ionization from the phase of the electromagnetic field. The dynamics of charge transfer and ionization are determined by the superposition of Coulomb forces from nuclei and the force from the electromagnetic field in the region of the incident particle approaching the target. The force exerted by the electromagnetic field in this region, in turn, is determined by the phase of the field at the moment of the shortest distance between the incident particle and the target. If the impact parameter is small enough ($b < 2$ a.u.), the excited states of the quasimolecule H_2^+ turn out to be significantly populated while the incident particle is in close proximity to the target. In this case, the areas of motion of the nucleus when the incident particle approaches the target and when it departs differ significantly in their role in the processes of charge transfer and ionization. When the incident particle is still approaching the target, the electron dynamics are caused mainly by the interference of the initially occupied $1\sigma_g$ and $1\sigma_u$ molecular orbitals. However, by the time the incident particle leaves, the overlying electronic states are already populated, which affects the dynamics of charge transfer and ionization in an external field. The probabilities of charge transfer and ionization are different for different field phases at the same strength.

The lowest ionization both at an intensity of 1×10^{12} W/cm^2 and at an intensity of 1×10^{13} W/cm^2 is observed, if the field phase is 270°.

At large impact parameters ($b > 2$ a.u.), the probability of excitation of a quasi-molecule into higher-lying electronic states is small, and the dynamics of charge transfer are mainly determined by the interference of the initially occupied $1\sigma_g$ and $1\sigma_u$. Near the point of closest approach between the incident particle and the target, the axis of the molecule is almost perpendicular to the direction of action of the external field force. In this situation, the dependence on the sign of the field disappears. Then the probability of charge transfer is the same for both phases of the field in pairs 0°, 180° and 90°, 270°, but differs from the probability for the other couples. For the electromagnetic field frequency $\omega = 2$ a.u. and intensity $I_0 = 5 \times 10^{14}$ W/cm^2, no influence of the electromagnetic field phase on the probabilities of charge transfer and ionization is observed. This is well explained by the much faster oscillations of the electromagnetic field compared to the oscillations of the electron density between the target and the incident particle.

Conclusion

In this dissertation, various effects in quasimolecules that arise when irradiated with a linearly polarized laser field were studied, which was considered both in the dipole approximation and beyond.

The process of single-photon ionization for the H_2^+ molecule in the antisymmetric initial state $1\sigma_u$ in the classical case was studied. For this purpose, the energy and angular distributions of emitted photoelectrons were constructed, as well as the dependence of the total probability of ionization on the angle β between the polarization vector and the molecular axis. The results obtained demonstrate that for certain parameters of the laser field: 1) the probability of ionization increases monotonically with increasing angle β, which contradicts intuitive expectations; 2) The maxima in the angular distributions practically do not change their position as the angle β increases. This behavior of the ionization probability and angular distributions is explained by two-center interference, due to which the most probable direction of photoelectron emission is determined by two factors: the external field tends to knock out the electron in the direction of the polarization vector and the amplification of the signal at a certain angle of photoelectron emission from the vicinity of two nuclei due to the interference of the wave function.

A relativistic method for calculating one-electron quasimolecules in an external field was developed. The assessment of relativistic effects was carried out by scaling the parameters of the system according to the nuclear charge Z. The results obtained demonstrate the increasing role, with increasing nuclear charge Z, of relativistic effects such as a shift in the resonant frequency and an increase in the ionization potential of the quasimolecule. Having studied the multiphoton ionization of quasimolecules at several internuclear distances, it was discovered that relativistic effects can change their electronic structure, shifting the resonance to internuclear distances of different scales for different quasimolecules. The scope of the dipole

approximation for the three-dimensional Dirac equation has been achieved. The results obtained demonstrate that the dipole approximation for molecules with a high nuclear charge is violated, leading to incorrect calculations of ionization dynamics.

An analysis of the influence of the phase of a linearly polarized electromagnetic field in collisions of a proton atom with a hydrogen atom in low-energy collisions has been carried out. The calculation results for H_2^+ demonstrate a significant influence on the probability of electron capture by a incident particle for a slowly oscillating field, and the stage of approach of the incident particle and its removal have different effects on the ionization dynamics. At the same time, the rapidly oscillating field does not affect the process of electron capture by the incident particle.

Bibliography

[1] *Krausz F., Ivanov M.* Attosecond physics // Reviews of Modern Physics. — 2011. — Vol. 81, no. 1. — P. 163.

[2] Extremely high-intensity laser interactions with fundamental quantum systems / A. Di Piazzaand C. Müller Z. Hatsagortsyan [et al.] // Reviews of Modern Physics. — 2012. — Vol. 84, no. 3. — P. 1177.

[3] *Vrakking M. J. J.* Attosecond imaging // The Journal of Physical Chemistry B. — 2014. — Vol. 16, no. 7. — P. 2775.

[4] *Villeneuve D. M.* Attosecond science // Contemporary Physics. — 2018. — Vol. 59, no. 1. — P. 47.

[5] Dynamics of resonant x-ray and Auger scattering / F. Gel'mukhanov, M. Odelius S. Polyutov [et al.] // Reviews of Modern Physics. — 2021. — Vol. 93, no. 3. — P. 035001.

[6] *Patanen M., Svensson S., Martensson N.* Electron spectroscopy using ultra brilliant synchrotron X-ray sources // Journal of Electron Spectroscopy and Related Phenomena. — 2015. — Vol. 200. — Pp. 78–93.

[7] Roadmap of ultrafast x-ray atomic and molecular physics / L. Young, K. Ueda, M. Gühr [et al.] // Journal of Physics B: Atomic, Molecular and Optical Physics. — 2018. — Vol. 51. — P. 032003.

[8] *Posthumu J. H.* The dynamics of small molecules in intense laser fields // Reports on Progress in Physics. — 2004. — Vol. 67, no. 5. — P. 623.

[9] High Harmonic Generation from Multiple Orbitals in N_2 / B. K. McFarland, J. P. Farrell, P. H. Bucksbaum [et al.] // Science. — 2008. — Vol. 322, no. 5905. — Pp. 1232–1235.

[10] Direct Measurement of the Angular Dependence of Ionization for N_2, O_2 and CO_2 in Intense Laser Fields / D. Pavičić, K. F. Lee, D. M. Rayner, P. B.

Corkum [et al.] // Physical Review Letters. — 2007. — Vol. 98, no. 24. — P. 243001.

[11] Direct Measurement of the Angular Dependence of the Single-Photon Ionization of Aligned N_2 and CO_2 / I. Thomann, R. Lock, V. Sharma, E. Gagnon [et al.] // The Journal of Physical Chemistry A. — 2008. — Vol. 112. — P. 9382.

[12] Laser-induced electron tunneling and diffraction / M. Meckel, D. Comtois, D. Zeidle [et al.] // Science. — 2008. — Vol. 320, no. 5882. — P. 1478.

[13] Imaging ultrafast molecular dynamics with laser-induced electron diffraction / C. I. Blaga, J. Xu, A. D. DiChiara, E. Sistrunk [et al.] // Nature. — 2012. — Vol. 483. — Pp. 194—197.

[14] Tomographic imaging of molecular orbitals / J. Itatani, J. Levesque, D. Zeidler [et al.] // Nature. — 2004. — Vol. 432. — Pp. 867–871.

[15] Laser-induced electron diffraction: A tool for molecular orbital imaging / M. Peters, T. T. Nguyen-Dang, E. Charron, A. Keller [et al.] // Physical Review A. — 2012. — Vol. 85, no 5. — P. 053417.

[16] *Henkel J., Lein M., Engel V.* Interference in above-threshold-ionization electron distributions from molecules // Physical Review A. — 2011. — Vol. 83, no. 5. — P. 051401(R).

[17] Two-Source Double-Slit Interference in Angle-Resolved High-Energy Above-Threshold Ionization Spectra of Diatoms / M. Okunishi, R. Itaya, K. Shimada [et al.] // Physical Review Letters. — 2009. — Vol. 103, no. 4. — P. 043001.

[18] Two-center interferences in photoionization of a dissociating H_2^+ molecule / A. Picón, A. Bahabad, H.C., Kapteyn [et al.] // Physical Review A. — 2011. — Vol. — 83, no. 1. — P. 013414.

[19] *Yuan K.-J., Bandrauk A. D.* Angle-dependent molecular above-threshold ionization with ultrashort intense linearly and circularly polarized laser pulses// Physical Review A. — 2011. — Vol. 84, no. 1. — P. 013426.

[20] Role of the Intramolecular Phase in High-Harmonic Generation / M. Lein, N. Hay, R. Velotta [et al.] // Physical Review Letters. — 2002. — Vol. 88, no. 18.— P. 183903.

[21] Interference effects in high-order harmonic generation with molecules / M. Lein,

N. Hay, R. Velotta, J [et al.] // Physical Review A. — 2002. — Vol. 66, no. 2. — P. 023805.

[22] Orientation dependence of high-order harmonic generation in molecules / M. Lein, P. P. Corso, J. P. Marangos [et al.] // Physical Review A. — 2003. — Vol. 67, no. 2. — P. 023819.

[23] *Etches A., Gaarde M. B., Madsen L. B.* Theory of tunneling ionization of molecules: Weak-field asymptotics including dipole effects // Physical Review A. — 2011. — Vol. 84, no. 5. — P. 023418.

[24] Following a chemical reaction using high-harmonic interferometry / H. J. Wörner, J. B. Bertrand, D. V. Kartashov [et al.] // Nature. — 2010. — Vol. 466. — P. 604.

[25] Signatures of the continuum electron phase in molecular strong-field photoelectron holography / M. Meckel, A. Staudte, S. Patchkovskii [et al.] // Nature Physics. — 2014. — Vol. 10. — Pp. 594–600.

[26] Probing Molecular Dynamics by Laser-Induced Backscattering Holography / M. Haertelt, X.-B. Bian, M. Spanner [et al.] // Physical Review Letters. — 2016. — Vol. 116, no. 13. — P. 133001.

[27] *Bian X. B., Bandrauk A. D.* Probing Molecular Dynamics by Laser-Induced Backscattering Holography // Physical Review Letters. — 2012. — Vol. 108, no. 26. — P. 263003.

[28] *Lefebvre R. Atabek O.* Progress toward full optical control of ultracold-molecule formation: Role of scattering Feshbach resonances // Physical Review A. — 2019. — Vol. 101, no. 6. — P. 063406.

[29] Laser-assisted binary-encounter emission in relativistic ion-atom collision / Z. Wang, B. Najjari, S. F. Zhang [et al.] // Physical Review A. — 2019. — Vol. 100, no. 5. — P. 052710.

[30] *Fabrikant I. I., Ambalampitiya H. B., Schneider I. F.* Semiclassical theory of laser-assisted dissociative recombination // Physical Review A. — 2021. — Vol. 103, no. 5. — P. 053115.

[31] Dynamics of two atoms undergoing light-assisted collisions in an optical microtrap / P. Sompet, A. V. Carpentier, Y. H. Fung [et al.] // Physical Review A. — 2013. — Vol. 88, no. 5. — P. 051401(R).

[32] Ab initio study of charge exchange in collisions of B^{2+} ions with Ne and Ar targets / A. Moussa, A. Zaidi, S. Lahmar [et al.] // Physical Review A. — 2012. — Vol. 85, no. 2. — P. 022715.

[33] *Zuo T., Bandrauk A. D.* Charge-resonance-enhanced ionization of diatomic molecular ions by intense lasers // Physical Review A. — 1995. — Vol. 52, no. 4. — P. R2511(R).

[34] Strong Orientation Effects in Ionization of H_2^+ by Short, Intense, High-Frequency Light Pulses / S. Selstø, M. Førre, J. P. Hansen [et al.] // Physical Review Letters. — 2005. — Vol. 95, no. 9. — P. 093002.

[35] *Telnov D. A., Chu S. I.* Ab initio study of the orientation effects in multiphoton ionization and high-order harmonic generation from the ground and excited electronic states of H_2^+ // Physical Review A. — 2007. — Vol. 76, no. 4. — P. 043412.

[36] *Kamta G. L., Bandrauk A. D.* Orbital symmetry and interference effects in molecular high-order harmonic generation // Physical Review A. — 2009. — Vol. 80, no. 4. — P. 041403(R).

[37] *Yuan K.-J., Bian X.-B., Bandrauk A. D.* Two-center interference in molecular photoelectron energy spectra with intense attosecond circularly polarized XUV laser pulses // Physical Review A. — 2014. — Vol. 90, no. 2. — P. 023407.

[38] *Yuan K.-J., Lu H. Z., Bandrauk A. D.* Linear- and circular-polarization photoionization angular distributions in H_2 and H_2^+ by attosecond xuv laser pulses // Physical Review A. — 2011. — Vol. 83, no. 4. — P. 043418.

[39] *Guan X., DuToit R. C., Bartschat K.* Photoionization of the H_2^+ ion by ultrashort elliptically polarized laser pulses // Physical Review A. — 2013. — Vol. 87, no. 5. — P. 053410.

[40] *Fetić B., Miloševi D. B.* Numerical solution of the time-dependent Schrödinger equation for H_2^+ ion with application to high-harmonic generation and above-threshold ionization // Physical Review E. — 2017. — Vol. 95, no. 5. — P. 053309.

[41] *Gudzenko L. I., Yakovlenko S. I.* Radiative Collisions // Soviet Journal of Experimental and Theoretical Physics. — 1972. — Vol. 35, no. 5. — Pp. 887–881.

[42] Carrier-Envelope-Phase Stabilized Terawatt Class Laser at 1 KHz with a Wavelength Tunable Option / B. Langdon, J. Garlick, X. Ren [et al.] // Optics Express. — 2015. — Vol. 23, no. 4. — P. 4563.

[43] CEP-Stabilized, Sub-18 Fs, 10 KHz and TW-Class 1 KHz Dual Output Ti:Sa Laser with Wavelength Tunability Option / A. Golinelli, X. Chen, B. Bussière [et al.] // Optics Express. — 2019. — Vol. 27, no. 10. — Pp. 13624–13636.

[44] Goulielmakis E. Direct Measurement of Light Waves / E. Goulielmakis, M. Uiberacker, R. Kienberger [et al.] // Science. — 2004. — Vol. 305, no. 4. — P. 1267.

[45] Paasch-Colberg T. Solid-State Light-Phase Detector / T. Paasch-Colberg, A. Schiffrin, N. Karpowicz [et al.] // Nature Photonics. — 2014. — Vol. 8, no. 3. — P. 214.

[46] *Domínguez-Gutiérrez F. J., Cabrera-Trujillo R.* Pulse duration effects on laser-assisted electron transfer cross section for He^{2+} ions colliding with atomic hydrogen // The European Physical Journal D. — 2014. — Vol. 68. — P. 226.

[47] *Kirchner T.* Manipulating ion-atom collisions with coherent electromagnetic radiation // Physical Review Letters. — 2002. — Vol. 89, no. 9. — P. 093203.

[48] *Domínguez-Gutiérrez F. J., Cabrera-Trujillo R.* Comparison of laser-assisted charge transfer of symmetric and asymmetric colliding systems // Journal of Physics: Conference Series. — 2014. — Vol. 512. — P. 012033.

[49] *Niederhausen T., Thumm U.* Capture and ionization in laser-assisted proton–hydrogen collisions // Physical Review A. — 2006. — Vol. 73, no. 4. — P. 041404(R).

[50] Laser-assisted charge transfer in He^{2+}+ collisions / Fatima Anis, V. Roudnev, R. Cabrera-Trujillo [et al.] // Physical Review A. — 2006. — Vol. 73, no. 4. — P. 043414.

[51] Optimal control of charge transfer for slow H^++D collisions with shaped laser pulses / W. Zhang, C.-C. Shu, T.-S. Ho [et al.] // The Journal of Chemical Physics. — 2014. — Vol. 140, no. 9. — P. 094304.

[52] *Vanne Y. V., Saenz A.* Solution of the time-dependent Dirac equation for multiphoton ionization of highly charged hydrogenlike ions // Physical Review A. — 2012. — Vol. 85, no. 3. — P. 033411.

[53] I. Relativistic ionization probabilities of hydrogenlike ions exposed to intense laser pulses / V. Ivanova, A. Saenz, A. I. Bondarev [et al.] // Journal of Physics: Conference Series. — 2017. — Vol. 875, no. 2. — P. 022031.

[54] Alternative gauge for the description of the light-matter interaction in a relativistic framework / Kjellsson T., Førre M., Simonsen A. S. [et al.] // Physical Review A. — 2017. — Vol. 96, no. 2. — P. 023426.

[55] Dual-kinetic-balance approach to the Dirac equation for axially symmetric systems: Application to static and time-dependent fields / E. B. Rozenbaum, D. A. Glazov, V. M. Shabaev [et al.] // Physical Review A. — 2014. — Vol. 89, no. 1. — P. 012514.

[56] *Chu S.-I., Telnov D. A.* Beyond the Floquet theorem: generalized Floquet formalisms and quasienergy methods for atomic and molecular multiphoton processes in intense laser fields // Physics Reports. — 2004. — Vol. 390, no. 1-2. — Pp. 1–131.

[57] Ionization dynamics beyond the dipole approximation induced by the pulse envelope / A. S. Simonsen, T. Kjellsson, M. Førre [et al.] // Physical Review A. — 2016. — Vol. 93, no. 5. — P. 053411.

[58] *Pindzola, M. S., Ludlow, J. A., Colgan, J.* Photoionization of highly charged atomic ions // Physical Review A. — 2010. — Vol. 81, no. 6. — P. 063431.

[59] Photoionization of highly charged atomic ions / M. S. Pindzola, S. A. Abdel-Naby, F. Robicheaux [et al.] // Physical Review A. — 2012. — Vol. 85, no. 3. — P. 032701.

[60] *Ivanov I. A.* Relativistic calculation of the electron-momentum shift in tunneling ionization // Physical Review A. — 2015. — Vol. 91, no. 4. — P. 043410.

[61] Relativistic ionization characteristics of laser-driven hydrogenlike ions / H. Bauke, H. G. Hetzheim, G. R. Mocken [et al.] // Physical Review A. — 2011. — Vol. 83, no. 6. — P. 063414.

[62] Spin dynamics in relativistic ionization with highly charged ions in super-strong laser fields / M. Klaiber, E. Yakaboylu, C. Müller [et al.] // Journal of Physics B: Atomic, Molecular and Optical Physics. — 2014. — Vol. 47, no. 6. — P. 065603.

[63] *Klaiber M., Hatsagortsyan K. Z.* Spin-asymmetric laser-driven relativistic tunneling from **p** states // Physical Review A. — 2014. — Vol. 90, no. 6. — P. 063416.

[64] Nondipole Ionization Dynamics of Atoms in Superintense High-Frequency Attosecond Pulses / M. Førre, J. P. Hansen, L. Kocbach [et al.] // Physical Review Letters. — 2006. — Vol. 97, no. 4. — P. 043601.

[65] Molecules in intense xuv pulses: Beyond the dipole approximation in linearly and circularly polarized fields / M. Førre, S. Selstø, J. P. Hansen [et al.] // Physical Review A. — 2007. — Vol. 76, no. 3. — P. 033415.

[66] *Zhou Z., Chu S.-I.* Multiphoton above-threshold ionization in superintense free-electron x-ray laser fields: Beyond the dipole approximation // Physical Review A. — 2013. — Vol. 87, no. 2. — P. 023407.

[67] *Moe T. E., Førre M.* Ionization of atomic hydrogen by an intense x-ray laser pulse: An ab initio study of the breakdown of the dipole approximation // Physical Review A. — 2018. — Vol. 97, no. 1. — P. 013415.

[68] *Kjellsson T., Selstø S., Lindroth E.* Relativistic ionization dynamics for a hydrogen atom exposed to superintense XUV laser pulses // Physical Review A. — 2017. — Vol. 95, no. 4. — P. 043403.

[69] Multiphoton Ionization of One-Electron Relativistic Diatomic Quasimolecules in Strong Laser Fields / D. A. Telnov, D. A. Krapivin, J. Heslar [et al.] // The Journal of Physical Chemistry A. — 2018. — Vol. 122, no. 11. — Pp. 8026–8036.

[70] *Krapivin D. A., Telnov D. A.* Anomalous dependence of ionization probability and electron angular distributions on orientation of molecular axis in photoionization of H_2^+ : effect of two-center interference // Journal of Physics B: Atomic, Molecular and Optical Physics. — 2021. — Vol. 54, no. 20. — P. 205601.

[71] *Krapivin D. A., Telnov D. A.* Influence of the phase of the electromagnetic field on the processes of charge transfer and ionization in laser-assisted collisions of protons with hydrogen atoms // The European Physical Journal D. — 2023. — Vol. 77, no. 99.

[72] *Handbook of Mathematical Functions*, edited by M. Abramowitz and I. Stegun (Dover, New York, 1965).

[73] Attosecond Strobing of Two-Surface Population Dynamics in Dissociating H_2^+ / A. Staudte, D. Pavičić, S. Chelkowski [et al.] // Physical Review Letters. — 2007. — Vol. 98, no. 7. — P. 073003.

[74] *Telnov D. A., Chu S. I.* Ab initio study of high-order harmonic generation H_2^+ of in intense laser fields: Time-dependent non-Hermitian Floquet approach // Physical Review A. — 2005. — Vol. 71, no. 1. — P. 013408.

[75] *Chu X., Shih-I Chu* Self-interaction-free time-dependent density-functional theory for molecular processes in strong fields: High-order harmonic generation of H_2^+ in intense laser fields // Physical Review A. — 2001. — Vol. 63, no. 2. — P. 023411.

[76] *Marston C.C., and Gabriel G. Balint-Kurti* The Fourier grid Hamiltonian method for bound state eigenvalues and eigenfunctions // Physical Review A. — 2001. — Vol. 63, no. 2. — P. 023411.

[77] *Tong X.-M., Chu S.-I.* Dynamics of Driven Quantum Systems // Chemical Physics. — 1997. — Vol. 217, no. 2-3. — Pp. 119–130.

[78] *Crank J., Nicolson P.* A Practical Method for Numerical Evaluation of Solutions of Partial Differential Equations of the Heat-Conduction Type // Mathematical Proceedings of the Cambridge Philosophical Society. — 1947. — Vol. 43, no. 6. — Pp. 50–67.

[79] *Ponomarev L.I., Somov L.N.* The wave functions of continuum for the two-center problem in quantum mechanics // Journal of Computational Physics. — 1976. — Vol. 20, no. 2. — P. 183.

[80] *Howard D. C., Fano U.* Interference in the Photo-Ionization of Molecules // Physics review journals archive. — 1966. — Vol. 150, no. 1. — P. 30.

[81] Interferences in the photoelectron spectrum of H_2^+ molecules at high energy / O.A. Fojón, A. Palacios, J. Fernández [et al.] // Physics Letters A. — 2006. — Vol. 350, no. 5-6. — Pp. 371–374.

[82] Photon-momentum transfer in diatomic molecules: An ab initio study / H. Liang, M.-X. Wang, X.-R. Xiao [et al.] // Physics Letters A. — 2018. — Vol. 98, no. 6. — P. 063413.

[83] *Parpia F. A., Mohanty A. K.* Relativistic basis-set calculations for atoms with Fermi nuclei // Physical Review A. — 1992. — Vol. 46, no. 7. — Pp. 3735–3745.

[84] *Angeli I., Marinova K. P.* Table of experimental nuclear ground state charge radii: An update // Atomic Data and Nuclear Data Tables. — 2013. — Vol. 99, no. 1. — Pp. 69–95.

[85] *Telnov D. A., Chu S.-I.* Ab initio study of the orientation effects in multiphoton ionization and high-order harmonic generation from the ground and excited electronic states H_2^+ // Physical Review A. — 2007. — Vol. 76, no. 4. — P. 043412.

[86] *Telnov D. A., Chu S.-I.* Time-dependent generalized pseudospectral method for accurate treatment of multiphoton processes of diatomic molecules in intense laser fields // Computer Physics Communications. — 2011. — Vol. 182, no. 1. — Pp. 18–20.

[87] *Grant I. P* B-spline methods for radial Dirac equations // J. Journal of Physics B: Atomic, Molecular and Optical Physics. — 2009. — Vol. 42, no. 5. — P. 055002.

[88] *Johnson W. R., Blundell S. A., Sapirstein J.* Finite basis sets for the Dirac equation constructed from B splines // Physical Review A. — 1988. — Vol. 37, no. 2. — Pp. 307–315.

[89] *Layton E., Chu S.-I* Generalized Fourier-grid Hamiltonian approach to the Dirac equation: variational solution without basis set // Physics Letters. — 1988. — Vol. 186, no. 1. — Pp. 100–106.

[90] Relativistic calculations of the ground state energies and the critical distances for one-electron homonuclear quasi-molecules / D. V. Mironova, I. I. Tupitsyn, V. M. Shabaev [et al.] // Physics Letters. — 2015. — Vol. 449. — Pp. 10–13.

[91] *Ishikawa A., Nakashima H., Nakatsuji H.* Solving the Schrödinger and Dirac equations of hydrogen molecular ion accurately by the free iterative complement interaction method // The Journal of Chemical Physics. — 2008. — Vol. 128, no. 12. — P 124103.

[92] *Yang L., Heinemann D., Kolb D.* An accurate solution of the two-centre Dirac equation for H_2^+ by the finite-element method // Chemical Physics Letters. — 1991. — Vol. 178, no. 2-3. — Pp. 213–215.

[93] *Franke R., Kutzelnigg W.* Perturbative relativistic calculations for one-electron

systems in a Gaussian basis // Chemical Physics Letters. — 1992. — Vol. 199, no. 6. — Pp. 561–566.

[94] *Fillion-Gourdeau F., Lorin E., Bandrauk A.* Numerical solution of the time-independent Dirac equation for diatomic molecules: **B** splines without spurious states // Physical Review A. — 2012. — Vol. 85, no. 2. — P. 022506.

[95] *Madsen L. B., Lambropoulos P.* Scaling of hydrogenic atoms and ions interacting with laser fields: Positronium in a laser field // Physical Review A. — 1999. — Vol. 59, no. 6. — Pp. 4574–4579.

[96] *Zeldovich Y. B., Popov V. S.* Electronic structure of superheavy atoms // Soviet Physics Uspekhi. — 1972. — Vol. 1, no. 6. — Pp. 673–694.

[97] *Mulliken R. S.* Intensities of Electronic Transitions in Molecular Spectra II. Charge–Transfer Spectra // The Journal of Chemical Physics. — 1939. — Vol. 7, no. 1. — Pp. 20–34.

[98] *Müller B., Greiner W.* The two center Dirac equation // Zeitschrift für Naturforschung A. — 1976. — Vol. 31, no. 1. — Pp. 1–30.

[99] *Jealy M. W., Zyl B. V.* Cross sections for electron capture and loss. II. H impact on H and H_2^+ // Physical Review A. — 1987. — Vol. 36, no. 7. — P. 3100.